Simulation and understanding of atomic and molecular quantum crystals

Claudio Cazorla*

School of Materials Science and Engineering, and Integrated Materials Design Centre, UNSW Australia, Sydney NSW 2052, Australia

Jordi Boronat†

Departament de Física, Universitat Politècnica de Catalunya, Campus Nord B4-B5, E-08034 Barcelona, Spain

(published 3 August 2017)

Quantum crystals abound in the whole range of solid-state species. Below a certain threshold temperature the physical behavior of rare gases (^{4}He and Ne), molecular solids (H_2 and CH_4), and some ionic (LiH), covalent (graphite), and metallic (Li) crystals can be explained only in terms of quantum nuclear effects (QNE). A detailed comprehension of the nature of quantum solids is critical for achieving progress in a number of fundamental and applied scientific fields such as planetary sciences, hydrogen storage, nuclear energy, quantum computing, and nanoelectronics. This review describes the current physical understanding of quantum crystals formed by atoms and small molecules, as well as the wide palette of simulation techniques that are used to investigate them. Relevant aspects in these materials such as phase transformations, structural properties, elasticity, crystalline defects, and the effects of reduced dimensionality are discussed thoroughly. An introduction to quantum Monte Carlo techniques, which in the present context are the simulation methods of choice, and other quantum simulation approaches (e.g., path-integral molecular dynamics and quantum thermal baths) is provided. The overarching objective of this article is twofold: first, to clarify in which crystals and physical situations the disregard of QNE may incur in important bias and erroneous interpretations. And second, to promote the study and appreciation of QNE, a topic that traditionally has been treated in the context of condensed matter physics, within the broad and interdisciplinary areas of materials science.

DOI: 10.1103/RevModPhys.89.035003

CONTENTS

*c.cazorla@unsw.edu.au
†jordi.boronat@upc.edu

I. INTRODUCTION

A. Quantum crystals: Definition and interests

Quantum crystals are characterized by light-weight particles interacting through weak long-range forces. At low temperatures, the kinetic energy per particle in a quantum crystal E_k is much larger than k_BT, where k_B is the Boltzmann constant, and the spatial fluctuations about the equilibrium lattice sites are up to 30% of the distance to the neighboring lattice sites (that is, much larger than in any classical solid). These qualities can be understood only in terms of quantum-mechanical arguments. Consider, for instance, the quantum expression of the atomic kinetic energy for a system of N indistinguishable particles with mass m:

$$E_k = -\frac{\hbar^2}{2m}\left\langle \frac{\nabla^2\Psi}{\Psi}\right\rangle, \tag{1}$$

where $\hbar$ is the Planck constant, Ψ is the ground-state wave function of the system, and $\langle\cdots\rangle$ denotes expected value. If the lightweight particles were to rest immobile on the positions of the crystal arrangement $\mathbf{R}_0$ that minimizes their potential energy E_p, that is, $\Psi \propto \sqrt{\delta(\mathbf{R}-\mathbf{R}_0)}$, E_k would diverge. Rather, particles in a quantum crystal remain fluctuating around such equilibrium lattice sites in order to minimize their total energy $E = E_p + E_k$. The corresponding degree of spatial delocalization is determined by a subtle balance between the accompanying gains in kinetic and potential energies.

Examples of quantum solids include Wigner crystals (Wigner, 1934; Ceperley and Alder, 1980; Drummond *et al.*, 2004; Militzer and Graham, 2006; Drummond and Needs, 2009), vortex lattices (Safar *et al.*, 1992; Abo-Shaeer *et al.*, 2001; Cooper, Wilkin, and Gunn, 2001), dipole systems (Astrakharchik *et al.*, 2007; Matveeva and Giorgini, 2012; Boninsegni, 2013a; Moroni and Boninsegni, 2014), rare gases, molecular solids, light metals, and many other similar systems (see the next paragraphs). For the sake of focus, however, in this review we will concentrate on quantum crystals formed by atoms and small molecules.

A quantitative indicator of the degree of quantumness of a system is given by the de Boer parameter Λ^* (Sevryuk, Toennies, and Ceperley, 2010). This is defined as the ratio of the corresponding de Broglie wavelength $\lambda(\epsilon)$ and a typical interatomic distance r_0, namely,

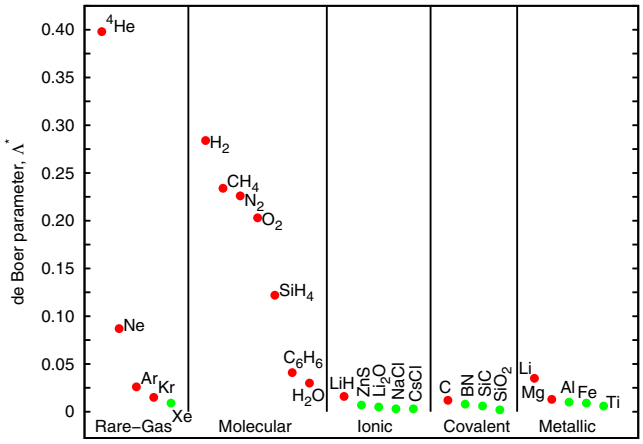

FIG. 1. de Boer parameter estimated in a series of crystals spanning over the entire range of solid-state species. The cases in which Λ^* adopts a value larger than 0.012, namely, C and above, are indicated with red (dark) dots.

$$\Lambda^* = \frac{\lambda(\epsilon)}{r_0} = \frac{\hbar}{r_0\sqrt{m\epsilon}}, \tag{2}$$

where ϵ is an energy scale characterizing the interactions between particles. The smaller m and ϵ are, the larger Λ^* results. Figure 1 shows the de Boer parameter estimated in a series of crystals that are representative of the broad spectrum of solid-state species.[1] The crystals in which quantum nuclear effects (QNE) are expected to be large, somewhat arbitrarily defined here as $\Lambda^* \geq 0.012$ (which in the limiting case coincides with graphite), are indicated with red (dark) dots. As observed, most rare gases and light-weight molecular solids, among which we highlight helium, hydrogen, and methane, are quantum crystals. An important number of quantum specimens are also found in the remnant of solid-state categories such as, for instance, metal hydride (ionic), carbon-based (covalent), and alkali metal (metallic) compounds.

Quantum paraelectrics, although not included in Fig. 1, also conform to an intriguing class of quantum crystals. Quantum paraelectrics are materials in which the onset of ferroelectricity, that is, the appearance of a spontaneous and externally switchable electrical polarization, is suppressed by quantum nuclear fluctuations (Müller and Burkard, 1979; Rytz, Hochli, and Bilz, 1980; Conduit and Simons, 2010). Examples of quantum paraelectrics include $SrTiO_3$ and $KTaO_3$, which normally are classified as complex oxide perovskites (Ohtomo and Hwang, 2004; Cazorla and Stengel, 2012). Quantum paraelectrics do not follow the conventional definition of a quantum crystal since they contain heavy atomic species that interact through strong covalent and ionic forces. Actually, the size of QNE in these materials should be rather small (i.e., $\Lambda^* \ll 0.01$). At low temperatures, however, quantum paraelectrics are on the verge of a phase transition involving

[1] Λ^* values were calculated using reported Lennard-Jones potential parameters for "rare gas" and "molecular" solids. In the rest of the cases, we used reported experimental cohesive energies as ϵ's and equilibrium lattice parameters as r_0's.

disparate crystal structures with very similar energies and thus the impact of QNE in these and other related materials is large (see Sec. IX).

The study of quantum solids is important to understand nature. Hydrogen and helium, for instance, are the most abundant elements in the Universe; they represent ∼70%–95% of the mass of the giant planets in our Solar System such as Jupiter and Saturn (Fortney, 2004; Baraffe, Chabrier, and Barman, 2010). An exhaustive knowledge of their condensed matter phases at extreme thermodynamic conditions is then crucial for understanding the chemical composition and past and future evolution of planetary bodies. Quantum solids are also sought after for technological applications. Rare-gases alloys, for instance, are intensively employed as pressure-transmitting media in high-load compression experiments and synthesis processes, due to their intriguing elastic properties (Errandonea *et al.*, 2006; Dewaele *et al.*, 2008; Cazorla, Errandonea, and Sola, 2009).

Other examples of scientific fields in which quantum crystals are important include nuclear energy, gas storage, quantum computing, and nanoelectronics. For instance, lithium hydride (LiH) and deuteride (LiD) are thoroughly used in the nuclear industry as either shielding agents or fuel in energy reactors (Welch, 1974; Veleckis, 1977). Metal hydrides are also promising for hydrogen storage applications (Grochala and Edwards, 2004; Shevlin and Guo, 2009) since they can supply large amounts of gas upon thermodynamic destabilization. Likewise, carbon-based nanostructures (e.g., graphene, nanotubes, and fullerenes) exhibit large gas uptake capacities (Cazorla, Shevlin, and Guo, 2011; Cazorla, 2015; Gadipelli and Guo, 2015) as a consequence of their large surface-to-volume ratio, light atomic weight, and great thermodynamic stability. Diamonds with negatively charged nitrogen-vacancy centers, another type of carbonaceous nanomaterial, play a crucial role in the development of scalable quantum computing components (Fuchs *et al.*, 2011; Nemoto *et al.*, 2014). This class of crystals can also be employed as tunable *quantum simulators* that, in analogy to ultracold atom gases trapped in optical lattices (Lewestein *et al.*, 2007), can be used to answer fundamental questions in the fields of condensed matter, biology, and high-energy physics (Georgescu, Ashhab, and Nori, 2014; Wang *et al.*, 2015). Finally, quantum paraelectrics find numerous applications in nanoelectronics as varistors, supercapacitor electrodes, and substrates on which to grow epitaxial films of other perovskite compounds (Lawless, 1974; Schlom *et al.*, 2007; Cazorla and Stengel, 2012).

Besides their fundamental and applied interests, quantum crystals are also important in the framework of development and testing of new theories. The interactions between particles in quantum crystals typically are of dispersion, hydrogen bond, and multipole-multipole types, which are long ranged and weak. The cohesion between atoms in solid helium, for instance, is so weak that to a first approximation this crystal can be described by a system of hard spheres (Kalos, Levesque, and Verlet, 1974). Nevertheless, the description of long-ranged and very weak interactions poses a serious challenge to some families of first-principles methods (also known as *ab initio* because they do not rely on any predetermined knowledge of the atomic forces) as the analytical expression of the corresponding electronic exchange and correlation energies are intricate and difficult to approximate for computational purposes (Klimeš and Michaelides, 2012; Cazorla, 2015). This circumstance converts quantum solids into an ideal playground in which to perform benchmark calculations for assessing the performance of standard and advanced electronic band-structure first-principles methods such as density functional theory (DFT) and the electronic quantum Monte Carlo (eQMC) method (Driver *et al.*, 2010; Henning *et al.*, 2010; Clay *et al.*, 2014, 2016) (see Sec. III.A).

Likewise, QNE must be fully accounted for in any study dealing with quantum solids since they may noticeably affect the most fundamental properties of crystals such as atomic structure, vibrational phonon excitations, magnetic spin order, and electronic energy band gap. This fact leads to the situation in which approaches describing QNE only at a qualitative or approximate level (e.g., the Debye model and quasiharmonic approximation) normally are inadequate for investigating genuine quantum crystals [as shown, for example, by Morales *et al.* (2013), Monserrat *et al.* (2014), and Cazorla and Boronat (2015a)]; instead, anharmonic or full quantum approaches based on the solution to the Schrödinger equation or path-integral formulation of quantum mechanics due to Feynman (1948) has to be employed (the fundamentals of some of these simulation techniques are reviewed in Sec. II).

B. A bit of history and theory

The experimental study of quantum solids was initiated with the solidification of ^{4}He at the Kamerlingh Onnes Laboratories in Leiden, by W. H. Keesom in June 1926 (Keesom, 1942; Domb and Dugdale, 1957). It was not until the late 1960s and early 1970s, however, that with the establishment of neutron inelastic scattering techniques solid helium started being thoroughly investigated (Klein and Venables, 1974). The aim of those early neutron inelastic scattering experiments (Lipschultz *et al.*, 1967; Minkiewicz *et al.*, 1968) was to understand the vibrational properties of such a highly anharmonic solid. Actually, harmonic calculations render a mechanically unstable solid (that is, with imaginary lattice phonon frequencies) at low densities (Wette and Nijboer, 1965), hence it was appealing to rationalize the real dynamics in the crystal. An interest in understanding how hydrostatic pressure could modify the physical properties of quantum solids started to develop also at that time (Eckert, Thomlinson, and Shirane, 1977; Stassis *et al.*, 1978).

Likewise, the initial theoretical efforts were concentrated in finding a theory that could correctly describe the dynamical stability observed in highly anharmonic crystals. This was accomplished with the development of the self-consistent phonon (SCP) theory (Koehler, 1966; Glyde, 1994). In the SCP approach, one essentially assumes a harmonic solid with force constants that best represent the real anharmonic crystal, which are determined on the basis of a variational principle. We note that in recent years variants of the SCP method and other related but more advanced approaches (e.g., the vibrational self-consistent-field method) have been applied with success to the study of highly anharmonic metallic, molecular, and superconductor materials in the context of electronic

first-principles calculations [see, for instance, Errea, Rousseau, and Bergara (2011), Errea, Calandra, and Mauri (2013), Monserrat and Needs (2014), Engel, Monserrat, and Needs (2015), Errea *et al.* (2015), and Paulatto *et al.*, 2015].

In quantum crystals, due to the large excursions of the atoms around the equilibrium positions, a good treatment of the short-range correlations is necessary. The need to consider such microscopic effects, which are beyond the extent of harmonic and quasiharmonic approaches, led to the development of the variational theory of quantum solids (Nosanow, 1966; Koehler, 1967). Nosanow proposed a general wave function model for a quantum solid of the form

$$\Psi(\mathbf{r}_1,\ldots,\mathbf{r}_N;\{\mathbf{R}_I\}) = \prod_{j<k} f(r_{jk}) \prod_{i=1}^{N} g(|\mathbf{r}_i - \mathbf{R}_i|), \quad (3)$$

where $\mathbf{R}_I$ are the position vectors defining the equilibrium crystal lattice, $\mathbf{r}_i$ are the position vectors of the particles, $r_{jk} \equiv |\mathbf{r}_j - \mathbf{r}_k|$, and $g(r)$ and $f(r)$ are Gaussian and two-body correlation factors, respectively. The second factor in Eq. (3) localizes each particle around a particular equilibrium lattice site, while the first accounts for the interparticle correlations introduced by the atomic interactions.

After McMillan's and other works on liquid ^{4}He (McMillan, 1965; Schiff and Verlet, 1967), the two-body correlation factors in Ψ are frequently expressed as $f(r) = \exp[-(1/2)(b/r)^5]$. This function corresponds to the asymptotic solution of the Schrödinger equation in the $r \to 0$ limit of a two-body problem in which the interparticle interaction is of the Lennard-Jones (LJ) type. With such a relatively simple analytical model of Ψ and by employing Monte Carlo multidimensional integration techniques (Metropolis *et al.*, 1953; Wood and Parker, 1957), it was then possible to perform variational calculations in the ground state of solid helium (Hansen and Levesque, 1968) and other quantum solids (Hansen, 1968; Bruce, 1972). These advancements set the foundation of the variational Monte Carlo (VMC) method as applied to the study of quantum solids (see Sec. II.A.1).

Despite the fact that variational approaches may be insightful from a physical point of view, they rarely provide the exact quantitative answer to realistic problems. In order to obtain the precise solution to a quantum many-body problem, one, for instance, may deal explicitly with the corresponding Schrödinger equation. To this end, more sophisticated techniques than VMC, albeit related, were developed during the 1970s, among which we highlight the Green's function Monte Carlo (GFMC) method due to Kalos and co-workers (Kalos, 1962; Kalos, Levesque, and Verlet, 1974; Ceperley, Chester, and Kalos, 1976; Whitlock and Kalos, 1979; Whitlock *et al.*, 1979; Schmidt and Kalos, 1984). The basic idea behind the GFMC method is to employ Monte Carlo sampling techniques to solve the time-independent Schrödinger equation of a many-body system, when that is expressed as an integral equation containing a Green's function. Although the exact form of the Green's function normally is not known, this can be reproduced with stochastic sampling techniques involving probability distribution functions generated through the Trotter's product formula (Trotter, 1959); see Sec. II.A.2.

An intimately related method to the GFMC method is the diffusion Monte Carlo (DMC) method, in which the imaginary time-dependent Schrödinger equation, rather than the time-independent one, is integrated by using an analytical short-time approximation to the Green's function (Ceperley and Alder, 1980; Reynolds *et al.*, 1982; Guardiola, 1986; Hammond, Lester, and Reynolds, 1994). Both the GFMC and DMC methods are exact ground-state methods in the sense that they provide results for the energy that in principle are affected only by statistical errors. These two methods belong to the family known as "projection techniques," in which a projector operator is iteratively applied in order to cast out the ground state of the targeted quantum many-body system [in this latter category we also find, for instance, the reptation Monte Carlo method due to Baroni and Moroni (1999)]. Nonetheless, the DMC method is more efficient in dealing with arbitrary boundary conditions and potential-energy functions (Anderson, 2002); hence the use of the GFMC method is infrequent nowadays. In Sec. II.A.2, we review the fundamentals of the DMC method as applied to the study of quantum bosonic crystals.

Quantum nuclear effects are also crucial to understand quantum solids at finite temperature (i.e., $T \neq 0$). The threshold temperature below which QNE are important can be considered to be equal to the Debye temperature Θ_D (Born and Huang, 1954). Θ_D is defined as $\hbar\omega_m/k_B$, where ω_m is the largest vibrational frequency in the crystal (that is, at $\Theta_D \leq T$ all phonon modes in the solid are excited). This threshold temperature can be obtained directly from neutron inelastic scattering or specific heat measurements, and in the particular case of rare gases Θ_D ranges from 25 to 85 K. It is important to note that Θ_D can increase dramatically under the application of external pressure, hence making unavoidable the consideration of QNE in the study of highly compressed quantum crystals. In molecular hydrogen, for instance, the Debye temperature at normal pressure conditions amounts to ~100 K, whereas at $P = 20$ GPa it turns out to be ~1000 K (Diatschenko *et al.*, 1985).

The theoretical method of choice for simulation of quantum solids at $T \neq 0$ is the path-integral Monte Carlo (PIMC) method. The PIMC method is based on Feynman's formulation of nonrelativistic quantum mechanics, which can be thought of as a generalization of the action principle of classical mechanics (Feynman, 1948; Feynman and Hibbs, 1965). In Feynman's path-integral theory, however, a functional integral over an infinity of possible trajectories (that is, a path integral) replaces the notion of probability amplitude. From a computational perspective, Feynman's formalism allows one to map out the atomic quantum system of interest onto a classical model of interacting polymers that evolve in imaginary time. This idea, which is known as the "classical isomorphism" (Feynman, 1972; Barker, 1979; Chandler and Wolynes, 1981; Ceperley, 1995), makes it possible to sample the corresponding space of possible configurations with stochastic techniques, laying the foundations of the PIMC method. The PIMC method relies exclusively on the knowledge of the many-body Hamiltonian and, in contrast to other simulation techniques such as, for instance, the GFMC and

DMC methods, does not comprise the use of projector operators (this method is explained in detail in Sec. II.B.1). Interestingly, the PIMC approach can be generalized to zero-temperature calculations by exploiting the formal similarities between imaginary time propagators and thermal density matrices (Sarsa, Schmidt, and Magro, 2000). This methodological extension is named path-integral ground state (PIGS) and is reviewed in Sec. II.A.3.

The isomorphism between classical and quantum systems also allows one to employ molecular dynamics (MD) simulation techniques for the sampling of path integrals (Chakravarty, 1997; Tuckerman and Hughes, 1998). In this last framework, generally known as path-integral molecular dynamics (PIMD), the atoms are treated as distinguishable particles. Consequently, genuine quantum statistical effects, that in liquids and disordered systems may give rise to intriguing quantum phenomena such as Bose-Einstein condensation (BEC) and superfluidity at low temperatures, are neglected. Nonetheless, in situations in which atomic quantum exchanges are not relevant (i.e., high temperatures) the PIMD formalism becomes a powerful method that can be used, for instance, to compute quantum time-correlation functions and transition state rates very efficiently (Gillan, 1990; Habershon *et al.*, 2013; Herrero and Ramírez, 2014).

Recently, an alternative to path-integral quantum simulation approaches has been proposed that relies on the combined action of "quantum thermal baths" (QTB) and molecular dynamics (Wang, 2007; Buyukdagli, Savin, and Hu, 2008; Dammak *et al.*, 2009; Hernández-Rojas, Calvo, and González-Noya, 2015). In the QTB formalism, the dynamics of the system is governed by a Langevin-type equation including dissipative and Gaussian random forces that mimics the power spectral density given by the quantum fluctuation-dissipation theorem (Callen and Welton, 1951). Although quantum statistical effects are also neglected in QTB approaches, these methods have become more popular in recent years due to their reduced computational expense as compared to path-integral based techniques. Meanwhile, hybrid PIMD and QTB schemes have been recently developed that exhibit improved convergence and scalability as compared to the PIMD scheme alone (Ceriotti, Bussi, and Parrinello, 2009; Ceriotti, Manolopoulos, and Parrinello, 2011; Ceriotti and Manolopoulos, 2012; Brieuc, Dammak, and Hayoun, 2016). In Sec. II.B, we provide a brief introduction to these emergent quantum simulation techniques.

C. Quantum versus classical solids

Let us take a deeper look into the main differences between classical and quantum solids in the zero-temperature limit (see Fig. 2). Atoms in a classical solid remain practically immobile on the positions of the periodic arrangement that minimizes their potential energy (i.e., $E_k \ll k_B T$), whereas in a quantum solid particles remain loosely localized around those sites (i.e., $E_k \gg k_B T$). As a consequence, large Lindemann ratios (i.e., $\gamma \equiv \sqrt{\langle u^2 \rangle}/a$, where $\langle u^2 \rangle$ represents the atomic mean squared displacement and a the lattice parameter) of the order of ~ 0.1 are observed in the latter case. Also, the radial pair distribution function $g(r)$ (i.e., the average number density at a distance r from an atom divided by the overall particle density) presents

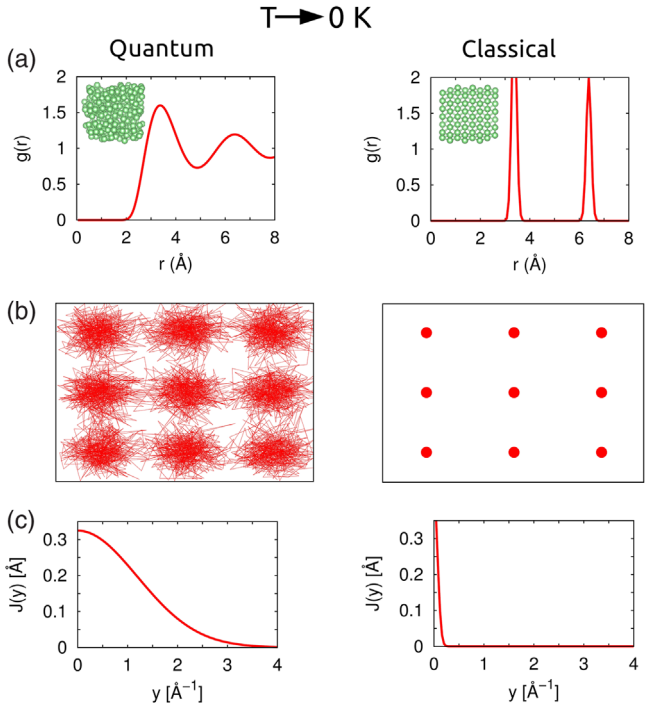

FIG. 2. Sketch of the main differences between quantum (left) and classical (right) solids in the zero-temperature limit. (a) Radial pair distribution function $g(r)$. (b) Localization of the atoms around their equilibrium lattice positions; in the quantum case, lines represent the evolution of the atomic positions along time and show the occurrence of atomic quantum exchanges. (c) Compton profile of the longitudinal momentum distribution $J(y)$.

different features in the two types of crystals. In the zero-temperature limit, the $g(r)$ of a classical solid exhibits a series of sharp peaks signaling the radial distances between crystal lattice sites. By contrast, in a quantum solid $g(r)$ is continuous and displays a pattern of peaks and valleys that oscillates around unity at large distances [see Fig. 2(a)]. Likewise, the structure factor in a quantum solid, which is related to the Fourier transform of $g(r)$, presents some broadening and depletion of the main scattering amplitudes as compared to that in a classical solid (Whitlock *et al.*, 1979; Draeger and Ceperley, 2000).

A further difference between quantum and classical crystals is provided by the momentum distribution $n(\mathbf{k})$. In classical solids, $n(\mathbf{k})$ is always (that is, independently of the interactions between the atoms) equal to the Maxwell-Boltzmann distribution:

$$n(\mathbf{k})^{\text{class}} = \left(\frac{1}{2\pi\hat{\alpha}_2}\right)^{3/2} \exp\left[-\frac{\mathbf{k}^2}{2\hat{\alpha}_2}\right], \tag{4}$$

where by the equipartition theorem $\hat{\alpha}_2 \equiv m k_B T/\hbar^2$. In quantum solids, however, the momenta and positions of the atoms are not independent and consequently $n(\mathbf{k})$ may depart significantly from $n(\mathbf{k})^{\text{class}}$. In solid ^{4}He, for instance, $n(\mathbf{k})$ is non-Gaussian as it has a larger occupation of low momentum states in comparison to a Maxwell-Boltzmann distribution (Diallo *et al.*, 2004; Rota and Boronat, 2011).

The atomic momentum distribution of condensed matter systems can be measured by inelastic neutron scattering performed at high momentum transfer (Glyde, 1994; Diallo *et al.*, 2007). In this case, the Compton profile of the longitudinal momentum distribution $J(y)$ is the quantity that is directly measured that in the impulse approximation is related to $n(\mathbf{k})$ through (Withers and Glyde, 2007)

$$J(y) = 2\pi \int_{|y|}^{\infty} dk k n(\mathbf{k}), \tag{5}$$

where y is a scaling variable. Compton profile experiments can provide a wealth of information about the nature of quantum solids (Glyde, 1994). For instance, recent neutron scattering measurements have found that the atomic kinetic energy in solid helium at $T \approx 0$ amounts to 24.25 (0.30) K (the number within parentheses represents the accompanying uncertainty) (Diallo *et al.*, 2007), which is in good agreement with quantum Monte Carlo estimations (Ceperley, Simmons, and Blasdell, 1996; Cazorla and Boronat, 2008a; Vitiello, 2011).

Kinetic isotopic effects, which attribute different kinetic energies to the isotopes of the same chemical element [see Eq. (1)], are also indicators of the presence of QNE. The magnitude of these effects can actually be inferred from functions $g(r)$ and $n(\mathbf{k})$ (Boninsegni, Pierleoni, and Ceperley, 1994; Mao and Hemley, 1994; Cazorla and Boronat, 2005). For instance, narrowing (widening) of the $g(r)$ peaks may be caused by the presence of heavier (lighter) species. Kinetic isotopic effects can also manifest in the thermal expansion of quantum solids (Herrero and Ramírez, 2011a; Pamuk *et al.*, 2012) and the $P-T$ boundaries delimiting the stability regions between different phases (Lorenzana, Silvera, and Goettel, 1990; Goncharov, Hemley, and Mao, 2011).

In quantum mechanics, atoms of the same species are indistinguishable, that is, they can exchange positions while leaving the configuration of the system (namely, the square of the wave function) invariant. These atomic exchanges can occur as pairwise interchanges, three-particle, four-particle, and so on cyclic permutations. When the particles involved in such permutations are bosons and their number grows to infinity, the system becomes superfluid and the atoms on it can flow coherently without any resistance (Feynman, 1972; Ceperley, 1995). In quantum solids, as opposed to classical crystals, atoms can swap their positions and further delocalize in configurational space [see Fig. 2(b) for a schematic representation]. An illustrative example of this class of QNE is given by solid ^{3}He. ^{3}He atoms, which are fermions, have a nonzero magnetic moment and at low pressure the stable phase is a cubic bcc crystal. At temperatures below 1.5 mK, this system adopts an exotic magnetic order that consists of two planes of up spins followed by two planes of down spins (Roger, Hetherington, and Delrieu, 1983). In terms of classical interaction arguments, that is, if only nearest-neighbor pair exchanges were important, the magnetic order in this crystal should be antiferromagnetic. However, quantum exchanges between more than two ^{3}He atoms are very frequent and as a result a strong competition between ferromagnetism and antiferromagnetism appears in the crystal that leads to the observed magnetic order (Ceperley, 1995).

It has been theoretically shown that in *commensurate* ^{4}He crystals (i.e., crystals with exactly two atoms per hcp unit cell, without any point or line defects such as vacancies, dislocations, or grain boundaries) typical cyclic permutations occurring at a few tenths of K involve only a small number of atoms. Consequently, the superfluid density in perfect quantum solids is null (Ceperley and Bernu, 2004; Bernu and Ceperley, 2005; Boninsegni, Prokof'ev, and Svistunov, 2006b). This conclusion appears to be consistent with the results of most recent and conclusive torsional oscillator experiments performed by Kim and Chan (2012, 2014). Meanwhile, in the presence of crystalline defects or atomic disorder, quantum Monte Carlo calculations agree in predicting that the length of the ring quantum exchanges increases noticeably, and thus the possibility of realizing superfluidity starts to depart from zero (Boninsegni, Prokof'ev, and Svistunov, 2006b; Boninsegni *et al.*, 2007; Rota and Boronat, 2012). We must note, however, that convincing experimental evidence of superfluidlike manifestations in quantum crystals is yet elusive (Chan, Hallock, and Reatto, 2013; Hallock, 2015). We discuss these topics in more detail in Sec. VI.

D. Incomplete understanding of quantum crystals

Although a lot is already known about the physics of quantum crystals, there are still a few puzzling and controversial aspects that urge for an improved understanding. One of these aspects is related to the interactions between different types of crystalline defects, their formation energy, and transport properties. In a seminal work, Day and Beamish (2007) reported the experimental dependence of the shear modulus μ in solid ^{4}He as a function of temperature. They found that μ increased with decreasing T below a certain temperature of 0.15 K. The observed increase in stiffness was rationalized in terms of line defects mobility: below a particular temperature threshold the dislocations present in the crystal could be pinned by ^{3}He impurities in spite of the incredibly small concentration of the latter (i.e., just 200 ppb of ^{4}He atoms). This argument has been subsequently ratified by a number of compelling experimental works carried out by the groups of Beamish, at the University of Alberta, and Balibar, at the Ecole Normale Supérieure de Paris [see, for instance, Haziot, Fefferman, Souris *et al.* (2013), Haziot, Fefferman, Beamish, and Balibar (2013), Fefferman *et al.* (2014), and Souris *et al.* (2014)]. Remarkably, Haziot *et al.* (2013a) recently showed that in ultrapure single crystals of ^{4}He the resistance to shear along one particular direction nearly vanishes at around $T = 0.1$ K, whereas normal elastic behavior is observed in the others. The exact origins of this intriguing effect, which has been termed "giant plasticity," however, are still under debate (Haziot *et al.*, 2013b; Zhou *et al.*, 2013), and the exact ways in which dislocations and isotopic impurities interact are not yet fully understood (see Fig. 3).

Recent theoretical arguments by Kuklov *et al.* (2014) suggest that quantum crystals might constitute a unique kind of material in which topological lattice defects, that is,

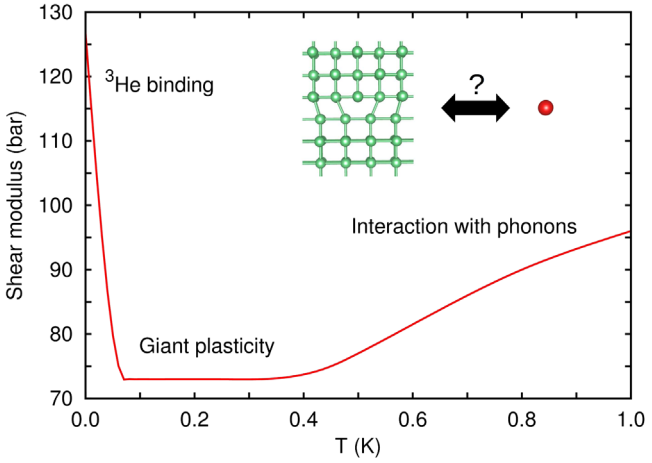

FIG. 3. Shear modulus in an extremely pure ^{4}He crystal expressed as a function of temperature. Three different regimes are observed that can be explained in terms of dislocation dynamics (see text). The unsolved problem about which are the interactions between dislocations and isotopic impurities is noted schematically. Adapted from Haziot *et al.*, 2013a.

dislocations, could display quantum behavior such as quantum tunneling of kinks and jogs. Kuklov's hypotheses appear to be sustained by recent experimental observations in ^{4}He and ^{3}He crystals [see, for instance, Ray and Hallock (2008) and Lisunov *et al.* (2015)]. Verifying such a possible quantum scenario, however, turns out to be very challenging in practice due to the difficulties encountered in both the experiments and atomistic simulations. For instance, according to recent reports it appears to be extremely challenging to grow perfect helium crystals totally free of dislocations (Souris *et al.*, 2015). Concerning the calculations, a detailed and reliable simulation of line defects entails the use of large systems containing up to several thousands of atoms (Bulatov and Cai, 2006; Proville, Rodney, and Marinica, 2012), which currently is on the edge of quantum simulations. Because of these issues, many fundamental questions remain yet unanswered such as, for instance: What is the formation energy of dislocations in quantum solids and by which mechanisms are these created? Can dislocations really behave as quantum entities so that they delocalize in space? Through which exact mechanisms do quantum impurities such as ^{3}He atoms, which are extremely mobile, interact with dislocations? Solving these and other similar puzzles is crucial for advancing the field of quantum solids; this knowledge could also have an impact on particular areas of materials science in which plasticity is important (e.g., fatigue in crystals and amorphous and martensitic transformations) (Proville, Rodney, and Marinica, 2012). We comment further on these points in Sec. VI.

Another source of unawareness in quantum crystals is posed by their behavior at extreme thermodynamic conditions. When a crystal is compressed the bonds between atoms normally are shortened so that particles become more localized to avoid increasing their (highly repulsive) potential energy. At the same time, the kinetic energy of the solid increases due to Heisenberg's uncertainty principle. In quantum crystals, such a pressure-induced energy gain may be compensated in part by quantum atomic exchanges and quantum tunneling, which tend to favor the delocalization of particles (Kosevich, 2005). The existence of proton quantum tunneling, for instance, has been demonstrated in solid hydrogen and ice under pressure, a quantum nuclear effect that is key to understanding their corresponding phase diagrams and vibrational properties (Benoit, Marx, and Parrinello, 1998; Hemley, 2000; Howie, Scheler *et al.*, 2012; Drechsel-Grau and Marx, 2014). On the other hand, quantum fluctuations in highly compressed solid hydrogen are known to hinder molecular rotation, which counterintuitively leads to some kind of atomic localization (Kitamura *et al.*, 2000; Li *et al.*, 2013). The ways in which QNE manifest and affect the physical properties of highly compressed quantum crystals actually seem to be quite unpredictable.

Simulation of QNE phenomena at high pressures is technically difficult and demands intensive computational resources. The main reason for this is that the interactions between atoms can no longer be correctly described with semiempirical approaches such as, for instance, pairwise potentials, and thereby the treatment of both the electronic and ionic degrees of freedom needs to be done quantum mechanically (see Sec. III). Likewise, carrying out high-P, high-T experiments in the laboratory is extremely challenging due to the occurrence of unwanted chemical reactions between the samples and containers (Dewaele *et al.*, 2010). In addition to this, it is complicated to determine the exact atomic structure in highly compressed solids with low-Z numbers because their x-ray scattering cross sections are very small (Dzyabura, Zaghoo, and Silvera, 2013; Goncharov, Howie, and Gregoryanz, 2013). Because of all these difficulties, the $P-T$ phase diagram of many quantum solids remains contentious and a complete understanding of the accompanying QNE features (e.g., quantum atomic exchanges and kinetic energy) is still pending. Further progress in this field is essential for advancing our knowledge in condensed matter physics and Earth and planetary sciences (see Sec. VIII for more details).

E. Aims and organization of this review

This review is concerned with the simulation and understanding of quantum solids formed by atoms and small molecules under broad $P-T$ conditions. Important aspects in these systems such as, for instance, their energetic and structural properties, phase transitions, and elasticity are discussed in detail. The effects that crystalline defects and reduced dimensionality have on the physical properties of archetypal quantum solids (i.e., ^{4}He and H_2) are also reviewed. Special emphasis is put on identifying those systems and physical situations in which QNE should be considered in order to avoid likely misconceptions. In fact, QNE have traditionally been analyzed in the field of condensed matter physics; however, comprehension of this class of effects is also crucial for the advancement of many other research areas such as planetary and materials sciences.

We start by explaining the basics of the simulation methods that are used most frequently in the study of quantum crystals (Secs. II and III). In Secs. IV–IX, we describe the phenomenology and current understanding of quantum solids by

surveying a large number of experimental and theoretical studies on archetypal and other less popular quantum crystals (e.g., H_2O, N_2, CH_4, LiH, and $BaTiO_3$). Finally, we comment on promising research directions involving quantum solids and summarize our general conclusions in Sec. X.

II. QUANTUM SIMULATION METHODS

We review the basics of customary quantum simulation methods that are employed for the investigation of quantum crystals. We classify them into two major categories, namely, ground-state ($T = 0$) and finite-temperature ($T \neq 0$) methods. In the zero-temperature case, we differentiate between "approximate" and "exact" techniques. Depending on the nature of the problem that is going to be investigated and the amount of computational resources that are available, one may opt for using one or the other.

A. Ground-state approaches

1. Approximate methods

a. Quasiharmonic approximation

In the quasiharmonic approach (QHA) one assumes that the potential energy of a crystal can be approximated with a quadratic expansion around the equilibrium atomic configuration of the form (Born and Huang, 1954; Kittel, 2005)

$$E_{\mathrm{qh}} = E_{\mathrm{eq}} + \frac{1}{2}\sum_{l\kappa\alpha,l'\kappa'\alpha'} \Phi_{l\kappa\alpha,l'\kappa'\alpha'} u_{l\kappa\alpha} u_{l'\kappa'\alpha'}, \tag{6}$$

where E_{eq} is the total energy of the perfect lattice, Φ is the corresponding force-constant matrix, and $u_{l\kappa\alpha}$ is the displacement along the Cartesian direction α of atom κ at lattice site l. Normally, this dynamical problem is solved by introducing

$$u_{l\kappa\alpha}(t) = \sum_{q} u_{q\kappa\alpha} \exp\{i[\omega t - \boldsymbol{q}\cdot(\boldsymbol{l} + \boldsymbol{\tau}_\kappa)]\}, \tag{7}$$

where $\boldsymbol{q}$ is a wave vector in the first Brillouin zone (BZ) that is defined by the equilibrium unit cell; $\boldsymbol{l} + \boldsymbol{\tau}_\kappa$ is the vector that locates atom κ at cell l in the equilibrium structure. The normal modes are then found by diagonalizing the dynamical matrix:

$$D_{\boldsymbol{q};\kappa\alpha,\kappa'\alpha'} = \frac{1}{\sqrt{m_\kappa m_{\kappa'}}} \sum_{l'} \Phi_{0\kappa\alpha,l'\kappa'\alpha'} \exp[i\boldsymbol{q}\cdot(\boldsymbol{\tau}_\kappa - \boldsymbol{l}' - \boldsymbol{\tau}_{\kappa'})], \tag{8}$$

and thus the crystal can be treated as a collection of noninteracting harmonic oscillators with frequencies $\omega_{\boldsymbol{q}s}$ (positively defined and nonzero) and energy levels:

$$E^n_{\boldsymbol{q}s} = (\tfrac{1}{2} + n)\omega_{\boldsymbol{q}s}, \tag{9}$$

where $0 \leq n < \infty$. In this approximation, the Helmholtz free energy of a crystal with volume V at temperature T is given by

$$F_{\mathrm{qh}}(V,T) = \frac{1}{N_q} k_B T \sum_{\boldsymbol{q}s} \ln\left[2\sinh\left(\frac{\hbar\omega_{\boldsymbol{q}s}(V)}{2k_{\mathrm{B}}T}\right)\right], \tag{10}$$

where N_q is the total number of wave vectors used for integration over the BZ, and the V dependence of the vibrational frequencies has been noted explicitly. In the zero-temperature limit, Eq. (10) transforms into

$$F_{\mathrm{qh}}(V,0) = \frac{1}{N_{\mathrm{q}}} \sum_{\boldsymbol{q}s} \frac{1}{2}\hbar\omega_{\boldsymbol{q}s}(V), \tag{11}$$

which is usually referred to as the "zero-point energy" (ZPE). We note that despite quasiharmonic approaches may not be adequate for the study of archetypal quantum solids (Morales *et al.*, 2013; Monserrat *et al.*, 2014; Cazorla and Boronat, 2015a), QHA ZPE corrections normally are decisive in predicting accurate phase transitions in other materials (Cazorla, Alfè, and Gillan, 2008; Shevlin, Cazorla, and Guo, 2012; Cazorla and Íñiguez, 2013).

b. Variational Monte Carlo method

Variational theory has been one of the most fruitful computational approaches to study quantum fluids and solids. The strong repulsive interaction at short distances between particles produces a failure of conventional perturbation methods. The variational principle of quantum-mechanics states that the expectation value of a Hamiltonian $\hat{H}$ obtained with a model wave function $|\Psi\rangle$ provides an upper bound to the true ground-state energy of the system E_0, namely,

$$E = \frac{\langle\Psi|\hat{H}|\Psi\rangle}{\langle\Psi|\Psi\rangle} \geq E_0. \tag{12}$$

In a many-body system, the evaluation of E is not an easy task because one has to deal with a $3N$-dimensional integral. In this context, Monte Carlo integration techniques emerge as one of the most efficient computational methods. In the VMC method, one defines the multivariate probability density function (pdf):

$$f(\boldsymbol{R}) = \frac{|\Psi(\boldsymbol{R})|^2}{\int d\boldsymbol{R}|\Psi(\boldsymbol{R})|^2}, \tag{13}$$

which is normalized and positively defined. Meanwhile, the expectation value of the Hamiltonian can be expressed in the following integral form:

$$\langle\hat{H}\rangle_\Psi = \int d\boldsymbol{R} E_{\mathrm{L}}(\boldsymbol{R}) f(\boldsymbol{R}), \tag{14}$$

where the local energy E_{L} is defined as

$$E_{\mathrm{L}}(\boldsymbol{R}) = \frac{1}{\Psi(\boldsymbol{R})}\hat{H}\Psi(\boldsymbol{R}). \tag{15}$$

In Eqs. (14) and (15) $\boldsymbol{R}$ stands for a multidimensional point (also called the "walker"), $\boldsymbol{R} \equiv \{\boldsymbol{r}_1, \ldots, \boldsymbol{r}_N\}$. The expected value of the Hamiltonian then is calculated as the mean value of $E_{\mathrm{L}}(\boldsymbol{R})$, which is evaluated in a series of points n_s generated through the pdf $f(\boldsymbol{R})$, namely,

$$\langle \hat{H} \rangle_\Psi = \frac{1}{n_s} \sum_{i=1}^{n_s} E_L(\boldsymbol{R}_i). \tag{16}$$

Effective sampling of the multidimensional pdf $f(\boldsymbol{R})$ can be done with the Metropolis method (Metropolis *et al.*, 1953; Wood and Parker, 1957). Given a trial wave function $\Psi(\boldsymbol{R})$, the VMC method provides the exact $\langle \hat{H} \rangle_\Psi$ value to within statistical errors. Trial wave functions normally contain a set of parameters that are optimized in order to find the absolute minimum of $\langle \hat{H} \rangle_\Psi$. Alternatively, one can search for the parameter values that minimize the variance of the energy, whose lower bound *a priori* is known to be zero (Hammond, Lester, and Reynolds, 1994).

With regard to Bose crystals (that is, formed by boson particles), the most widely used wave function is the Nosanow-Jastrow (NJ) model:

$$\Psi_{NJ}(\boldsymbol{r}_1, \ldots, \boldsymbol{r}_N) = \prod_{i<j}^{N} f(r_{ij}) \prod_{i,I=1}^{N} g(r_{iI}), \tag{17}$$

where N is the number of particles and lattice sites, $f(r)$ is a two-body Jastrow correlation function, and $g(r)$ is a one-body localization factor that links particle i to site I (see Sec. I.B). The Jastrow factor takes into account, at the lowest order, the dynamical correlations between particles induced by the interatomic potential, whereas the one-body term introduces the symmetry of the crystal.

The wave function Ψ_{NJ} leads to an excellent description of the equation of state (eos) and structural properties of atomic quantum solids. However, it cannot be used to calculate properties that directly depend on the Bose-Einstein statistics (e.g., superfluidity and off-diagonal long-range order) because it is not symmetric under the exchange of particles. The latter symmetry requirement can be formally expressed as

$$\Psi_{PNJ}(\boldsymbol{r}_1, \ldots, \boldsymbol{r}_N) = \prod_{i<j}^{N} f(r_{ij}) \left(\sum_{P(J)} \prod_{i=1}^{N} g(r_{iJ}) \right), \tag{18}$$

where $P(J)$ indicates a sum over all possible particle permutations involving the lattice sites. This wave function model, however, is technically challenging in practice since the number of configurations that needs to be sampled to reach convergence grows exponentially with the number of particles.

Effective calculations involving a symmetric NJ wave function can be done with the model

$$\Psi_{SNJ}(\boldsymbol{r}_1, \ldots, \boldsymbol{r}_N) = \prod_{i<j}^{N} f(r_{ij}) \prod_{J=1}^{N} \left(\sum_{i=1}^{N} g(r_{iJ}) \right), \tag{19}$$

which was introduced by Cazorla *et al.* (2009). This symmetric wave function possesses a localization factor that suppresses lattice voids arising from double site occupancy, a desirable feature that also is reproduced by the wave function Ψ_{PNJ}.

Other symmetric wave functions have been proposed in the context of quantum solids that do not rely on the symmetrization of Ψ_{NJ}. These include a Bloch-like function (Ceperley, Chester, and Kalos, 1978), inspired in the band theory of electrons, and the shadow wave function (Galli, Rossi, and Reatto, 2005). The first model was introduced in a VMC study of the Yukawa system (Ceperley, Chester, and Kalos, 1978); the resulting variational energies, however, were significantly higher than those estimated with the nonsymmetric NJ wave function, and the creation of vacancies or double occupancy of the same lattice site in the crystal could not be prevented. Consequently, this model has been overlooked in subsequent studies. A more realistic symmetric model is provided by the shadow wave function (Vitiello, Runge, and Kalos, 1988; MacFarland *et al.*, 1994), which is defined as

$$\Psi_{sh}(\boldsymbol{r}_1, \ldots, \boldsymbol{r}_N) = \Phi_p(\boldsymbol{R}) \int d\boldsymbol{S} \Theta(\boldsymbol{R}, \boldsymbol{S}) \Phi_s(\boldsymbol{S}), \tag{20}$$

in which auxiliary variables $\boldsymbol{S}$ (also called "shadows") are introduced in order to avoid the explicit definition of any particular atomic arrangement. In Eq. (20), $\Phi_p(\boldsymbol{R})$ and $\Phi_s(\boldsymbol{S})$ are Jastrow factors that correlate particles and shadows separately; the function $\Theta(\boldsymbol{R}, \boldsymbol{S})$, on the other hand, introduces a coupling between particles and shadows. The shadow variables finally are integrated out from Ψ_{sh} in order to remove any explicit dependence on them.

2. Diffusion Monte Carlo method

Despite the fact that variational methods may provide qualitatively correct results, it is not possible to determine their accuracy in absolute terms. The Green's function Monte Carlo method eliminates any variational constraint by directly solving the Schrödinger equation for an N-body problem. The most advanced form of this method is domain GFMC, in which the corresponding Green's function is time independent (Kalos, 1962; Kalos, Levesque, and Verlet, 1974; Ceperley, Chester, and Kalos, 1976; Whitlock and Kalos, 1979; Whitlock *et al.*, 1979; Schmidt and Kalos, 1984). A related method is the diffusion Monte Carlo method, which is time dependent and nowadays widely used (Ceperley and Alder, 1980; Reynolds *et al.*, 1982; Hammond, Lester, and Reynolds, 1994; Anderson, 2002).

The DMC method is a projector method that, by working in imaginary time, is able to retrieve exact energy results for the ground state of a many-particle system. In imaginary time τ the Schrödinger equation becomes

$$-\frac{\partial \Psi(\boldsymbol{R}, \tau)}{\partial \tau} = (\hat{H} - E_0) \Psi(\boldsymbol{R}, \tau), \tag{21}$$

where $\boldsymbol{R} = \{\boldsymbol{r}_1, \ldots, \boldsymbol{r}_N\}$ and time is expressed in units of $\hbar$. The time-dependent wave function of the system $\Psi(\boldsymbol{R}, \tau)$ can be expanded in terms of the complete set of eigenfunctions of the Hamiltonian $\phi_i(\boldsymbol{R})$, namely,

$$\Psi(\boldsymbol{R}, \tau) = \sum_n c_n \exp\left[-(E_i - E_0)\tau\right] \phi_i(\mathbf{R}), \tag{22}$$

where E_i is the eigenvalue associated with $\phi_i(\boldsymbol{R})$. The asymptotic solution of Eq. (21) in the $\tau \to \infty$ limit then

corresponds to $\phi_0(\boldsymbol{R})$, provided that there is a nonzero overlap between $\Psi(\boldsymbol{R},\tau=0)$ and the true ground-state wave function $\phi_0(\boldsymbol{R})$.

Direct application of Eq. (21) to condensed matter problems is hindered by the repulsive interactions that atoms experience at short distances, which translates into large energy variances. To overcome this problem, one introduces importance sampling, a technique that is widely used in the Monte Carlo (MC) calculation of integrals. Importance sampling as applied to Eq. (21) consists of rewriting the Schrödinger equation in terms of the pdf:

$$f(\boldsymbol{R},\tau) \equiv \psi(\boldsymbol{R})\Psi(\boldsymbol{R},\tau), \tag{23}$$

where $\psi(\boldsymbol{R})$ is a time-independent trial wave function that at the variational level correctly describes the ground state of the crystal. By considering a Hamiltonian of the form

$$\hat{H} = -\frac{\hbar^2}{2m}\nabla_{\boldsymbol{R}}^2 + \hat{V}(\boldsymbol{R}), \tag{24}$$

Eq. (21) turns into

$$-\frac{\partial f(\boldsymbol{R},t)}{\partial\tau} = -D\nabla^2 f(\boldsymbol{R},\tau) + D\nabla[\boldsymbol{F}(\boldsymbol{R})f(\boldsymbol{R},\tau)] + [E_{\mathrm{L}}(\boldsymbol{R}) - E_0]\cdot f(\boldsymbol{R},\tau), \tag{25}$$

where $D \equiv \hbar^2/(2m)$, $E_{\mathrm{L}}(\mathbf{R}) \equiv \psi(\boldsymbol{R})^{-1}H\psi(\boldsymbol{R})$ is the local energy, and

$$\boldsymbol{F}(\boldsymbol{R}) \equiv 2\psi(\boldsymbol{R})^{-1}\nabla\psi(\boldsymbol{R}) \tag{26}$$

is the so-called drift or quantum force. $\boldsymbol{F}(\boldsymbol{R})$ acts as an external force that guides the diffusion process rendered by the first term on the right-hand side of Eq. (25). In particular, walkers are attracted toward regions in which the value of $\psi(\boldsymbol{R})$ is large, thus avoiding the repulsive core of the interaction that produces large fluctuations in the energy.

The right-hand side of Eq. (25) can be written as the action of three operators $\hat{A}_i$ acting on the pdf $f(\boldsymbol{R},\tau)$, namely,

$$-\frac{\partial f(\boldsymbol{R},\tau)}{\partial\tau} = (\hat{A}_1+\hat{A}_2+\hat{A}_3)f(\boldsymbol{R},\tau) \equiv \hat{A}f(\boldsymbol{R},\tau). \tag{27}$$

The operator $\hat{A}_1$ corresponds to a free diffusion process with coefficient D, $\hat{A}_2$ to a driving force produced by an external potential, and $\hat{A}_3$ to a birth and death branching term. In the quantum Monte Carlo method, the Schrödinger equation is most manageable when expressed in an integral form. This is achieved by introducing a Green's function $G(\boldsymbol{R}',\boldsymbol{R},\tau)$ that describes the transition probability to move from an initial state $\boldsymbol{R}$ to a final state $\boldsymbol{R}'$ during the time interval $\Delta\tau$; that is,

$$f(\boldsymbol{R}',\tau+\Delta\tau) = \int G(\boldsymbol{R}',\boldsymbol{R},\Delta\tau)f(\boldsymbol{R},\tau)d\boldsymbol{R}. \tag{28}$$

More explicitly, the Green's function can be expressed in terms of the $\hat{A}$ operator as

$$G(\boldsymbol{R}',\boldsymbol{R},\Delta\tau) = \langle\boldsymbol{R}'|\exp(-\Delta\tau\hat{A})|\boldsymbol{R}\rangle, \tag{29}$$

and can be approximated in practice with Trotter's product formula (Trotter, 1959):

$$e^{-\tau(\hat{A}_1+\hat{A}_2)} = \lim_{n\to\infty}(e^{-(\tau/n)\hat{A}_1}e^{-(\tau/n)\hat{A}_2})^n. \tag{30}$$

DMC algorithms rely on reasonable approximations to the propagator $G(\boldsymbol{R}',\boldsymbol{R},\Delta\tau)$ in the $\Delta\tau\to 0$ limit, which are iterated repeatedly until reaching the asymptotic regime $f(\boldsymbol{R},\tau\to\infty)$ (that is, when the ground state is effectively sampled). The order of the employed $G(\boldsymbol{R}',\boldsymbol{R},\Delta\tau)$ approximation introduces a certain time-step bias on the results that needs to be removed in order to provide perfectly converged solutions (Boronat and Casulleras, 1994). In the DMC method, the sampling of an operator $\hat{O}$ is performed according to the mixed distribution $f(\boldsymbol{R},\tau)$ [see Eq. (23)], rather than to $\phi_0(\boldsymbol{R})$. Consequently, the standard DMC output, the so-called "mixed" estimator, normally is biased by the trial wave function that is used for importance sampling. Only when $\hat{O}$ is the Hamiltonian of the system or an operator that commutes with it, does the mixed estimator and the exact result coincide. A simple scheme that is employed to partially remove the bias introduced by $\psi(\boldsymbol{R})$ is

$$\langle\hat{O}(\boldsymbol{R})\rangle_e = 2\langle\hat{O}(\boldsymbol{R})\rangle_m - \langle\hat{O}(\boldsymbol{R})\rangle_v, \tag{31}$$

which is built from the mixed (m) and variational (v) estimators and is known as the "extrapolated" estimator (e) (Ceperley and Kalos, 1979). Nevertheless, expectation values obtained with the extrapolation approach never are totally free of bias, and it is difficult to estimate *a priori* the size of the accompanying errors. In order to overcome such limitations, one can calculate "pure" expectation values (that is, exact to within the statistical errors) by using the forward walking technique (Casulleras and Boronat, 1995).

3. Path-integral ground-state Monte Carlo method

An interesting alternative to the DMC method was put forward by Sarsa, Schmidt, and Magro (2000), based on a previous proposal by Ceperley (1995). This method is termed the PIGS method and it is directly related to the PIMC method used at finite temperature (see Sec. II.B.1). The integral version of the Schrödinger equation can be written in terms of the Green's function as

$$\Psi(\boldsymbol{R},\tau) = \int d\boldsymbol{R}' G(\boldsymbol{R},\boldsymbol{R}';\tau-\tau_0)\Psi(\boldsymbol{R}',\tau_0). \tag{32}$$

In the PIGS method one exploits the formal identity between the Green's function at imaginary time τ, $G(\boldsymbol{R},\boldsymbol{R}';\tau-\tau_0)$, and the statistical density matrix operator at an inverse temperature $\beta \equiv 1/T$, $\rho(\boldsymbol{R},\boldsymbol{R}';\beta)$. The convolution property of the density matrix permits one to estimate $\rho(\boldsymbol{R},\boldsymbol{R}';\beta)$ through a convolution of density matrices calculated at smaller values β/N_b, namely,

$$\rho(\boldsymbol{R},\boldsymbol{R}';\beta) = \int d\boldsymbol{R}_1 \cdots d\boldsymbol{R}_{N_b-1} \times \rho(\boldsymbol{R},\boldsymbol{R}_1;\beta/N_b)\cdots\rho(\boldsymbol{R}_{N_b-1},\boldsymbol{R}';\beta/N_b). \quad (33)$$

In the PIMC ($T \neq 0$) formalism, one has to deal with the trace of the density matrix operator and hence the boundary condition $\boldsymbol{R} = \boldsymbol{R}'$ is imposed; this makes a *closed path*. In the context of the classical isomorphism (Feynman, 1972; Barker, 1979; Chandler and Wolynes, 1981; Ceperley, 1995), a path is interpreted as a polymer in which first neighbors are connected with springs; moving a quantum particle is equivalent to evolve such a polymer. In the PIGS method ($T = 0$), in contrast to the PIMC method, one truncates the path by imposing that the end points $\boldsymbol{R}'$ terminate in a trial wave function ψ; the path then is *open*. In this case, the expectation value of an operator $\hat{O}$ is determined by

$$\hat{O} = \frac{\langle\psi|G(\tau/2)\hat{O}G(\tau/2)|\psi\rangle}{\langle\psi|G(\tau)|\psi\rangle}, \quad (34)$$

where τ is the total imaginary time that the system takes to move from the initial point to the end. The most remarkable aspect of this method is that in the middle of the path $\tau/2$ the sampling of any operator is exact, independently of whether $\hat{O}$ commutes or not with the Hamiltonian of the system. In other words, calculation of pure estimators is the standard output in the PIGS method, contrary to what occurs in the DMC method (although for operators that commute with the Hamiltonian both methods provide equivalent results). Actually, for nondiagonal operators, such as, for instance, the one-body density matrix, only the PIGS method is able to provide unbiased zero-temperature results in an efficient manner.

In order to perform PIGS calculations as efficiently as possible in practice, it is necessary to develop approximations for the propagator operator that are accurate to within a certain order in the time step. In this regard, significant progress has been achieved in recent years by developing splitting schemes for the exponential of the Hamiltonian operator $\hat{H} = \hat{K} + \hat{V}$ (where $\hat{K}$ and $\hat{V}$ are the kinetic- and potential-energy operators, respectively) of the form:

$$\exp[\varepsilon(\hat{T}+\hat{V})] = \prod_{i=1}^{N} \exp(t_i\varepsilon\hat{T})\exp(v_i\varepsilon\hat{V}), \quad (35)$$

where the values of the parameters $\{t_i\}$ and $\{v_i\}$ are selected in a way that satisfies forward propagation (Chin and Chen, 2002). Under this constraint, one can write algorithms that are accurate up to fourth order (Rota *et al.*, 2010) and which produce consistent convergence toward the ground state (see Sec. II.B.1). Recent applications of the PIGS method involving high-order decomposition methods showed that it is actually possible to obtain results that are completely independent of the trial wave function that is used as a boundary condition (Rossi *et al.*, 2009; Rota *et al.*, 2010). Even in the limiting case of considering only the symmetry requirement of the system [e.g., $\psi(\boldsymbol{R}) = 1$ in the bosonic case] the PIGS method works reliably, with the only penalty of producing slightly larger variances. These methodological advancements permit one to achieve accurate zero-temperature results in systems for which it is difficult to find a good trial wave function.

A related method to the PIGS method is the reptation quantum Monte Carlo (RQMC) method due to Baroni and Moroni (1999); the starting point in the RQMC method is the same as that in the PIGS method, that is, Eq. (32). The main difference relies on the approximation that is used in the Green's function: the RQMC method adopts a short-time expression similar to the one used in the DMC method [see Eq. (29)] consisting of a drifted Gaussian that incorporates importance sampling. The ways in which the paths are sampled are also different in the two methods. In the case of knowing a good trial wave function, the RQMC method may be advantageous as the resulting energy variance can be reduced significantly; otherwise, for the reasons explained, the PIGS method may turn out to be a more reliable method (Rossi *et al.*, 2009; Rota *et al.*, 2010).

B. Finite-temperature techniques

1. Path-integral Monte Carlo method

The PIMC method is based on the convolution property of the thermal density matrix shown in Eq. (33). This allows one to estimate the density matrix at low temperature from its knowledge at higher temperatures, the latter being described by classical statistical mechanics. The partition function Z of a quantum system then becomes a multidimensional integral with a distribution law that resembles that of a closed classical polymer with an interbead harmonic coupling. If one assumes that all particles are bosons, the corresponding quantum statistical distribution is then positively defined and can be interpreted as a probability distribution function that can be sampled with standard Metropolis MC techniques. The finite-T mapping of a quantum system into a classical one composed of polymers was first proposed by Feynman (1972) and subsequently applied by Barker (1979) and Chandler and Wolynes (1981) to condensed matter simulations.

The quantum partition function of a general Hamiltonian $\hat{H}$ at temperature T is

$$Z = \mathrm{Tr}e^{-\beta\hat{H}}. \quad (36)$$

The noncommutativity of operators $\hat{K}$ and $\hat{V}$ makes a direct calculation of Z impractical in the quantum regime. Nevertheless, one can exploit the following convolution property:

$$e^{-\beta(\hat{K}+\hat{V})} = (e^{-\varepsilon(\hat{K}+\hat{V})})^M, \quad (37)$$

where $\varepsilon = \beta/M$, since now each of the terms on the right-hand side of the equality effectively corresponds to a higher temperature, that is, $T' = M \cdot T$. In the lowest order approximation, known as the primitive action, the kinetic and potential contributions are factorized as

$$e^{-\varepsilon(\hat{K}+\hat{V})} \simeq e^{-\varepsilon\hat{K}}e^{-\varepsilon\hat{V}}, \quad (38)$$

and the convergence to the exact result is guaranteed by the Trotter's product formula (Trotter, 1959):

$$e^{-\beta(\hat{K}+\hat{V})} = \lim_{M\to\infty}(e^{-\varepsilon\hat{K}}e^{-\varepsilon\hat{V}})^M. \tag{39}$$

The primitive action approximation, however, is not accurate enough to reach proper convergence at very low temperatures, when the number of terms involved, also called "beads," is large. In recent years, there has been relevant progress in achieving better convergence by using high-order splitting schemes of the exponential operator. Fourth-order algorithms can be developed by introducing double commutators (Chin and Chen, 2002; Sakkos, Casulleras, and Boronat, 2009) of the form

$$[[\hat{V},\hat{K}],\hat{V}] = \frac{\hbar^2}{m}\sum_{i=1}^{N}|\boldsymbol{F}_i|^2, \tag{40}$$

where $\boldsymbol{F}_i$ is the "force" acting on particle i, namely,

$$\boldsymbol{F}_i = \sum_{j\neq i}^{N}\boldsymbol{\nabla}_i V(r_{ij}). \tag{41}$$

One of the most efficient splitting schemes corresponds to

$$e^{-\varepsilon\hat{H}} \simeq e^{-v_1\varepsilon\hat{W}_{a_1}}e^{-t_1\varepsilon\hat{K}}e^{-v_2\varepsilon\hat{W}_{1-2a_1}} \times e^{-t_1\varepsilon\hat{K}}e^{-v_1\varepsilon\hat{W}_{a_1}}e^{-2t_0\varepsilon\hat{K}}, \tag{42}$$

where $W(r)$ is a generalized potential that includes the double commutator in Eq. (40) [see Sakkos, Casulleras, and Boronat (2009) for details on the definition of the different factors appearing in Eq. (42)]. We note that by optimizing the value of the parameters in this expansion, convergence with nearly sixth-order accuracy in ε can be achieved.

From the knowledge of the quantum partition function one can access the total and kinetic energies by using the well-known thermodynamic relations

$$E = \langle\hat{H}\rangle = -\frac{1}{Z}\frac{\partial Z}{\partial\beta}, \tag{43}$$

$$E_{\mathrm{k}} = \langle\hat{K}\rangle = \frac{m}{\beta Z}\frac{\partial Z}{\partial m}, \tag{44}$$

where the potential energy comes from the difference $E_{\mathrm{p}} = E - E_{\mathrm{k}}$. The potential energy also can be computed through

$$\hat{O}(\boldsymbol{R}) = -\frac{1}{\beta}\frac{1}{Z(\hat{V})}\frac{dZ(\hat{V}+\lambda\hat{O})}{d\lambda}\bigg|_{\lambda=0}, \tag{45}$$

which in general is suitable for estimating operators that depend only on particle coordinates. We note that the kinetic-energy expression in Eq. (44), which is known as the "thermodynamic" estimator, presents some technical drawbacks such as a diverging variance when the number of beads is large. Several solutions have been proposed to overcome this limitation, among which we highlight the "virial" estimator introduced by Cao and Berne (1989).

An alternative to the discussed decomposition scheme of the exponential operator is to use a pair product approximation (Ceperley, 1995). In this case, one approximates the density matrix by a factorization of correlations up to second order, resembling the Jastrow approximation used for the ground state, namely,

$$\rho(\boldsymbol{R},\boldsymbol{R}';\varepsilon) = \prod_{i=1}^{N}\rho_1(\boldsymbol{r}_j,\boldsymbol{r}_j';\varepsilon)\prod_{i<j}^{N}\hat{\rho}_2(\boldsymbol{r}_{ij},\boldsymbol{r}_{ij}';\varepsilon). \tag{46}$$

In Eq. (46), ρ_1 represents the density matrix for a noninteracting system and $\hat{\rho}_2$ the normalized pair density matrix, that is,

$$\hat{\rho}_2(\boldsymbol{r}_{ij},\boldsymbol{r}_{ij}';\varepsilon) = \frac{\rho_2(\boldsymbol{r}_{ij},\boldsymbol{r}_{ij}';\varepsilon)}{\rho_2^0(\boldsymbol{r}_{ij},\boldsymbol{r}_{ij}';\varepsilon)}, \tag{47}$$

in which ρ_2 and ρ_2^0 are the relative density matrices of the interacting and noninteracting systems, respectively. The pair action is especially useful when the pair density matrix is known analytically or an accurate approximation of it is at hand. Application of this approach is particularly suitable for the study of central potentials, although it is not restricted to this type of interaction (Pierleoni and Ceperley, 2006).

The formalism explained previously applies only to distinguishable particles (i.e., "boltzmanons"), since the symmetry requirement under the exchange of particles has been neglected systematically. In order to correctly describe quantum Bose crystals one needs to symmetrize the corresponding thermal density matrix, namely,

$$\rho_s(\boldsymbol{R},\boldsymbol{R}';\varepsilon) = \frac{1}{N!}\sum_{\mathcal{P}}\rho(\boldsymbol{R},\mathcal{P}\boldsymbol{R}';\varepsilon), \tag{48}$$

where the summation runs over all possible $N!$ permutations involving the system particles. In contrast to the boltzmanon case, in which the number of closed polymers equals the number of particles ($\boldsymbol{R}_{M+1} = \boldsymbol{R}_1$, with M the number of beads), the new boundary condition $\boldsymbol{R}_{M+1} = \mathcal{P}\boldsymbol{R}_1$ implies that each closed polymer can represent more than one particle. The acceptance rate for the proposed permutations then increases with the inverse of the temperature; when the thermal wavelength λ_T is comparable to the mean interparticle distance the size of closed polymers becomes macroscopic, originating Bose-Einstein condensation and superfluidity (see Sec. I.C).

The fraction of particles occupying the lowest momentum state in a bosonic system, i.e., the condensate fraction $n_0 \equiv n(k=0)$, can be obtained from the long-range behavior of the one-body density matrix, defined as

$$\varrho_1(r_{11'}) = \frac{V}{Z}\int d\boldsymbol{r}_2\cdots d\boldsymbol{r}_N\rho_s(\boldsymbol{R},\boldsymbol{R}';\beta), \tag{49}$$

namely, $n_0 = \lim_{r\to\infty}\varrho_1(r)$. In practice, $\varrho_1(r)$ is estimated by calculating frequency histograms over distances between $\boldsymbol{r}_1$ and $\boldsymbol{r}_1'$.

Sampling the space of permutations is technically involved because one has to guarantee ergodicity. In recent years, the introduction of the worm algorithm has significantly improved the efficiency in this type of calculation (Boninsegni, Prokof'ev, and Svistunov, 2006a). The idea behind the worm

algorithm is to work in an extended configuration space with two sectors. In the diagonal sector, termed Z, all paths are closed, which corresponds to conventional PIMC simulations. In the second sector, termed Z_G, all paths are closed except one, which is called the worm; this latter sector, therefore, is nondiagonal. The generalized partition function then can be written as

$$Z_W = Z + CZ_G, \tag{50}$$

where $C > 0$ is a dimensionless parameter that is fixed during the simulation. The parameter C controls the relative statistics between sectors Z and Z_G. In the nondiagonal sector one proposes swap movements that generate multiparticle permutations (i.e., by single pair permutations between the worm and closed paths), whereas in the diagonal sector particles evolve as boltzmanons.

2. Path-integral molecular dynamics

In the PIMD formalism, the partition function of a quantum system is approximated with the following Maxwell-Boltzmann expression:

$$Z \approx \frac{1}{N!}\left(\frac{mL}{2\pi\beta\hbar^2}\right)^{3NL/2} \times \int \prod_{j=1}^{N}\prod_{i=1}^{L} d\mathbf{r}_{ij} e^{-\beta(E_k+E_p)}. \tag{51}$$

Equation (51) completely disregards possible quantum atomic exchanges stemming from the indistinguishability of the atoms (in contrast to the PIGS and PIMC methods, see Secs. II.A.3 and II.B.1); that is, particles are treated as boltzmanons. Nevertheless, in the case of quantum crystals it is well known that the role of quantum statistics is secondary at moderate and high temperatures (e.g., $T > 100$ K in hydrogen at $P \sim 100$ GPa) (McMahon *et al.*, 2012). In those situations, the PIMD formalism can be used to compute, for instance, quantum time-correlation functions and transition state rates in an efficient manner (Gillan, 1990; Habershon *et al.*, 2013; Herrero and Ramírez, 2014).

The key idea behind the PIMD formalism is to formulate a Hamiltonian framework in which new space coordinates and momenta $(\mathbf{u}_{ij}, \mathbf{p}_{ij})$ are introduced for sampling the integral in Eq. (51) with molecular dynamics techniques. In particular, the new space coordinates and momenta are referred to the staging modes $\mathbf{u}_{ij}$ that diagonalize the harmonic energy term, namely,

$$E_k = \frac{mL}{2\beta^2\hbar^2}\sum_{j=1}^{N}\sum_{i=1}^{L}(\mathbf{r}_{ij} - \mathbf{r}_{(i+1)j})^2 = \sum_{j=1}^{N}\sum_{i=2}^{L}\frac{m_i L}{2\beta^2\hbar^2}\mathbf{u}_{ij}^2. \tag{52}$$

For a given atom j, the staging mode coordinates are defined as $\mathbf{u}_{1j} = \mathbf{r}_{1j}$, and

$$\mathbf{u}_{ij} = \mathbf{r}_{ij} - \frac{i-1}{i}\mathbf{r}_{(i+1)j} - \frac{1}{i}\mathbf{r}_{1j}$$

in the rest of the cases; the corresponding staging mode masses are $m_1 = 0$, and $m_i = (i/i-1)m$ in the rest of the cases.

The momentum variables that are required for the molecular dynamics algorithm to work are introduced through the substitution of the prefactor in the partition function by a Gaussian integral of the form

$$\left(\frac{mL}{2\pi\beta\hbar^2}\right)^{3NL/2} = C\int \prod_{j=1}^{N}\prod_{i=1}^{L} d\mathbf{p}_{ij} e^{-\beta\mathbf{p}_{ij}^2/2\chi_i}, \tag{53}$$

where C is a constant that depends on the staging momentum masses, but which has no influence on the calculation of the equilibrium properties; $\mathbf{p}_{ij}$ is the i staging momentum of particle j. The masses χ_i in Eq. (53) can be defined as $\chi_1 = m$, and $\chi_i = m_i$ in the rest of the cases; essentially, these must be chosen so that all $i > 1$ staging modes evolve in the same time scale.

In either (N, V, T) or (N, P, T) PIMD simulations, control of the temperature is achieved through a massive thermostatting of the system that implies a chain of Nosé-Hoover thermostats coupled to each staging variable $\mathbf{u}_{ij}$ (Tuckerman and Hughes, 1998). The involved thermostats introduce friction terms in the corresponding dynamic equations and thus the dynamics of the quantum system is no longer Hamiltonian. Nevertheless, it is always possible to define a quantity with units of energy that is well conserved during the simulation and that can be used to check whether integration of the equations of motion is being done correctly (Martyna, Hughes, and Tuckerman, 1999). Finally, we note that equivalent estimators in the PIMD and PIMC frameworks may present some formal differences although only in the terms involving momentum variables. Nevertheless, in those cases in which quantum atomic exchanges can be safely neglected, both PIMD and PIMC approaches should provide identical expectation values, as it follows from the equipartition theorem (Herrero and Ramírez, 2014).

A detailed account of the PIMD method certainly is out of the scope of this review. The details of this technique have been thoroughly described by Tuckerman and Hughes (1998) and Martyna, Hughes, and Tuckerman (1999); hence we refer the interested reader to those works.

3. Quantum thermal baths

The key idea behind QTB is to use a Langevin-type approach in which a dissipative force and a Gaussian random force are adjusted to have the power spectral density given by the quantum fluctuation-dissipation theorem (Ceriotti, Bussi, and Parrinello, 2009; Dammak *et al.*, 2009; Barrat and Rodney, 2011). In doing this, the internal energy of the system can be mapped into that of an ensemble of harmonic oscillators whose vibrational modes follow a Bose-Einstein distribution. It is worth noticing that while such a quantum discretization is applied to the energy, the atoms in the system are invariably treated as distinguishable particles. Consequently, QTB are not well suited for describing physical phenomena in which

TABLE I. A list of computer simulation packages that allow one to simulate quantum nuclear effects in periodic systems. PIMD, PIMC, VMC, DMC, and PIGS in the "capabilities" column stand for, path-integral molecular dynamics, path-integral Monte Carlo, variational Monte Carlo, diffusion Monte Carlo, and ground-state path-integral Monte Carlo methods, respectively. CPU and GPU in the "parallelization" column stand for central and graphical processing units.

Package	Capabilities	Parallelization	License	Reference
ABINIT	PIMD	CPU	Free	Gonze *et al.* (2016)
CASINO	VMC/DMC	CPU	Free	Needs *et al.* (2010)
CHAMP	VMC/DMC	CPU	Free	Umrigar *et al.* (2007)
CP2K	PIMD	CPU	Free	Hutter *et al.* (2014)
CPMD	PIMD	CPU	Free	Marx, Tuckerman, and Martyna (1999)
i − PI	PIMD	CPU	Free	Ceriotti, More, and Manolopoulos (2014)
OPENMM	PIMD	CPU/GPU	Free	Ceriotti, Parrinello *et al.* (2010)
PIMC ++	PIMC	CPU	Free	Clark and Ceperley (2008)
pi − QMC	PIMD	CPU	Free	Shumway (2005)
QL	VMC	GPU	Free	Lutsyshyn (2015)
QMCPACK	VMC/DMC	CPU/GPU	Free	Esler *et al.* (2012) and Kim *et al.* (2012)
QSATS	PIGS	CPU	Free	Hinde (2011)
QWALK	VMC/DMC	CPU	Free	Wagner, Bajdich, and Mitas (2009)

quantum atomic exchanges are important, which typically occur in disordered and *incommensurate* systems at low temperatures (in contrast to the PIGS and PIMC methods, see Secs. II.A.3 and II.B.1).

In analogy to the classical Langevin thermostat method, each particle is coupled to a fictitious bath by introducing a random force and a dissipation term in the equations of motion of the form

$$m\frac{d^2\mathbf{r}}{dt^2} = \mathbf{F}(\mathbf{r}) - \gamma m\frac{d\mathbf{r}}{dt} + \sqrt{2m\gamma}\Theta(t), \tag{54}$$

where $\mathbf{r}$ and $\mathbf{F}$ represent the atomic positions and total forces exerted by the rest of the particles, respectively. The function $\Theta(t)$ is a colored noise with a power spectral density that follows the Bose-Einstein distribution, namely,

$$\begin{aligned}\tilde{\Theta}(\omega) &= \int e^{-i\omega t}\langle\Theta(t)\Theta(t')\rangle dt \\ &= \hbar\omega\left(\frac{1}{2} + \frac{1}{e^{\hbar\omega/k_B T} - 1}\right),\end{aligned} \tag{55}$$

which takes into account the zero-point energy of the system as given by the quasiharmonic approximation (see Sec. II.A.1).

In practice, $\tilde{\Theta}(\omega)$ can be generated by using a signal-processing method based on the filtering of white noise (Barrat and Rodney, 2011). The implementation of QTB in a discrete MD algorithm then is quite straightforward. QTB neither slow down the calculations appreciably nor are detrimental in terms of memory requirements. For these reasons, the use of QTB for simulation of QNE is becoming increasingly more popular in recent years (Hernández-Rojas, Calvo, and González-Noya, 2015).

A word of caution, however, must be added here. QTB alone fail to reproduce the correct quantum behavior in highly anharmonic systems and processes (Ceriotti, Bussi, and Parrinello, 2009; Barrozo and de Koning, 2011; Bedoya-Martínez, Barrat, and Rodney, 2014). Consequently, the conclusions attained with QTB-based methods should always be validated against results obtained with more accomplished quantum approaches (e.g., PIMC and PIMD). Meanwhile, it was recently demonstrated that QTB can be used to noticeably accelerate the convergence in PIMD calculations (Ceriotti, Manolopoulos, and Parrinello, 2011; Ceriotti and Manolopoulos, 2012; Brieuc, Dammak, and Hayoun, 2016). In particular, generalized Langevin thermostats allow one to sample the canonical distribution more efficiently by reducing the usual ergodic problems encountered in path-integral simulations performed with a large number of beads. It is probably in this latter context that QTB techniques may become particularly useful.

C. Computer packages

While the number of classical simulation packages, either commercially or freely available, is practically countless, the number of computer packages that allow one to simulate QNE is very limited. In Table I, we list those computer packages that, to the best of our knowledge, are publicly available and can be used to simulate QNE in periodic systems, along with a brief description of their basic capabilities. In total, they amount to a bit more than ten.

We note that PIMD (see Sec. II.B.2) is the method that is implemented most frequently. On the other hand, quantum Monte Carlo techniques (i.e., VMC and DMC methods) are available only in a few codes. Although it is not indicated in Table I, most of the listed simulation packages also allow one to describe the interactions between atoms through *ab initio* methods (see Sec. III.A). In addition to this, they are all designed to run in high-performance computing architectures and can be downloaded free of charge from the Internet or made available on request.

A likely reason behind the scarcity of studies considering QNE may be, apart from the increased computational and technical burdens as compared to classical calculations, the limited number of available quantum simulation packages. We note that most of the codes in Table I are relatively new; hence until recently any researcher interested in simulating QNE had

to craft his or her own quantum implementation. Nevertheless, we expect that due to the steady growth in computing power and the increasing awareness of the importance of QNE in condensed matter systems and materials, the availability and user friendliness of quantum simulation packages will increase over the next years.

III. MODELING OF ATOMIC INTERACTIONS

The simulation techniques that are used to describe the atomic interactions in quantum crystals, and materials in general, can be classified into two major categories: semiempirical and first principles. In semiempirical approaches, the interparticle forces are typically modeled with analytical functions, known as force fields or classical potentials, that are devised to reproduce a particular set of experimental data or the results of highly accurate calculations. The inherent simplicity of classical potentials makes it possible to address the study of quantum solids within ample thermodynamic intervals and large length and time scales, with well-established quantum simulation techniques such as the ones discussed in Sec. II. By using semiempirical potentials and exploiting the current computational power and algorithm development, quantum simulations of condensed matter systems can be routinely performed nowadays in multicore processors. Nevertheless, in spite of their great versatility, classical potentials may sometimes present some impeding transferability issues. Transferability issues are related to the impossibility of mimicking the targeted systems at conditions different from those in which the setup of the corresponding force field was performed. An illustrative example of such a failure is given by the unreliable description of highly compressed rare-gas crystals with pairwise potentials (Cazorla and Boronat, 2008a, 2015a, 2015b). In addition to this, there are many physical phenomena that simply cannot be reproduced accurately with straightforward force fields (e.g., magnetic spin interactions, electronic screening effects, and oxidation-state changes, to cite just a few examples).

In this context, the output of first-principles calculations, also known as *ab initio*, turns out to be crucial. In first-principles approaches, as the name indicates, no empirical information is assumed on the derivation of the atomic interactions: these are directly obtained from applying the principles of quantum mechanics to the electrons and nuclei. Transferability issues, therefore, are absent. First-principles approaches are in general very accurate, but they can also be very demanding in terms of computational expense. This circumstance makes the full *ab initio* study of quantum crystals, that is, in which both the electronic and nuclear degrees of freedom are treated quantum mechanically, intricate and computationally very demanding (Pierleoni, Ceperley, and Holzmann, 2004; Pierleoni and Ceperley, 2005, 2006; McMahon *et al.*, 2012). Common acceleration schemes within first-principles schemes involve the use of pseudopotentials (Vanderbilt, 1990; Troullier and Martins, 1991), which avoids explicitly treating the core electrons. This approximation is based on the fact that many material properties can be predicted by focusing exclusively on the behavior of valence electrons. Nonetheless, pseudopotentials can actually be the source of potential errors. Fortunately, some strategies can be used to minimize the impact of the approximations introduced by pseudopotentials such as, for instance, the projector augmented wave method (Blöchl, 1994) and linearized augmented plane waves (Andersen, 1975). Next, we concisely explain some basic aspects of first-principles and semiempirical methods as related to the study of quantum solids.

A. First-principles methods

In solids, the dynamics of electrons and nuclei can be decoupled to a good approximation because their respective masses differ by several orders of magnitude. The wave function of the corresponding many-electron system $\Psi(\mathbf{r}_1, \mathbf{r}_2, \ldots, \mathbf{r}_N)$ therefore can be determined by solving the Schrödinger equation involving the following nonrelativistic Born-Oppenheimer Hamiltonian:

$$H = -\frac{1}{2}\sum_i \nabla_i^2 - \sum_I \sum_i \frac{Z_I}{|\mathbf{R}_I - \mathbf{r}_i|} + \frac{1}{2}\sum_i \sum_{j\neq i} \frac{1}{|\mathbf{r}_i - \mathbf{r}_j|}, \tag{56}$$

where Z_I are the nuclear charges, $\mathbf{r}_i$ are the positions of the electrons, and $\mathbf{R}_I$ are the positions of the nuclei, which are considered fixed. Note that nonadiabatic effects beyond the Born-Oppenheimer approximation in principle can also be treated within first-principles methods by using wave functions that explicitly depend on the electronic and nuclear degrees of freedom (Ceperley and Alder, 1987; Tubman *et al.*, 2014; Yang *et al.*, 2015). In real materials Ψ is a complex mathematical function that in most cases is unknown. Electrons are fermion particles, hence their wave function must change sign when two of them exchange orbital states. This quantum antisymmetry leads to an effective repulsion between electrons, called the Pauli repulsion, that helps in lowering their total Coulomb energy. At the heart of any first-principles method is to find a good approximation to Ψ, or an equivalent solution, that is manageable enough to perform calculations and simultaneously correctly describes the system of interest. Examples of *ab initio* methods include density functional theory, Møller-Plesset perturbation theory (MP2), the coupled-cluster method with single, double, and perturbative triple excitations [CCSD(T)], and the electronic quantum Monte Carlo method, to cite just a few. From these, DFT and the eQMC method have been most intensively applied to the study of quantum solids and for this reason we summarize their foundations in what follows.

1. Density functional theory

In 1965, Kohn and Sham developed a pioneering theory to effectively calculate the energy and properties of many-electron systems without the need of explicitly knowing Ψ (Kohn and Sham, 1965; Sham and Kohn, 1966). The main idea underlying this theory, called density functional theory, is that the exact ground-state energy E and electron density $n(\mathbf{r})$ can be determined by solving an effective one-electron Schrödinger equation of the form

$$H_{\text{eff}}\psi_{i\sigma} = \epsilon_{i\sigma}\psi_{i\sigma}, \tag{57}$$

where i labels different one-electron orbitals and σ the corresponding spin state. In particular,

$$H_{\text{eff}} = -\frac{1}{2}\nabla^2 + V_{\text{ext}}(\mathbf{r}) + \int \frac{n(\mathbf{r}')}{|\mathbf{r}-\mathbf{r}'|}d\mathbf{r}' + V_{xc}(\mathbf{r}), \tag{58}$$

and

$$n(\mathbf{r}) = \sum_{i\sigma}|\psi_{i\sigma}(\mathbf{r})|^2, \tag{59}$$

where V_{ext} represents an external field and $V_{xc}(\mathbf{r}) = \delta E_{xc}/\delta n(\mathbf{r})$ is the exchange-correlation potential.

The exchange-correlation energy has a purely quantum-mechanical origin and can be defined as the interaction energy difference between a quantum many-electron system and its classical counterpart. Despite the fact that E_{xc} represents a relatively small fraction of the total energy, this contribution is extremely crucial for all materials and molecules because it directly acts on the bonding between atoms. In general, $E_{xc}[n]$ is unknown and needs to be approximated. This is the only source of fundamental error in DFT methods. The exact form of the exchange-correlation energy can be readily expressed through the adiabatic connection fluctuation-dissipation theorem as (Langreth and Perdew, 1975; Nguyen and de Gironcoli, 2009)

$$E_{xc}[n] = \int n(\mathbf{r})d\mathbf{r}\int \frac{n_{xc}(\mathbf{r},\mathbf{r}')}{|\mathbf{r}-\mathbf{r}'|}d\mathbf{r}', \tag{60}$$

where $n_{xc}(\mathbf{r},\mathbf{r}') = n_x(\mathbf{r},\mathbf{r}') + n_c(\mathbf{r},\mathbf{r}')$ is the exchange-correlation hole density at position $\mathbf{r}'$ surrounding an electron at position $\mathbf{r}$. Some important constraints on $n_{xc}(\mathbf{r},\mathbf{r}')$ are already known. For instance, $n_x(\mathbf{r},\mathbf{r}')$ must be nonpositive everywhere and its space integral is equal to -1. Also, the space integral of the correlation hole density is zero. These constraints can be employed in the construction of approximate $E_{xc}[n]$ functionals.

In standard DFT approaches $E_{xc}[n]$ is approximated with

$$E_{xc}^{\text{approx}}[n] = \int \epsilon_{xc}^{\text{approx}}(\mathbf{r})n(\mathbf{r})d\mathbf{r}, \tag{61}$$

where $\epsilon_{xc}^{\text{approx}}$ is made to depend on $n(\mathbf{r})$, $\nabla n(\mathbf{r})$, and/or the electronic kinetic energy $\tau(\mathbf{r}) = \frac{1}{2}\sum_{i\sigma}|\nabla\psi_{i\sigma}(\mathbf{r})|^2$.

Next, we summarize the basic aspects of the most popular $E_{xc}[n]$ functionals found in computational studies of condensed matter systems and materials. Additional details on these topics can be found in recent and more specialized reviews (Dobson and Gould, 2012; Klimeš and Michaelides, 2012; Perdew, 2013; Cazorla, 2015). We note that the current number of commercially available and open-source DFT computer packages is large (at least in comparison to that of eQMC codes); a reference to some of them can be found, for instance, in Cazorla (2015).

a. Local and semilocal functionals

In local approaches [e.g., local density approximation (LDA)], E_{xc} is approximated with Eq. (61) and the exchange-correlation energy is taken to be equal to that in a uniform electron gas of density $n(\mathbf{r})$, namely, $\epsilon_{xc}^{\text{unif}}$. The exact $\epsilon_{xc}^{\text{unif}}[n]$ functional is known numerically from quantum Monte Carlo calculations (Ceperley and Alder, 1980; Perdew and Zunger, 1981). In order to deal with the nonuniformity in real electronic systems, the space is partitioned into infinitesimal volume elements that are considered to be locally uniform. In semilocal approaches [e.g., generalized gradient approximation (GGA)], E_{xc} is approximated also with Eq. (61) but $\epsilon_{xc}^{\text{approx}}$ is made to depend on $n(\mathbf{r})$ and its gradient $\nabla n(\mathbf{r})$ (Perdew *et al.*, 1992; Perdew, Burke, and Ernzerhof, 1996). Both local and semilocal approximations satisfy certain exact E_{xc} constraints (e.g., some exact scaling relations and the exchange-correlation hole sum rules) and can work notably well for systems in which the electronic density varies slowly over the space (e.g., bulk crystals at equilibrium conditions). However, by construction local and semilocal functionals cannot account for long-range electronic correlations, otherwise known as dispersion interactions, which certainly are ubiquitous in quantum crystals.

b. Hybrid exchange functionals

Hybrid functionals comprise a combination of nonlocal exact Hartree-Fock (HF) and local exchange energies, together with semilocal correlation energies. The proportion in which both nonlocal and local exchange densities are mixed generally relies on empirical rules. The popular B3LYP approximation (Becke, 1993), for instance, takes 20% of the exact HF exchange energy and the rest from the GGA and LDA functionals. Other well-known hybrid functionals are the HSE proposed by Heyd, Scuseria, and Ernzerhof (2003), PBE0 (Adamo and Barone, 1999), and the family of Minnesota meta hybrid GGA (Zhao, Schultz, and Truhlar, 2005). In contrast to local and semilocal functionals, hybrids can describe to some extent the delocalization of the exchange-correlation hole around an electron. This characteristic is especially useful when dealing with strongly correlated systems containing d and f electronic orbitals (e.g., perovskite oxides). Hybrid functionals, however, do not account for the long-range part of the correlation hole energy and thus cannot reproduce dispersion forces. Effective ways to correct for these drawbacks have been proposed (Chai and Head-Gordon, 2008; Lin *et al.*, 2013; Mardirossian and Head-Gordon, 2014).

c. Dispersion-corrected functionals

DFT-based dispersion schemes reproduce the asymptotic $1/r^6$ interaction between two particles separated by a distance r in a gas. The most straightforward way of achieving this consists of adding an attractive energy term to the exchange-correlation energy of the form $E_{\text{disp}} = -\sum_{i,j}C_{ij}/r_{ij}^6$ (i and j label different particles). This approximation represents the core of a suite of methods named DFT-D that, due to their simplicity and low computational cost, are being widely employed (Grimme, 2004). Nevertheless, DFT-D methods present some inherent limitations. For instance, many-body

dispersion effects and faster decaying terms such as the B_{ij}/r_{ij}^8 and C_{ij}/r_{ij}^{10} interactions are completely disregarded. Also, it is not totally clear from where one should obtain the optimal C_{ij} coefficients. Several improvements on DFT-D methods have been proposed in which the values of the dispersion coefficients are made to depend somehow on the specific atomic environment. Examples of those include the DFT-D3 method by Grimme *et al.* (2010), the vdW(TS) approach by Tkatchenko and Scheffler (2009), and the BJ model by Becke and Johnson (2007). A further degree of elaboration exists in which no external input parameters are needed and the dispersion interactions are directly computed from the electron density. In this context, the exchange-correlation energy is expressed as $E_{xc} = E_x^{\mathrm{GGA}} + E_c^{\mathrm{LDA}} + E_c^{\mathrm{nl}}$, where E_c^{nl} is the nonlocal correlation energy. E_c^{nl} can be calculated as a double space integral involving the electron density and a two-position integration kernel. This approach, introduced by Dion *et al.* (2004), represents a key development in DFT methods as it combines all types of interaction ranges within the same formula. Refinements of this scheme were proposed recently in which the original two-position integration kernel is modified (Vydrov and Voorhis, 2012), or the exchange term in E_{xc} is replaced with other more accurate functionals (Lee *et al.*, 2010; Carrasco *et al.*, 2011).

2. Electronic quantum Monte Carlo method

Here we explain the basics of the diffusion Monte Carlo method (see Sec. II.A.2) as applied to the study of many-electron systems [for a more technical and complete discussion on this topic, see, for instance, Foulkes *et al.* (2001) and Towler (2006)]. In electronic quantum Monte Carlo methods one deals explicitly with the solution to the imaginary time-dependent Schrödinger equation (in contrast to DFT methods). The quantum antisymmetry of the electrons leads to the so-called "sign problem," which is related to the fact that the probability distribution function $f = \Psi_T\Psi_0$ is not positive definite everywhere (see Sec. II.A.2). If the nodes of the guiding and true ground-state wave functions [that is, the $(3N-1)$-dimensional surfaces at which $\Psi(\mathbf{r}_1, \mathbf{r}_2, \ldots, \mathbf{r}_N) = 0$] were coincident, the sign problem would not exist. However, in most many-electron problems this condition is never satisfied. Several approaches have been proposed in the literature to tackle the sign problem, among which we highlight the "fixed-node" (FN) and "released-node" (RN) methods.

a. Fixed-node method

In this method the nodes of the ground-state function Ψ_0 are forced to be equal to those of the guiding wave function Ψ_T [see, e.g., Anderson (1975) and Anderson (1976)]. As a result, the probability distribution function that is asymptotically sampled is always positive because a change of sign in Ψ_T is replicated by a change of sign in Ψ_0. By using this approximation, however, one always obtains results that are upper bounds to the exact ground-state energy (Reynolds *et al.*, 1982). When dealing with fermionic systems, therefore, it is critically important to choose guiding wave functions with high quality nodal surfaces. This requirement is also necessary for guaranteeing numerical stability in the simulations, since the divergence of the drift force $\mathbf{F} = 2\boldsymbol{\nabla}\Psi_T/\Psi_T$ close to a node cannot always be counteracted by the replication of energetically favorable configurations.

The fixed-node electronic DMC (FN-DMC) method was first applied to the electron gas by Ceperley and Alder (1980). Subsequently, it was employed to study solid hydrogen (Ceperley and Alder, 1987) and other crystals containing heavier atoms (Fahy, Wang, and Louie, 1988, 1990; Li, Ceperley, and Martin, 1991). Wigner crystals in two and three dimensions have also been thoroughly investigated with eQMC methods (Tanatar and Ceperley, 1989; Drummond *et al.*, 2004; Drummond and Needs, 2009). Important FN-DMC developments include the introduction of variance minimization techniques to optimize wave functions (Umrigar, Wilson, and Wilkins, 1988) and the use of nonlocal pseudopotentials (Hammond, Reynolds, and Lester, 1987; Hurley and Christiansen, 1987; Fahy, Wang, and Louie, 1988; Mitas, Shirley, and Ceperley, 1991; Trail and Needs, 2013, 2015; Lloyd-Williams, Needs, and Conduit, 2015). We also highlight the generalization of eQMC methods to systems with broken time-reversal symmetry (e.g., interacting electrons in an applied magnetic field or states with nonzero angular momentum), which is known as the "fixed-phase" approximation (Ortiz, Ceperley, and Martin, 1993). These improvements, together with a certain availability of commercial and open-source simulation packages (see Sec. II.C), have stimulated the study of a wide range of electronic systems with the DMC method such as, for instance, strongly correlated oxide materials (Huihuo and Wagner, 2015; Wagner, 2015), hydrates (Alfè *et al.*, 2013; Cox *et al.*, 2014), and organic molecules (Purwanto *et al.*, 2011; Jiang *et al.*, 2012).

b. Released-node method

In the RN method the nodal constraints imposed by the guiding function are relaxed in order to adapt to those of the exact wave function (Ceperley and Alder, 1980, 1984; Hammond, Lester, and Reynolds, 1994; Tubman *et al.*, 2011). As we explain next, this technique provides a solution that is not stable in imaginary time and thus its use is restricted to systems in which (i) the nodes of the guiding function are relatively accurate, or (ii) the Pauli principle is relatively unimportant (that is, the energy difference between the many-fermion system and its many-boson counterpart is small).

An arbitrary antisymmetric wave function Ψ_A can always be expressed as a linear combination of two positive functions such as

$$\Psi_A(\mathbf{r},\tau) = \phi_+(\mathbf{r},\tau) - \phi_-(\mathbf{r},\tau). \tag{62}$$

As both ϕ_+ and ϕ_- are positively defined, each one can be interpreted as a probability density and be propagated individually. A convenient definition of $\phi_\pm$ at $\tau = 0$ is

$$\phi_\pm(\tau = 0) = \tfrac{1}{2}(|\Psi_A| \pm \Psi_A), \tag{63}$$

since at large imaginary time the corresponding projected states are

$$\phi_{\pm}(\tau \to \infty) = \pm C_F \Psi_0^F + C_B \Psi_0^B e^{(E_0^F - E_0^B)\tau}, \tag{64}$$

where Ψ_0^F and Ψ_0^B are the ground-state fermion and boson wave functions of the Hamiltonian, respectively. Ψ_A consistently renders the ground-state energy of the fermionic system, namely,

$$E_0^{RN} = \frac{\int \Psi_A(\tau \to \infty) H \Psi_0 d\mathbf{r}}{\int \Psi_A(\tau \to \infty) \Psi_0 d\mathbf{r}} = E_0^F. \tag{65}$$

However, since the $E_0^F - E_0^B$ energy difference is always positive, the bosonic parts in $\phi_{\pm}$ grow exponentially with imaginary time [see Eq. (64)], leading to an energy variance of

$$\sigma(E_0^{RN}) \propto e^{(E_0^F - E_0^B)\tau} \tag{66}$$

that is divergent. For this reason the RN method is classified as a "transient estimator" approach. In cases where the application of the RN method is judicious, numerical weighting techniques can be used to considerably reduce the variance of the energy and other quantities (Hammond, Lester, and Reynolds, 1994; Tubman *et al.*, 2011). The RN approach can also be employed as a measure of the quality of the upper bounds provided by the fixed-node method (Casulleras and Boronat, 2000; Sola, Casulleras, and Boronat, 2006).

c. Electronic guiding wave functions

In eQMC methods, the choice of the guiding function is particularly important as it determines the degree of accuracy in the calculations. The most widely used Ψ_T model is the Slater-Jastrow wave function that is expressed as

$$\Psi_T(\mathbf{X}) = e^{J(\mathbf{X})} \sum_j c_j D_j(\mathbf{X}), \tag{67}$$

where $\mathbf{X} = (\mathbf{x}_1, \mathbf{x}_2, \ldots, \mathbf{x}_N)$ and $\mathbf{x}_i = \{\mathbf{r}_i, \sigma_i\}$ represent the space and spin coordinates of electron i, e^J is the Jastrow factor, c_j are coefficients, and D_i are Slater determinants of single-particle orbitals of the form

$$D_j(\mathbf{X}) = \begin{vmatrix} \phi_1^j(\mathbf{x}_1) & \phi_1^j(\mathbf{x}_2) & \cdots & \phi_1^j(\mathbf{x}_N) \\ \phi_2^j(\mathbf{x}_1) & \phi_2^j(\mathbf{x}_2) & \cdots & \phi_2^j(\mathbf{x}_N) \\ \vdots & \vdots & \vdots & \\ \phi_N^j(\mathbf{x}_1) & \phi_N^j(\mathbf{x}_2) & \cdots & \phi_N^j(\mathbf{x}_N) \end{vmatrix}. \tag{68}$$

The orbitals $\{\phi_i^j\}$ often are obtained from DFT or Hartree-Fock calculations and are assumed to be products of factors that depend on either the space or spin coordinates. It is common practice in eQMC calculations to replace D_j with products of separate up- and down-spin determinants, since this improves the computational efficiency (Foulkes *et al.*, 2001).

The Jastrow factor in Eq. (67) normally contains one- and two-body terms, namely,

$$J(\mathbf{X}) = \sum_i^N \chi(\mathbf{x}_i) - \frac{1}{2} \sum_i^N \sum_{j \neq i}^N u(\mathbf{x}_i, \mathbf{x}_j), \tag{69}$$

where the functions u describe the electron-electron correlations and χ the electron-nuclear correlations. The two-electron terms in Eq. (69) reduce the value of the wave function whenever two electrons approach each other, hence reducing the repulsive electron-electron interaction energy. However, the introduction of u terms also has the unwanted effect of pushing electrons away from regions of high-charge density into regions of low-charge density, thus depleting the electronic density in the atomic bonds. By introducing the one-body functions χ in the Jastrow factor this problem can be overcome.

Another approach that is employed to improve the description of electron-electron correlations consists of considering backflow correlations within the Slater determinants. Backflow correlations were originally derived from a current conservation argument due to Feynman (1956) to provide a picture of excitations in liquid ^{4}He; they represent the characteristic flow pattern in a quantum fluid where particles in front of a moving one go on filling the space left behind it. The introduction of backflow correlations may relax in practice the constraints associated with the fixed-node approximation. For instance, it has been demonstrated that the use of backflow wave functions in homogeneous electron systems significantly reduces the corresponding VMC and DMC energies (Kwon, Ceperley, and Martin, 1993, 1998; López-Ríos *et al.*, 2006).

3. DFT versus eQMC method

In the last decade, important methodological progress has been made in the context of DFT calculations that allow one now to describe the electronic features of many materials adequately. Examples of these advancements are explained in Sec. III.A.1 and essentially are related to the construction of accurate and computationally efficient hybrid exchange and dispersion-corrected functionals. A pending challenge in DFT methods, however, is posed by the difficulties encountered in the reproduction of many-body and Coulomb screening effects. This type of shortcoming stems from the pairwise additivity that is assumed in the construction of most DFT functionals. Essentially, the interaction energy between two atoms completely neglects the effects introduced by the medium that separates them (Misquitta *et al.*, 2010; Tkatchenko, Alfè, and Kim, 2012; Gobre and Tkatchenko, 2013). In this context, the adiabatic connection fluctuation-dissipation theorem has been exploited to calculate correlation DFT energies that incorporate many-body terms beyond pairwise. This is the case of the random phase approximation to DFT (Dobson, White, and Rubio, 2006) and DFT + MBD methods (Ruiz *et al.*, 2012; Tkatchenko *et al.*, 2012; Ambrosetti *et al.*, 2014), which at the moment are receiving the highest attention. In the latest DFT + MBD versions, for instance, the Schrödinger equation of a set of fluctuating and interacting quantum harmonic oscillators is directly solved within the dipole approximation, and the resulting many-body energy is coupled to an approximate semilocal DFT functional

(Tkatchenko *et al.*, 2012; Ambrosetti *et al.*, 2014). Many-body DFT-based methods, however, are still in their infancy and the associated computational expenses are elevated, hence their applicability yet is limited.

The eQMC method, on the other hand, is inherently exact as it accounts for any type of electronic correlation, exchange, or many-body screening effect (although it is affected by the sign problem explained in previous sections). A further advantage of using the eQMC method is that it is possible to treat the zero-point motion of the nuclei beyond the Born-Oppenheimer approximation, that is, considering nonadiabatic effects (Ceperley and Alder, 1987; Tubman *et al.*, 2014; Yang *et al.*, 2015). This can be done by using wave functions that explicitly depend on both the electronic and nuclear degrees of freedom in projector MC schemes (e.g., DMC and GFMC methods). Another interesting feature of the eQMC method, in contraposition to DFT methods, is that in the case of light atoms the use of pseudopotentials can be avoided. This aspect is especially desirable for the study of quantum solids such as H_2 and ^{4}He, since core electrons then can be simulated without assuming any constraint (Morales, Pierleoni, and Ceperley, 2010; Morales *et al.*, 2013).

On the down side, the eQMC method presents some technical difficulties that are absent in DFT calculations. For instance, the periodic Ewald sum that is used to estimate the electron-electron interactions introduces a finite-size error in the exchange-correlation energy, as it depends on the size and shape of the simulation cell (Foulkes *et al.*, 2001). Consequently, the use of either increasingly large simulation cells or effective correction schemes (Fraser *et al.*, 1996; Hood *et al.*, 1997; Chiesa *et al.*, 2006) is necessary to guarantee proper convergence. For a detailed description of finite-size error treatment in the eQMC method see the recent and specialized articles by Drummond *et al.* (2008), Ma, Zhang, and Krakauer (2011), and Holzmann *et al.* (2016). Another intricacy is found in the calculation of the atomic forces. Calculating forces using a stochastic algorithm turns out to be difficult because straightforward derivation of the total energy with respect to the atomic positions, as it follows from the Hellmann-Feynman principle, leads to estimators with very large variances. Correlated sampling techniques have been proposed to make the statistical errors in the relative energy of different geometries much smaller than the errors in the separate energies (Filippi and Umrigar, 2000). Finite difference methods, however, become already impractical when considering systems containing a few tens of atoms. Alternative approaches based on "zero-variance" Hellmann-Feynman estimators (Assaraf and Caffarel, 2000; Chiesa, Ceperley, and Zhang, 2005; Per, Russo, and Snook, 2008; Clay *et al.*, 2016) and sampling of pure probability distributions (Badinski *et al.*, 2010) have been introduced more recently. Nevertheless, the central problem of efficiently calculating accurate forces in extended systems still persists.

The great accuracy of eQMC methods does not come free of cost. Although the scaling with respect to the number of electrons is the same as in DFT methods, namely, N^3 in standard cases, the prefactors in the eQMC method are considerably larger (e.g., roughly 10 and 100 times larger in VMC and DMC methods, respectively) (Foulkes *et al.*, 2001; Towler, 2006). Also, the convergence of the total energy is achieved more slowly than in DFT due to the usual MC propagation and sampling procedures. In spite of this, thanks to the escalating increase in computing efficiency and recent algorithmic advances, the use of the eQMC method is transitioning from that of benchmark calculations in few-atom systems to that of production runs in hundreds-of-atoms systems (Esler *et al.*, 2012; Kim *et al.*, 2012; Wagner, 2014). Actually, efficient QMC-based methods have already been developed that allow one to simulate both the electrons and nuclei in crystals quantum mechanically (Grossman and Mitas, 2005; Wagner and Grossman, 2010). Among those, we highlight the coupled electron-ion Monte Carlo method due to Pierleoni, Ceperley, and collaborators (Pierleoni, Ceperley, and Holzmann, 2004; Pierleoni and Ceperley, 2005; Pierleoni and Ceperley, 2006), for its special relevance to the field of quantum solids (see, for instance, Sec. VIII.A). In view of this progress, we foresee that in the future the use of eQMC techniques will become more popular within the community of computational condensed matter scientists.

B. Effective interaction models

Using first-principles methods to describe the interactions between atoms in quantum crystals normally requires intensive computational resources. Fortunately, the interactions between particles sometimes are so *simple* that they can be approximated with analytical functions known as classical interatomic potentials or force fields. In those particular cases one can concentrate on solving the quantum-mechanical equations for the nuclear degrees of freedom only, hence accelerating the calculations dramatically. Classical interaction models are constructed by following physical knowledge and intuition; they normally contain a set of parameters that are adjusted to reproduce experimental or *ab initio* data. The force matching method due to Ercolessi and Adams (1994), for instance, is a well-established force field fitting technique that is widely employed in computational physics and materials science (Masia, Guàrdia, and Nicolini, 2014). Nevertheless, the ways in which classical interatomic potentials are constructed are neither straightforward nor uniquely defined, and the thermodynamic intervals over which they remain reliable are not known *a priori*.

In situations where the use of first-principles methods is prohibitive and the available classical potentials are not versatile enough to reproduce the physical phenomena of interest, machine learning techniques can be useful. Machine learning (ML) is a subfield of artificial intelligence that exploits the systematic identification of correlation in data sets to make predictions and analysis (Behler, 2010; Rupp, 2015). Effective potentials resulting from ML are not built on physically motivated functional forms but obtained from purely mathematical fitting techniques that reproduce a set of reference data as closely as possible. Some of these fitting procedures strongly rely on the concept of artificial neural networks, which can "learn" the topology of a potential-energy surface (PES) from a set of reference points. ML techniques are common tools in mathematics and computer science and are starting to be applied with confidence in

chemistry (Raghunathan *et al.*, 2015) and physics (Manzhos, Yamashita, and Carrington, 2009; Li, Kermode, and Vita, 2015).

1. Classical potentials

The interactions between atoms in quantum solids have been traditionally modeled with two-body potentials. The most popular of all the two-body potentials is the LJ potential, which is expressed as

$$V_2^{\mathrm{LJ}}(r) = 4\epsilon\left[\left(\frac{\sigma}{r}\right)^{12} - \left(\frac{\sigma}{r}\right)^{6}\right], \tag{70}$$

where ϵ and σ are free parameters, and r is the distance between two particles. The first term in Eq. (70) represents repulsive short-ranged electrostatic and Pauli-like interactions acting between electrons; the second term represents the attractive long-ranged van der Waals interactions resulting from instantaneous electronic dipoles. In spite of its simplicity, the LJ potential has been used in the study of condensed matter systems with great success; it was the first interaction model to be systematically employed in variational Monte Carlo simulations of quantum solids (Hansen and Levesque, 1968; Hansen, 1968; Bruce, 1972). The LJ potential is convenient also for simulating atomic systems composed of several chemical species for which the corresponding σ's and ϵ's are already known; the resulting crossed interactions then can be approximated to a good extent with the LJ parameters given by the Lorentz-Berthelot rules $\sigma_{ij} = (\sigma_{ii} + \sigma_{jj})/2$ and $\epsilon_{ij} = \sqrt{\epsilon_{ii}\epsilon_{jj}}$.

When two atoms are brought together, however, the value of the repulsive LJ term in general increases too rapidly. In quantum solids particles can be close to each other due to their zero-point motion, hence an accurate description of the atomic interactions at short distances is necessary even for low densities (Ceperley and Partridge, 1986; Boronat and Casulleras, 1994). In this context, the pairwise interaction model originally proposed by Ahlrichs, Penco, and Scoles (1977) is more appropriate since it reproduces *ab initio* results for the repulsive interactions between closed shell atoms (Hepburn, Scoles, and Penco, 1975). The form of this potential is

$$V_2^{\mathrm{Aziz}}(r) = Ae^{-ar+br^2} - f(r)\sum_{i=6,8,10}\frac{C_i}{r^i}, \tag{71}$$

where A, a, b, and C_i are free parameters, and $f(r)$ is an exponential damping function that is introduced to avoid the divergence of the $1/r^n$ terms at small distances. Aziz and collaborators worked extensively on this model to deliver an accurate description of the atomic interactions in many rare-gas systems (Aziz *et al.*, 1979; Aziz, Meath, and Allnatt, 1983; Aziz, McCourt, and Wong, 1987), hence the notation employed. Equation (71) also yields an improved description of the long-range dispersion forces as compared to the LJ model, since it contains several types of multipole interactions.

In some situations, a well-balanced description of solids cannot be attained with pairwise potentials only. This is the case, for instance, of crystals at extreme thermodynamic conditions (Loubeyre, 1987; Cazorla and Boronat, 2008a, 2015b; Cazorla and Errandonea, 2014). A possible solution to overcome this modeling difficulty is to go beyond pairwise additivity, that is, to consider higher order terms in the approximation to the atomic interactions. Several three-body interatomic potentials have been proposed in the literature (Axilrod and Teller, 1943; Cencek, Patkowski, and Szalewicz, 2009), and the most popular in the context of quantum solids is (Bruch and McGee, 1973)

$$V_3(\mathbf{x},\mathbf{y},\mathbf{z}) = \frac{\nu}{x^3y^3z^3} - Be^{-c(x+y+z)} \times (1 + 3\cos\alpha\cos\beta\cos\gamma), \tag{72}$$

where ν, B, and c are free parameters, $\{x, y, z\}$ the distance between particles in a trimer, and $\{\alpha, \beta, \gamma\}$ the corresponding interior angles. V_3 is an interatomic potential that renders triple dipole and exchange interactions; inclusion of this type of force appears to be necessary for obtaining a realistic description of the energy and elastic properties of very dense quantum solids (Grimsditch, Loubeyre, and Polian, 1986; Pechenik, Kelson, and Makov, 2008; Cazorla and Boronat, 2015b).

2. Machine learning

When calculations are performed in a series of similar systems or a number of configurations involving the same system, the results contain redundant information. One example is to run a molecular dynamics simulation in which the total internal energy and atomic forces are calculated at each time step; after a sufficiently long time, points which are close in configurational space and have similar energies are visited during the sampling of the potential-energy surface. Such a redundancy can be exploited to perform computationally intensive calculations (that is, of first-principles type) only in a few selected configurations and to use ML to interpolate between those, hence obtaining approximate solutions for the remaining of configurations (see Fig. 4). The success of this

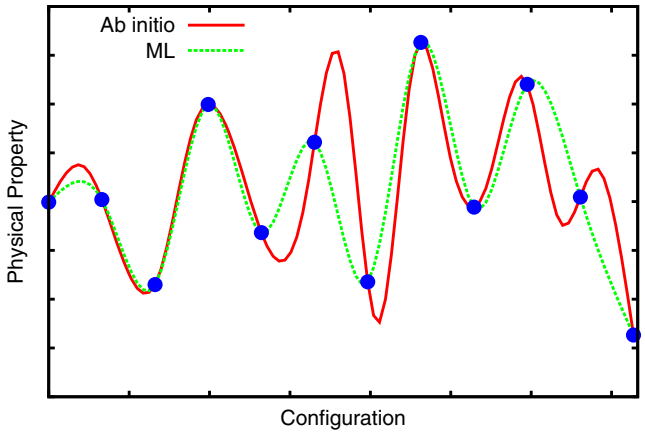

FIG. 4. Sketch of the key idea behind machine learning for the modeling of atomic interactions. *Ab initio* results (solid line), which are obtained at high computational cost, are approximated by interpolating with ML potentials (dashed line) between selected reference configurations (blue dots).

approach depends on a balance between incurred errors due to interpolation and invested computational effort.

ML modeling tools can provide both the energy and atomic forces directly from the atomic positions, hence they can be regarded as a particular class of atomistic potentials. ML potentials, however, rely on very flexible analytic functions rather than on physically motivated functionals. Promising analytic approaches that have recently been proposed to construct ML potentials include permutation invariant polynomials (Brown *et al.*, 2003), the modified Shepard method using Taylor expansions (Bowman, Czakó, and Fu, 2011), Gaussian processes (Bartók *et al.*, 2010, 2013), interpolating moving least squares (Dawes *et al.*, 2007), and artificial neural networks (Lorenz, Groß, and Scheffler, 2004). Artificial neural networks, for instance, have been demonstrated to be "universal approximators" (Behler, 2015) since they allow one to approximate unknown multidimensional functions to within arbitrary accuracy given a set of known function values.

To the best of our knowledge, ML potentials have not been applied yet to the study of quantum solids. However, the great versatility of ML approaches (Behler, 2010, 2015; Rupp, 2015) could be exploited to describe such systems in especially challenging situations such as, for instance, molecular solids (e.g., H_2, N_2, and CH_4) under extreme thermodynamic conditions. Classical interaction models normally disregard the orientational degrees of freedom in molecules and require the specification of bond connectivity between atoms. Therefore, they are not able to describe the orientational phase transitions and breaking and formation of atomic bonds occurring at high-P and high-T conditions (see Sec. VIII). ML potentials could represent an intermediate solution between classical potentials and first-principles methods, in terms of both numerical accuracy and computational burden.

IV. ARCHETYPAL QUANTUM CRYSTALS

Helium and hydrogen are the lightest elements in nature and the paradigm of quantum solids. The classical picture of a crystal at low temperature, with all the atoms strongly localized around their equilibrium lattice positions, breaks completely in solid helium and hydrogen. In archetypal quantum crystals atoms move noticeably around the equilibrium lattice positions even in the limit of zero temperature, and exchanges between few particles occur with frequency. Consequently, the degree of anharmonicity in these systems is very high. Quantum simulation methods beyond the harmonic approximation (see Sec. II) in fact are necessary for correctly describing archetypal quantum solids.

A. Helium

Helium has two stable isotopes, ^{4}He and ^{3}He, which are bosonic and fermionic particles, respectively. Both isotopes solidify under moderate pressures in the $T \to 0$ limit, namely, at $P \simeq 25$ bar in ^{4}He and 30 bar in ^{3}He. ^{4}He solidifies in the hexagonal hcp phase except for a small region at low pressures in which the stable phase is cubic bcc (see Fig. 5). Meanwhile, ^{3}He solidifies in the cubic bcc phase with a relatively large molar volume of $V \simeq 24.5$ cm^3 mol^{-1}. Under specific $P-T$ conditions, both isotopes transform into the cubic fcc phase (Glyde, 1994).

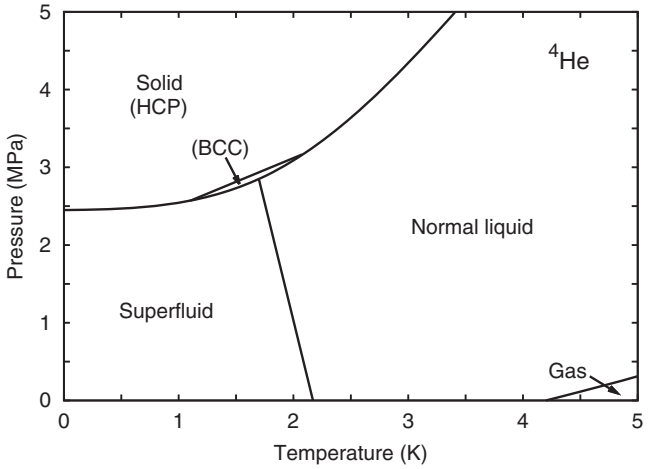

FIG. 5. Phase diagram of ^{4}He at low pressures and temperatures.

At low pressure ($P < 1$ GPa), the thermodynamic properties of solid ^{4}He are well known from experiments and accurately reproduced by QMC methods. In Fig. 6, we compare experimental and computational results for the dependence of the energy per particle on density. The theoretical results correspond to DMC simulations performed by Vranješ *et al.* (2005) using a semiempirical pair potential (Aziz, McCourt, and Wong, 1987); the agreement between observations and theory is excellent. Likewise, accurate results have also been obtained with the PIGS method (Rossi *et al.*, 2012). From the function $E/N(\rho)$ one can easily work out the pressure $P(\rho) = \rho^2 d(E/N)/d\rho$ thus obtaining the corresponding eos. Excellent agreement

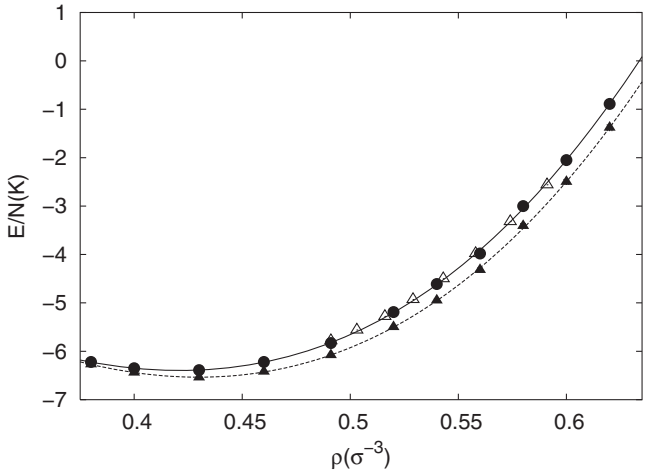

FIG. 6. Energy per particle in solid ^{4}He expressed as a function of density. Open triangles represent experimental data from Edwards and Pandorf (1965). Other symbols and lines correspond to the DMC results. Solid circles and line represent results in which the bias introduced by finite-size effects has been reduced significantly. Solid triangles and dashed line represent results which have been corrected only partially for the same type of bias. Adapted from Vranješ *et al.*, 2005.

between theory and experiment has also been demonstrated for this quantity [see, for instance, Cazorla and Boronat (2008a)]. The quantum nature of solid ^{4}He is thermodynamically reflected in its high compressibility; for instance, the corresponding experimental molar volume is reduced from 21 cm^3 mol^{-1} at 25 bar to 9 cm^3 mol^{-1} at 5 kbar. The location of the first-order liquid-solid phase transition is also accurately reproduced by QMC calculations. Recent DMC estimations provide a transition pressure of 27.3 atm, with freezing and melting densities equal to $\rho_f = 0.437\sigma^{-3}$ and $\rho_m = 0.481\sigma^{-3}$ ($\sigma = 2.556$ Å), respectively (Vranješ *et al.*, 2005). The corresponding experimental values are $P_t^{\text{expt}} = 25$ atm, $\rho_f^{\text{expt}} = 0.434\sigma^{-3}$, and $\rho_m^{\text{expt}} = 0.479\sigma^{-3}$ (Glyde, 1994).

Valuable information on the quantum nature of a solid is obtained from its Lindemann ratio:

$$\gamma = \frac{1}{a}\left[\frac{1}{N}\sum_{i=1}^{N}(\boldsymbol{r}_i - \boldsymbol{R}_i)^2\right]^{1/2} = \frac{\langle \boldsymbol{u}^2\rangle^{1/2}}{a}, \tag{73}$$

where $\boldsymbol{R}_i$ represent the coordinates of the perfect lattice sites, and a the corresponding lattice constant. The parameter γ quantifies the displacement of particles around their equilibrium positions. The quantum character of a solid can be said to be proportional to the value of its Lindemann ratio. In solid ^{4}He and ^{3}He at ultralow temperatures, for instance, γ amounts to ~0.3 (Glyde, 1994), which are the largest values known in any material at those thermodynamic conditions. The large excursions of helium atoms around their lattice positions allow them to explore the nonharmonic part of the potential-energy surface, leading to high anharmonicity. Another singular aspect in solid helium is the large kinetic energy per particle. At $P = 50$ atm, for instance, E_k amounts to ~24 K (Diallo *et al.*, 2007), which is of the same order of magnitude as the corresponding potential energy, namely, ~ -31 K (which results from a cancellation between large repulsive and attractive terms).

The influence of Bose-Einstein statistics on the energy and structural properties of solid ^{4}He is negligible [~1 μK/atom (Clark and Ceperley, 2006)]. In fact, many of the results just presented have been obtained with nonsymmetric wave functions and as explained the agreement with the experiments is excellent. However, quantum atomic exchanges play a pivotal role in other intriguing properties such as, for instance, Bose-Einstein condensation and superfluidity (Ceperley, 1995). These phenomena occur in liquid ^{4}He at ultralow temperatures and, due to the extreme quantum nature of helium, it was wondered a long time ago whether the same effects could also be observed in the crystal phase (see Sec. VI for a historical overview of this topic). In recent years, there have been several theoretical works aimed at clarifying these questions. In particular, the one-body density matrix $\varrho_1(r)$ [Eq. (49)] of solid ^{4}He has been calculated with different methods. Initial zero-temperature estimations based on symmetrized wave functions (Galli and Reatto, 2006; Cazorla *et al.*, 2009) provided a nonzero but small plateau at long distances. However, unbiased $\varrho_1(r)$ results obtained with the PIGS and PIMC methods have unequivocally demonstrated that the condensate fraction in perfect solid ^{4}He is actually zero (Ceperley and Bernu, 2004; Bernu and Ceperley, 2005; Boninsegni, Prokof'ev, and Svistunov, 2006b; Clark and Ceperley, 2006). In particular, the tail of $\varrho_1(r)$ decays exponentially at long distances as illustrated in Fig. 7 (Rota and Boronat, 2012). Actually, the exchange frequency between particles at different lattice sites is very small as compared to that in the liquid phase [for instance, the exchange frequency for 2, 3, and 4 atom exchanges is of ~3 μK/atom (Ceperley and Bernu, 2004; Clark and Ceperley, 2006)], and long permutation cycles able to trigger superfluidity are highly improbable. Nevertheless, note that when a finite and stable concentration of defects is assumed to exist in the crystal these conclusions change drastically (see Sec. VI).

At high pressures, the atoms in a crystal experience strong short-range repulsions due to electrostatic forces and the Pauli exclusion principle. Customary semiempirical potentials that at low densities provide a good description of the crystal then start to be unreliable due to severe transferability issues (see Sec. III.B). This is the case of the Aziz potential for ^{4}He (Aziz, McCourt, and Wong, 1987), which possesses a too steep repulsive core and leads to inaccurate results at pressures $P \geq 1$ GPa (Cazorla and Boronat, 2008a). Recently, dispersion-corrected DFT has been used in combination with the DMC method to study the quantum behavior of solid helium at pressures up to ~150 GPa (Cazorla and Boronat, 2015a, 2015b). Essentially, analytical potentials have been constructed to reproduce sets of atomic energies and forces calculated with first-principles methods. To a first approximation (Cazorla and Boronat, 2015a), the effective pair interaction has been obtained by fitting the static compression curve calculated with DFT-D to an analytical function based on the Aziz potential [see Eq. (71)] and an attenuation repulsion factor proposed by Moraldi (2012). This has allowed for a sizable improvement in the description of the high-P eos as compared to the available experimental data. However, it has been shown that such a simple approach

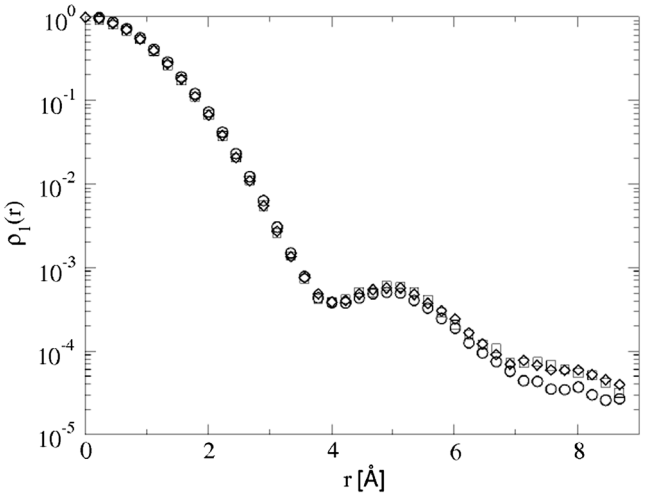

FIG. 7. One-body density matrix calculated in hcp ^{4}He at density $\rho = 0.0294$ Å^{-3}. Circles, squares, and diamonds stand for results obtained at $T = 0$, 1, and 2 K, respectively. Adapted from Rota and Boronat, 2012.

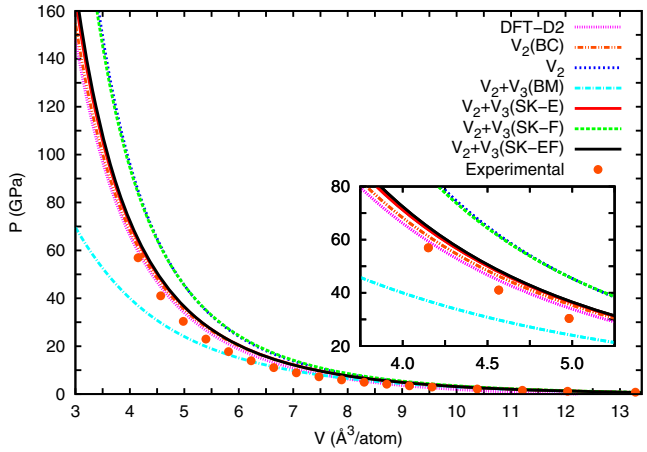

FIG. 8. Zero-temperature equation of state of hcp ^{4}He at high pressures calculated with several effective three-body interaction models fitted to reproduce *ab initio* data, and the DFT-D method (see text). Experimental data from Loubeyre *et al.* (1993) are shown for comparison. Inset: $P(V)$ curves in the high-P region are magnified in order to better appreciate the differences. From Cazorla and Boronat, 2015b.

provides unphysical results for the elastic constants and pressure dependence of the kinetic energy. In a later work, Cazorla and Boronat (2015b) introduced a family of three-body interaction potentials based on Eq. (72) that allow one to overcome (in part) these modeling shortcomings while still providing an accurate eos up to ∼60 GPa (see Fig. 8).

With regard to solid ^{3}He, the number of related studies is very limited. Besides some old variational calculations, the most recent and accurate investigation of its thermodynamic properties has been performed by Moroni *et al.* (2000) with the DMC method. In Moroni's work the quantum antisymmetry of the system is neglected, that is, particles are treated as bosons rather than as fermions. Nevertheless, since the exchange energy in the crystal is very small (of the order of mK) (Ceperley and Jacucci, 1987; Cândido, Hai, and Ceperley, 2011) it can be expected that quantum symmetry effects will play an insignificant role on the energy. The results obtained for the dependence of the energy on density show a discrepancy with the experimental data, which Moroni *et al.* (2000) attributed to a wrong reference in the integration of the experimental equation of state. After correction of such an error, the agreement between theory and experiments becomes excellent, namely, of the same quality as that achieved in solid ^{4}He.

B. Hydrogen

Bulk molecular hydrogen (deuterium) at zero pressure, in contrast to ^{4}He, solidifies at a temperature of ∼14 K (∼19 K) due to the stronger attractive interactions between particles. H_2 (D_2) molecules are composed of two hydrogen (deuterium) atoms joined by a covalent bond, which in the parahydrogen (orthodeuterium) state have zero angular momentum and spherically symmetric wave functions. Both types of particles, therefore, are bosons and the interactions between molecules of the same species can be modeled with radial pairwise potentials (at high pressures, however, the molecular angular momentum is no longer zero and thereby pairwise approximations to the intermolecular interactions become invalid, see Sec. VIII.A). Actually, in most quantum simulation studies of H_2 and D_2 crystals at low pressure (i.e., $P \leq 0.1$ GPa) the intermolecular forces have been modeled with the semiempirical Silvera-Goldman (Silvera and Goldman, 1978) and Buck (Buck *et al.*, 1983; Norman, Watts, and Buck, 1984) pair potentials. The effect of three-body forces on the corresponding low-P equation of state has been explored, but their net effects have been found to be negligible (Operetto and Pederiva, 2006). Meanwhile, anisotropic corrections to the pair potential have been tested against experiments and found to be significant only at pressures higher than ∼10 GPa (Cui *et al.*, 1997).

In Fig. 9, we show the energy per molecule in hexagonal hcp H_2 calculated in the limit of zero temperature with the DMC method and the Silvera-Goldman potential (Osychenko, Rota, and Boronat, 2012). We note that the experimental energy per particle is $E/N = -89.9$ K, which is underestimated (overestimated) by the Silvera-Goldman (Buck) potential model. Close to the equilibrium density the H_2 kinetic energy is 89.5 K, which roughly amounts to half of the potential energy. In comparison to solid ^{4}He, in which both types of energies are nearly equal, quantum nuclear effects in solid hydrogen turn out to be smaller (see also Fig. 1). The energy curve of the metastable liquid is shown in Fig. 9 for comparison. Results for the equation of state of solid and liquid H_2 are enclosed in Fig. 10. The agreement between theory and experiments (Driessen, de Waal, and Silvera, 1979) is quite satisfactory in the solid phase, although at pressures beyond ∼100 MPa this starts to worsen due to the limitations of the employed intermolecular potential (Moraldi, 2012; Omiyinka and Boninsegni, 2013).

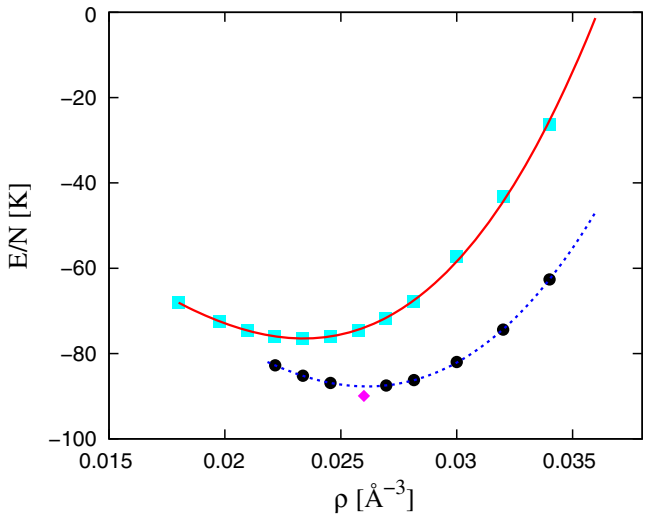

FIG. 9. DMC energy per H_2 molecule as a function of density. Squares and circles correspond to the liquid and solid phases, respectively. Solid and dashed lines are polynomial fits to the DMC energies for the liquid and solid phases, respectively. The diamond represents the experimental energy of hcp molecular hydrogen from Schnepp (1970). From Osychenko, Rota, and Boronat, 2012.

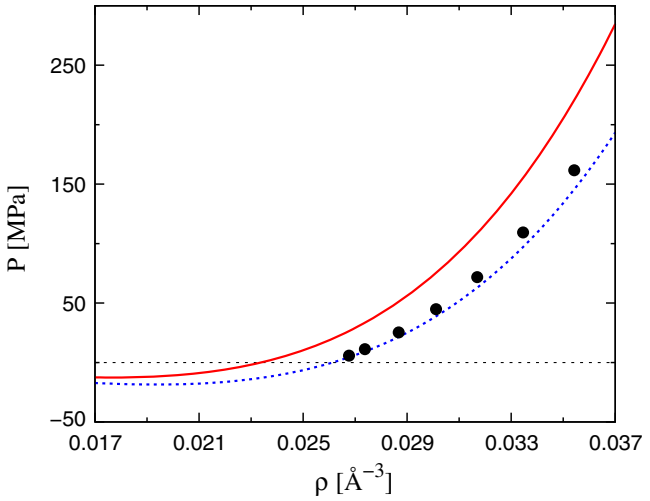

FIG. 10. Equation of state of liquid (solid line) and solid (dashed line) H_2. Experimental points for the solid phase are represented with solid circles (Driessen, de Waal, and Silvera, 1979). From Osychenko, Rota, and Boronat, 2012.

As a by-product of the recent experimental activity on the search for a supersolid state of matter (see Sec. VI), interest has developed in studying highly disordered solids such as, for instance, amorphous or glassy systems. A glassy state in solid ^{4}He, termed a "superglass," has been predicted to exhibit superfluid behavior by Boninsegni, Prokof'ev, and Svistunov (2006b). An analogous study has been carried out more recently in solid H_2 by Osychenko, Rota, and Boronat (2012). In this case, PIMC simulations showed that glassy molecular hydrogen eventually becomes superfluid at temperatures below ∼1 K. The critical temperature for this transition, however, is so small that it is unlikely to be observed in experiments (Kühnel *et al.*, 2011).

Interestingly, the free surface of bulk H_2 has also been investigated with experiments (Brewer *et al.*, 1990; Vilches, 1992; Kinder, Bouwen, and Schoemaker, 1995) and PIMC simulations (Wagner and Ceperley, 1994, 1996). It was found that the melting temperature of the bare hydrogen surface is reduced down to ∼6 K and that zero-point molecular fluctuations therein are considerably enhanced with respect to bulk. For instance, at low temperatures the corresponding Lindemann ratio increases from ∼0.1 in the inner layers up to ∼0.2 in the outer surface (Wagner and Ceperley, 1996). Yet, the corresponding melting temperature is still too high to expect that liquid H_2 will become superfluid (that is, well above the predicted critical temperature $T_c \sim 1$–2 K) (Apenko, 1999).

C. Neon

Solid neon behaves more "classically" than solid helium but more "quantumly" than the rest of the rare-gas species (see Fig. 1). The study of this crystal is useful to understand the transition from the quantum regime to the classical in solid-state systems. The interest in solid neon as a case study of a moderate quantum system dates back to the 1960s. Bernades (1958) and Nosanow and Shaw (1962) were the first to attempt an estimation of the kinetic energy in solid neon using theoretical methods. By relying on variational and self-consistent Hartree calculations performed with uncorrelated single-particle wave functions, they reported ground-state E_k values of ∼41 K. However, the binding energies reported in those early works were in strong disagreement with contemporary experiments, evidencing the need to go beyond uncorrelated microscopic approaches. A few years later, Koehler (1966) applied the self-consistent phonon approach to the same system and obtained results for the cohesive energy that were in better agreement with the experiments; Koehler's estimation of the kinetic energy was 42.6 K.

It was not until the 1990s that, with the development of the deep inelastic neutron scattering technique, the kinetic energy in quantum crystals could be measured precisely. Peek *et al.* (1992) were the first to perform those measurements in solid neon, reporting a ground-state kinetic energy of 49.1 (2.8) K. In view of the large discrepancies found with respect to previous estimations based on harmonic models, they suggested that solid neon was highly anharmonic. Later on, Timms *et al.* (1996) carried out a new series of neutron scattering experiments in which higher momentum and energy transfers were considered. They found that in the temperature interval of 4–20 K their measured excess kinetic energies, defined as $E_{exc} \equiv E_k - \frac{3}{2}k_B T$, were systematically lower than Peek's results by a few Kelvin (see Fig. 11). The validity of Timms *et al.*'s results is supported by the outcomes of several PIMC studies based on classical interatomic potentials (Cuccoli *et al.*, 1993; Timms *et al.*, 1996; Neumann and Zoppi, 2002). More recently, Timms, Simmons, and Mayers (2003) performed additional neutron scattering measurements and reported that the ground-state kinetic energy in solid neon is 41 (2) K. The accuracy of this result has been confirmed by recent DMC calculations performed by Cazorla and Boronat (2008b), which provide $E_k = 41.51\ (6)$ K in the $T \to 0$ limit (see Fig. 11). We note that the Lindemann ratio (see Sec. I.C) in solid neon is approximately 3 times smaller than in helium, namely, $\gamma_{Ne} \sim 0.08$ (Cazorla and Boronat, 2008b), pointing to a moderate degree of quantumness.

An interesting topic in the study of solid neon is related to the shape of its momentum distribution $n(\mathbf{k})$ (see Fig. 11). Withers and Glyde (2007) showed that when a crystal has a momentum distribution that is not well described by a Gaussian, it may be due to the fact that the system is highly anharmonic or that quantum atomic exchanges occur frequently. While quantum atomic exchanges are very likely to be negligible, anharmomic effects seem to be fairly important in solid neon. This was demonstrated by Cazorla and Boronat (2008b), who performed different types of harmonic-based calculations and compared their results to those obtained with full anharmonic methods. For instance, the ground-state kinetic energy that is predicted with the self-consistent average phonon approach (Shukla *et al.*, 1981) amounts to ∼47 K and the corresponding Lindemann ratio to 0.06, which are appreciably different from the experimental and DMC results.

Nevertheless, there is widespread agreement among experimentalists and theorists in that the momentum distribution in solid Ne is well approximated by a Gaussian function (Timms *et al.*, 1996; Neumann and Zoppi, 2002; Cazorla and Boronat, 2008b). The question then arises about how anharmonic (or

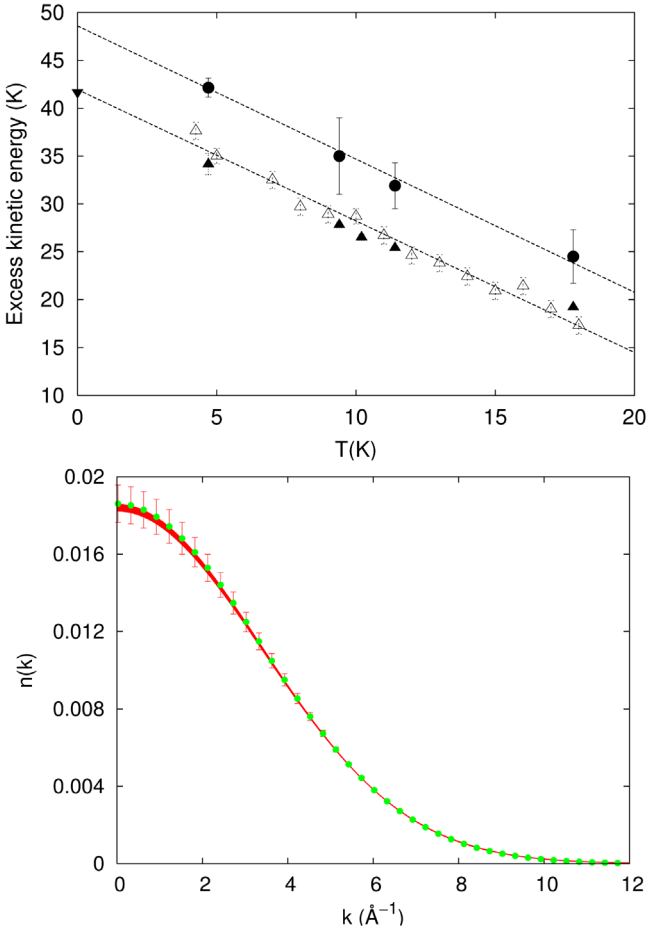

FIG. 11. Quantum nuclear effects in solid neon at low temperatures. (Top panel) Excess kinetic energy expressed as a function of temperature. Open up triangles: experimental data from Timms, Simmons, and Mayers (2003). Solid circles: measurements from Peek *et al.* (1992). Solid up trianges: PIMC calculations from Timms *et al.* (1996). Solid down triangle: DMC ground-state calculations from Cazorla and Boronat (2008b). The lines in the plot are linear fits to the experimental data. (Bottom panel) Ground-state momentum distribution in solid Ne calculated with the DMC method (green dots). The solid line (red) is a Gaussian fit to the results, the width of which represents its uncertainty. Adapted from Cazorla and Boronat, 2008b.

quantum) a crystal must be for its $n(\mathbf{k})$ to differ appreciably from a Gaussian. The momentum distribution in solid ^{4}He is non-Gaussian as it has a large occupation of low momentum states as compared to a Maxwell-Boltzmann distribution (Diallo *et al.*, 2004; Rota and Boronat, 2011). However, little is known about the relation between anharmonicity and $n(\mathbf{k})$ in other quantum crystals lying in between helium and neon, in terms of quantumness, which are mostly molecular systems (see Fig. 1). In the case of solid para-H_2, for instance, inelastic neutron scattering experiments have provided a translational momentum distribution that is Gaussian (Langel *et al.*, 1988); however, it is not clear whether this result can be attributed to the intensive use of Gaussian approximations during the refinement of experimental data (Colognesi *et al.*, 2015). Is solid helium the only quantum crystal with a non-Gaussian $n(\mathbf{k})$? The answer so far seems to be yes.

Free-energy calculations based on path-integral simulations and semiempirical pairwise potentials have also been employed to study the quantum phase diagram of neon up to pressures of 2–3 kbar and temperatures of 50 K (Ramírez and Herrero, 2008; Ramírez *et al.*, 2008; Brito and Antonelli, 2012). Significant QNE have been found in the solid-gas and liquid-gas $P-T$ coexistence lines, which consist of a shift of about 1.5 K toward lower temperatures as compared to the classical phase diagram. Moderate quantum isotopic effects have also been observed in the triple solid-liquid-gas coexistence point in both experiments (Furukawa, 1972) and path-integral calculations (Ramírez and Herrero, 2008).

V. ELASTICITY AND MECHANICAL PROPERTIES

The free energy of a crystal subjected to a homogeneous elastic deformation is

$$F(V,T,\epsilon) = F_0(V,T) + \frac{1}{2}V\sum_{ij} C_{ij}\epsilon_i\epsilon_j, \tag{74}$$

where F_0 is the free energy of the undeformed solid, C_{ij} are the corresponding elastic constants, and ϵ_i are general strain deformations (the latter two quantities are expressed in Voigt notation and the subscripts indicate Cartesian directions). The symmetry of the crystal determines the number of elastic constants that are inequivalent and nonzero. For a crystal to be dynamically stable, its change in free energy due to an arbitrary strain deformation must be always positive; this requirement leads to a number of mechanical stability conditions that need to be fulfilled for any stable or metastable state, and which depend on the particular symmetry of the crystal (Born and Huang, 1954; Grimvall *et al.*, 2012).

The elastic constants of a solid can be measured with ultrasonic techniques since the velocity of density waves depends on the elastic properties of the medium in which they propagate. Brillouin scattering spectroscopy and synchrotron x-ray diffraction techniques can also be employed to this end. Likewise, the calculation of elastic constants with quantum simulation methods is a well-established technique. At zero temperature, one can calculate the energy of the solid as a function of strain, using for instance the DMC or PIGS method (see Sec. II.A), and then simply compute the value of its second derivative numerically (Cazorla, Lutsyshyn, and Boronat, 2012, 2013). At $T \neq 0$, the calculation of C_{ij}'s is not so straightforward since one has to consider also the effects of thermal excitations. Schöffel and Müser (2001) were the first to undertake such a type of calculation by using the path-integral Monte Carlo method. They estimated the elastic constants in solid Ar and ^{3}He through direct derivation of the partition function with respect to the strain components. More recently, Peña-Ardila, Vitiello, and de Koning (2011) proposed an alternative path-integral approach in which a suitable expression for the estimation of the stress tensor is worked out.

In this section, we review the elastic properties of *perfect* quantum solids, that is, free of crystalline defects. Crystalline defects can considerably affect the elastic behavior of quantum (and also classical) crystals, so that we leave those aspects for Sec. VI. Our analysis here is divided into low and high

pressures because the fundamental character of elasticity in quantum crystals changes when moving from one regime to the other.

A. Low-pressure regime

The elastic properties of traditional quantum solids such as helium (Crepeau *et al.*, 1971; Greywall, 1977) and hydrogen (Nielsen and ller, 1971; Nielsen, 1973; Wanner and Meyer, 1973) have been measured extensively. In experiments, however, it is difficult to determine the exact contribution of QNE to elasticity. In this context, the outcomes of first-principles studies can be valuable. For instance, Schöffel and Müser (2001) performed a thorough PIMC study on the elastic properties of solid ^{3}He in the hexagonal hcp and cubic bcc and fcc phases, considering low temperatures and pressures. Their results were in good agreement with the reported experimental data, and they concluded that QNE accounted for about 30% of the C_{ij} values. A similar quantum influence on the elasticity of solid Ar was also reported (namely, ∼20%), a crystal that is considered to behave much more classically than helium.

More recently, the elastic properties of solid ^{4}He have been studied in detail using different QMC techniques. Cazorla, Lutsyshyn, and Boronat (2012) employed the DMC method to calculate the zero-temperature elastic constants, Grüneisen parameters, sound velocities, and Debye temperature over a wide pressure interval of ∼100 bar. The computed C_{ij} values are in overall good agreement (i.e., discrepancies to less than 5% in most cases) with the reported experimental data and results obtained using the VMC (Pessoa, Vitiello, and de Koning, 2010; Pessoa, de Koning, and Vitiello, 2013) and PIMC (Peña-Ardila, Vitiello, and de Koning, 2011) methods (see Fig. 12). It was found that the pressure dependence of all five elastic constants close to equilibrium is practically linear (see Fig. 12). Interestingly, the contribution of QNE to the elastic constants in hcp ^{4}He has been shown to be ∼30%, which roughly coincides with the results obtained by Schöffel and Müser (2001) in solid ^{3}He. In essence, all these theoretical studies conclude that QNE profoundly affect the elastic properties of quantum crystals at low pressures (that is, $P \leq 0.01$ GPa).

A fundamental question that can be easily addressed with simulations but not with experiments is what is the limit of mechanical stability in a quantum crystal? When the density in a system is reduced progressively, eventually this becomes unstable against long wavelength density fluctuations. This limit, also known as the spinodal point, has been comprehensively analyzed in liquid ^{4}He and ^{3}He (Boronat, Casulleras, and Navarro, 1994; Maris, 1995; Maris and Edwards, 2002); however, it has not been until recently that it was estimated directly in the crystal phase (Cazorla and Boronat, 2015c). Theoretically, the spinodal point in a crystal is identified with the thermodynamic state at which any of the mechanical stability conditions involving the elastic constants is not satisfied. One can expect that, due to the presence of QNE and inherent structural softness, the limit of mechanical stability in quantum crystals lies very low in density.

Based on C_{ij} calculations performed with the DMC method and a semiempirical pairwise potential, Cazorla and Boronat (2015c) estimated that the ground-state spinodal pressure

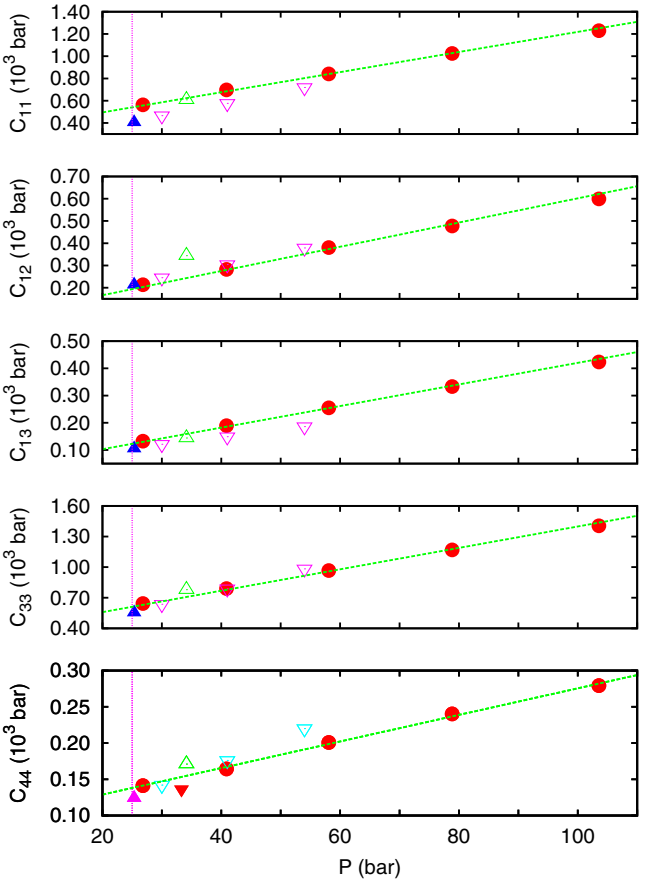

FIG. 12. Elastic constants in solid ^{4}He at moderate pressures. Solid up triangles: experimental data from Crepeau *et al.* (1971); open down triangles: Greywall (1977). Solid down triangles: C_{44} measurements from Syshchenko, Day, and Beamish (2009). Open up triangles: VMC calculations from Pessoa, Vitiello, and de Koning (2010). Solid circles: DMC ground-state calculations from Cazorla, Lutsyshyn, and Boronat (2012). The dashed lines (green) represent linear fits to the DMC results. The freezing pressures in the crystals are marked with vertical (magenta) lines. Adapted from Cazorla, Lutsyshyn, and Boronat, 2012.

in solid ^{4}He is $P_s = -33.8(1)$ bar, which corresponds to an atomic volume of $V_s = 50.81(5)$ Å^3. In particular, it was found that the mechanical stability condition $(C_{33} - P)\times(C_{11} + C_{12}) - 2(C_{13} + P)^2 > 0$ is violated at P_s. Regarding the propagation of density waves, previous calculations based on phenomenological models (Maris, 2009, 2010) had suggested that, in analogy to the liquid phase, the sound velocities in hcp ^{4}He near the spinodal density could follow a power law of the form $\propto (P - P_s)^{1/3}$. However, Cazorla and Boronat (2015c) showed that quantum solids and liquids behave radically different in the vicinity of their mechanical stability limits; in particular, none of the sound velocity components, either propagating along the c axis or in the basal plane, follow the previously proposed "1/3" power law.

B. High-pressure regime

The elastic properties of archetypal quantum solids under high pressure (i.e., $P > 1$ GPa) have been thoroughly

investigated with experiments (Zha *et al.*, 1993; Zha, Mao, and Hemley, 2004). Surprisingly, the results of first-principles DFT studies in which QNE are completely or partially neglected show good agreement with the measured C_{ij} and sound velocity data (Nabi *et al.*, 2005; Freiman *et al.*, 2013; Grechnev *et al.*, 2015). In view of the importance of QNE on the elastic properties of quantum crystals at low pressures (see Sec. V.A), such good agreement could be explained in terms of (i) a systematic error cancellation involving the disregard of QNE, on the one hand, and an inaccurate description of the system obtained with standard DFT functionals, on the other hand, or (ii) a steady diminishing of the importance of QNE on elasticity under pressure.

To the best of our knowledge, there are no fully *ab initio* studies (i.e., works in which both the electronic and ionic degrees of freedom are described with quantum-mechanical methods) on the elastic properties of highly compressed quantum crystals. The reason for this is likely to be the large computational expense associated with the calculation of partition function derivatives or the stress tensor with sufficient accuracy (Schöffel and Müser, 2001; Peña-Ardila, Vitiello, and de Koning, 2011). On the other hand, the semiempirical two-body potentials that at low pressures describe the interactions between atoms in quantum crystals correctly become unreliable at high pressures (see Sec. III). In addition to this, pairwise interaction models in general are not well suited for the study of elasticity in very dense crystals since they inevitably lead to zero values of the Cauchy relations (Wallace, 1972; Pechenik, Kelson, and Makov, 2008), which is inconsistent with the observations (Zha, Mao, and Hemley, 2004). Assessing the importance of QNE on the elasticity of quantum crystals by using such unrealistic interatomic potentials, therefore, could be misleading.

Cazorla and Boronat (2015b) recently introduced a set of effective three-body potentials based on Eq. (72), to simulate solid ^{4}He at high pressures realistically and with affordable computational effort (see Sec. IV.A). The new parametrizations have been obtained from fits to *ab initio* energies and atomic forces calculated with a dispersion-corrected DFT functional (see Sec. III.A.1). It has been shown that an overall improvement in the description of ^{4}He elasticity at zero temperature and pressures $0 \leq P \leq 25$ GPa can be achieved with some of the proposed three-body interaction models. Interestingly, Cazorla and Boronat (2015b) found that the impact of QNE on helium elastic constants becomes secondary at very large densities. For instance, the inclusion of QNE makes the value of the shear modulus C_{44} to decrease by less than 4% at a pressure of ∼50 GPa (to be compared with ∼30% found near equilibrium conditions). This conclusion appears to be consistent with the results of a recent PIMC study performed by Landinez-Borda, Cai, and de Koning (2014), in which the ideal shear strength on the basal plane of solid helium (that is, the maximum stress that the crystal can resist without yielding irreversibly) was found to behave quite similarly to that in classical hcp solids. Consequently, it can be expected that by treating QNE with approximate methods (e.g., the Debye model or quasiharmonic approximations) one can obtain a reasonably good description of elasticity in quantum solids at high pressures. It will be interesting to test whether this is also valid in quantum molecular crystals, the elastic properties of which remain largely unexplored at high densities with theory.

VI. CRYSTALLINE DEFECTS

Crystals are characterized by periodic arrangements of atoms or molecules defined by a unit cell. The regular pattern in a solid, however, normally is interrupted by crystalline defects, which can be classified into point, line, and planar types. Point defects occur only at or around one lattice site, and typical examples include vacancies, impurities, and interstitials (Kittel, 2005); see Fig. 13. Line defects entail entire rows of atoms that are misaligned with respect to the others; common examples of line defects are dislocations, which in turn are classified into "edge" and "screw" (Bulatov and Cai, 2006; Hull and Bacon, 2011). An edge dislocation, for instance, is created by introducing an extra half-plane of atoms midway through the crystal (see Fig. 13). Planar defects can occur in single crystals or in the boundaries between single crystals and include grain and twin boundaries, steps, and stacking faults (Kittel, 2005). The study of crystalline defects is important since these can considerably affect the mechanical, electrical, structural, and adsorption properties of materials. Dislocations, for example, are key to understanding

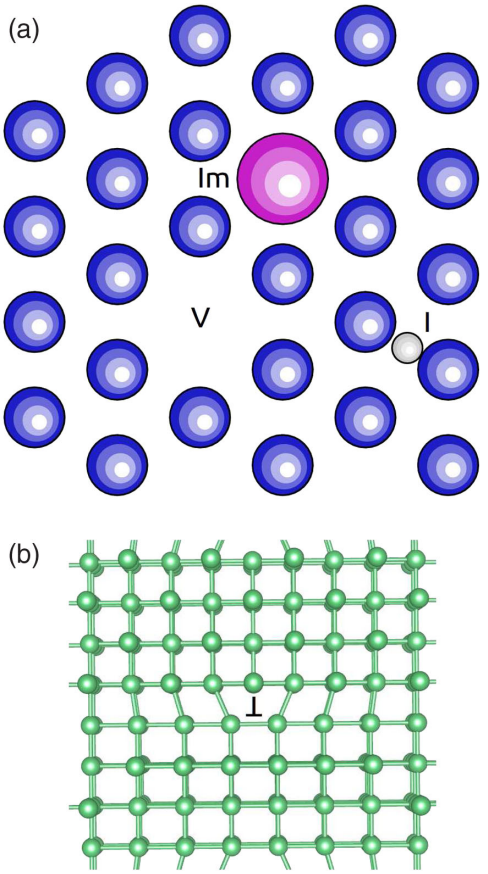

FIG. 13. Common types of defects in crystals. (a) Representation of point defects; *V*, *Im*, and *I*, respectively, stand for vacancy, impurity, and interstitial. (b) Representation of an edge dislocation, a class of line defect, in a solid with cubic symmetry.

the microscopic origins of plasticity, that is, the regime in which the mechanical deformation of a crystal becomes nonreversible (Kosevich, 2005).

In 1969, Andreev and Lifshitz proposed that a state of matter in which crystalline order and Bose-Einstein condensation coexisted could occur in a quantum crystal, the so-called supersolid. For this supersolid to exist, the presence of crystal vacancies was a necessary condition. At that time some experimentalists were attracted to the possibility of realizing such an exotic state of matter, and several mass flow and torsional oscillator experiments were carried out in solid ^{4}He at ultralow temperatures. In all those experiments, however, no evidence for a supersolid state was found. Several decades later, a renewed interest in supersolids blossomed after the torsional oscillator experiments by Kim and Chan (2004a, 2004b). In their experiments, Kim and Chan observed a shift in the period of the torsional oscillator of solid helium as the temperature was lowered below ∼0.1 K. This sign was interpreted as the mass decoupling between the normal and superfluid fractions in the crystal. Meanwhile, a few years later Day and Beamish (2007) measured the shear modulus in solid helium and found a striking resemblance with respect to the temperature dependence of the oscillation period reported by Kim and Chan: the shear modulus increased as the temperature was lowered below ∼0.1 K. Day and Beamish attributed that increase in stiffness to the temperature dependence of the mobility of dislocations in the solid, which could be pinned by static ^{3}He impurities. Day and Beamish's findings motivated a series of subsequent theoretical and experimental studies which have demonstrated that a change in the moment of inertia of the experimental torsional cell can be correlated to a change in the structure of the solid inside of it (Reppy, 2010; Maris, 2012; Shin *et al.*, 2016). In 2012, Kim and Chan completely redesigned their torsional oscillator setup making it stiffer, and the original mass-decoupling signal disappeared to within the experimental errors (Kim and Chan, 2014). Thus, any convincing evidence of the existence of a supersolid yet is to be found.

As a by-product of the frustrated investigations on supersolids, interest in the plastic behavior of quantum solids has emerged. Recently, Haziot *et al.* (2013a) showed that in ultrapure single crystals of hcp ^{4}He the resistance to shear along one particular direction nearly vanishes at around $T = 0.1$ K due to free gliding of dislocations within the basal plane. This intriguing effect has been termed giant plasticity and vanishes in the presence of numerous ^{3}He impurities or when the temperature is raised.

In this section, we review the current understanding of crystalline defects in quantum crystals. Our analysis is focused on vacancies and dislocations since these are the two types of defects that have been studied in more detail in solid ^{4}He. Special emphasis is put on identifying those aspects that remain unknown or controversial.

A. Vacancies

Both experiments and theory agree that the vacancy formation enthalpy ΔH_v in solid ^{4}He at ultralow temperatures amounts to ∼15 K (Fraass, Granfors, and Simmons, 1989; Galli and Reatto, 2004; Lutsyshyn *et al.*, 2010). The general understanding then is that vacancies cannot be thermally activated in this crystal at temperatures as low as 0.1–1.0 K. In fact, the classical equilibrium concentration of vacancies in a crystal is given by $x_v^{\text{class}} = \exp(-\Delta G_v/T)$, where ΔG_v is the Gibbs free-energy difference between the perfect and incommensurate (that is, defective) system. ΔG_v is equal to $\Delta H_v - T\Delta S_v$, where ΔS_v is the entropy change induced by the presence of vacancies. In turn, ΔS_v can be estimated as the sum of a vibrational and a configurational contribution. The vibrational contribution corresponds to the variation of the lattice phonon frequencies as a result of the local relaxation occurring around the vacancy; in the limit of very small x_v, this contribution can be safely neglected. The configurational entropy stems from the equivalency between lattice sites when creating a vacancy; this contribution is $\Delta S_v^{\text{conf}} = -\ln(x_v)$ and cannot be disregarded in the $x_v \ll 1$ limit. By neglecting vibrational contributions to ΔG_v and substituting the value of ΔS_v^{conf} in x_v^{class}, one has that the classical equilibrium concentration of vacancies in a crystal is

$$x_v^{\text{class}} = \exp\left(-\frac{\Delta H_v}{2T}\right). \tag{75}$$

In the case of solid ^{4}He at $T = 0.1$ K, for instance, it follows that $x_v^{\text{class}} \sim 10^{-22}$ when considering $\Delta H_v \sim 10$ K. In fact, such a classical equilibrium concentration of vacancies is so extremely small that in principle it is physically irrelevant.

Interestingly, Rossi *et al.* (2008) and Pessoa, de Koning, and Vitiello (2009a, 2009b) have recently estimated, by using a reversible-work approach that exploits a quantum-classical isomorphism, that the zero-point vacancy concentration in solid ^{4}He is $x_v \sim 10^{-3}$. Actually, this result is many orders of magnitude larger than the classical result obtained with Eq. (75), and it follows from assuming that the crystal is correctly described with a shadow wave function (Vitiello, Runge, and Kalos, 1988; MacFarland *et al.*, 1994). A hypothetical equilibrium vacancy concentration of $\sim 10^{-3}$, although probably still not experimentally detectable, would start being physically relevant to understand the behavior of defective solid ^{4}He. Nevertheless, since Rossi and Vitiello's estimations ultimately rely on a variational model, the large $x_v^{\text{class}} - x_v$ difference cannot be rigorously ascribed to the quantum nature of the crystal alone.

Even when assuming that the equilibrium concentration of vacancies in solid helium is practically null, it cannot be discarded that in the process of growing a crystal from the liquid phase a small concentration of point defects is created. A possible question to answer next then is do vacancies in a quantum crystal cluster or stay dispersed? If vacancies cluster, then they would segregate from the perfect system and become irrelevant. On the contrary, if vacancies remained separated, they could affect the general properties of the quantum crystal quite noticeably (Rota *et al.*, 2012). Unfortunately, there is not a general consensus between theorists about how vacancies interact and distribute in solid ^{4}He. Pollet *et al.* (2008) estimated from thermodynamic arguments that the binding energy of a divacancy is $E_{\text{div}}^{\text{bind}} = 1.4(5)$ K; note that this result is about 2 times larger

than the energy found by Clark and Ceperley (2008) using the PIMC method and a semiempirical pairwise potential. It has been argued then that if vacancies existed they would separate into a vacancy-rich region and segregate from the perfect crystal. Nevertheless, as noted earlier, at finite temperatures it is crucial to also consider the entropic contributions to the Gibbs free energy, which cannot be directly obtained from the simulations. Actually, as shown next, from a configurational entropy point of view it turns out to be energetically much more favorable to have two independent vacancies in the crystal than a bound divacancy state. By completely ignoring vibrational effects, the corresponding entropy gain can be estimated as

$$\delta S^{\mathrm{conf}}_{\mathrm{2v\text{-}div}} \approx 2\,\Delta S^{\mathrm{conf}}_{\mathrm{v}} - \Delta S^{\mathrm{conf}}_{\mathrm{div}} = -\ln(2\,x_{\mathrm{v}}), \tag{76}$$

where the constraint $x_{\mathrm{div}} = x_{\mathrm{v}}/2$ is employed. By considering the temperature and concentration of vacancies employed in the PIMC simulations (Clark and Ceperley, 2008), namely, 0.2 K and $\sim 10^{-2}$, one obtains that $T\,\delta S^{\mathrm{conf}}_{\mathrm{2v\text{-}div}} \sim 1$ K, which actually is of the same order of magnitude than the estimated $E^{\mathrm{bind}}_{\mathrm{div}}$. We note that the same conclusion also holds when considering smaller T's and x_{v}'s. Therefore, an attractive interaction between vacancies does not necessarily imply the existence of vacancy clusters or vacancy segregation at finite temperatures.

An alternative analysis to discern whether ^{4}He vacancies coalescence or not consists of monitoring their spatial correlations in quantum Monte Carlo simulations. For instance, if a multiple-vacancy bound state was to exist then an exponential decay in the corresponding vacancy-vacancy pair-correlation function should appear at separations larger than a specific interaction distance. Following this approach, Lutsyshyn, Cazorla, and Boronat (2010) and Lutsyshyn, Rota, and Boronat (2011) did not find any evidence for the existence of a multiple-vacancy bound state at zero temperature. In particular, at the freezing point and also at higher densities the tail in the vacancy-vacancy pair-correlation function always exhibits an asymptotic plateau. Pessoa, de Koning, and Vitiello (2009b) arrived at a similar conclusion by means of VMC calculations performed with a shadow wave function model. Contrarily, Rossi *et al.* (2010) reported, based on the results of PIGS simulations, that when vacancies are present in large concentrations ($x_{\mathrm{v}} \sim 1\%$) they tend to form bound states.

Note that other possible processes involving vacancies, apart from clustering or dispersing in bulk, have also been suggested; these include nucleation of dislocations (Rossi *et al.*, 2010) and annealing toward the interface regions with the system container (Rossi, Reatto, and Galli, 2012). Rigorous tests of these hypotheses in realistic crystals with first-principles methods, however, appear to be challenging due to the large system size and relaxation-time scales involved in the simulations.

In spite of the ongoing controversy about the possible existence of vacancies in quantum crystals at low T, the effects that hypothetically dispersed vacancies would have on the physical properties of solid helium have already been investigated thoroughly. For instance, the elastic properties of the incommensurate crystal in the limit of zero temperature have been analyzed by Cazorla, Lutsyshyn, and Boronat (2013); it has been shown that when considering large vacancy concentrations ($x_{\mathrm{v}} \sim 1\%$) the shear modulus of the solid undergoes a small reduction of just a few percent with respect to the perfect crystal case.

Based on PIGS simulations and fundamental arguments, Galli and Reatto (2006) demonstrated that BEC occurs in the ground state of incommensurate solid ^{4}He, that is, $n_0 \neq 0$ (see Sec. II.B.1), and that the corresponding critical temperature follows the relation $T_0 \propto x_{\mathrm{v}}^{2/3}$. Recently, Rota and Boronat (2012) corroborated the occurrence of vacancy-induced BEC in solid helium at low temperatures by means of PIMC simulations. It has been shown that below T_0 vacancies become quantum entities that completely delocalize in space; they also found that the dependence of the critical temperature on x_{v} is best represented by a power law with coefficient 1.57 (rather than of 2/3), suggesting that the correlations between vacancies are stronger than previously inferred. Interestingly, recent experiments performed by Benedek *et al.* (2016) appeared to support the possibility of a vacancy-induced BEC scenario in solid helium under nonequilibrium conditions.

B. Dislocations

Since the seminal work of Day and Beamish (2007), there is little doubt that dislocations play a pivotal role in interpreting the mechanical behavior of solid ^{4}He. If in the case of point defects it can be said that theory has led the way to their (partial) understanding, in the case of dislocations it is the other way around. At present, most of what we know about dislocations in quantum solids comes from recent experiments performed by the groups of Beamish, at the University of Alberta, and Balibar, at the Ecole Normale Supérieure de Paris [see, for instance, Haziot, Fefferman, Souris *et al.* (2013), Haziot, Fefferman, Beamish, and Balibar (2013), Fefferman *et al.* (2014), and Souris *et al.* (2014)]. Such a gap between theory and experiments is due to several reasons. First, in order to reliably simulate dislocations, large simulation cells containing at least several thousands of atoms need to be considered (Bulatov and Cai, 2006; Proville, Rodney, and Marinica, 2012); this system size is actually too large to be handled efficiently in quantum simulations. And second, dislocations are complex topological objects that until recently were not studied in depth in the context of low-temperature physics, as a preponderant interest in ground-state properties leads to consider perfect crystals by default. However, as described next, quantum simulation of dislocations is critical for advancing our understanding of quantum crystals.

Dislocations should be created during the growth process of solid helium (e.g., due to thermal contraction of the samples during cooling), as rough estimations of their formation energy amount to several thousands of K and hence they cannot be thermally activated at low T. Consider the classical elastic contribution to the formation energy per unit length of an edge dislocation (Cotterill and Doyama, 1966):

$$E^{\mathrm{elast}}_{\mathrm{disl}}/L = \frac{\mu b^2}{4\pi(1-\nu)} \ln\left(\frac{r_{\mathrm{d}}}{r_{\mathrm{c}}}\right) + E^{\mathrm{elast}}_{\mathrm{core}}, \tag{77}$$

where μ is the shear modulus of the crystal, ν is its Poisson ratio, b is the length of the Burgers vector describing the dislocation, r_d is the dislocation radius, r_c is the dislocation core radius, and $E_{\rm core}^{\rm elast}$ is the elastic energy of the dislocation core. Since we are interested in obtaining an approximate order of magnitude for $E_{\rm disl}^{\rm elast}$, we can neglect the second term in Eq. (77), which is always positive, and assume that $\ln(r_d/r_c) \sim 1$. By adopting the elastic data reported for perfect solid ^{4}He by Pessoa, Vitiello, and de Koning (2010), that is, $\mu = 17.1$ MPa and $\nu = 0.15$, and a usual Burgers vector of modulus $b = a/\sqrt{3} = 2.1$ Å, one obtains that $E_{\rm disl}^{\rm elast}/L \sim 1$ K/Å. Considering now that dislocations in solid ^{4}He typically are several μm long (see Fig. 14), one finally obtains that, at least, $E_{\rm disl}^{\rm elast} \sim 10^4$ K. Note that although this rough estimation for the elastic formation energy of line defects is several orders of magnitude larger than the cost of creating, for instance, a vacancy (see Sec. VI.A), in principle it is not possible to grow ^{4}He crystals free of dislocations with current state-of-the-art synthesis methods (Souris *et al.*, 2015). The apparently inevitable presence of dislocations in solid helium near the zero-temperature limit already poses a problem in the theorist's mind.

In a series of compelling experimental works, Balibar, Beamish, and collaborators characterized the energy, structural, and dynamic properties of dislocations in solid ^{4}He [for a recent review, see Balibar *et al.* (2016)]. The usual experimental setup in those studies consists of a measurement cell supplied with two piezoelectric shear plates that are placed facing each other with a separation of a few millimeters; the narrow gap that is formed between the transducers then is filled with a crystal that is oriented in a particular direction. By applying a voltage to one of the piezoelectric plates a shear strain is induced in the crystal, and the resulting stress is measured by the opposite shear plate. This process is done repeatedly by using alternating currents.

The theory underlying most of Balibar and Beamish's results is that due to Granato and Lücke (1956) in which an analogy is made between the vibration of a dislocation

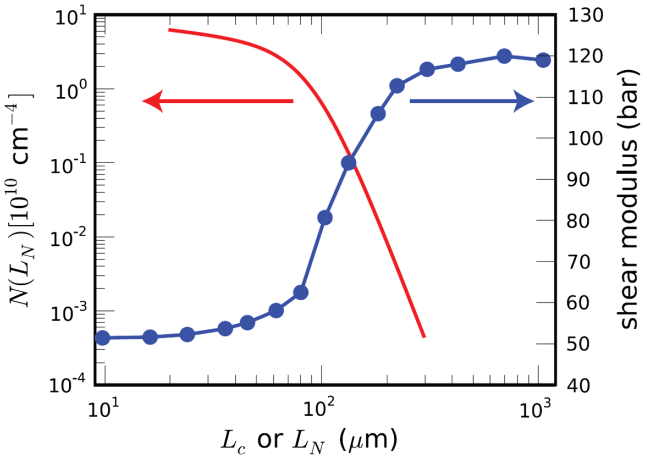

FIG. 14. The measured distribution $N(L_N)$ of lengths L_N between dislocation network nodes in a ^{4}He crystal at $T = 27$ mK; the contribution to the shear modulus from each dislocation length is also indicated. From Fefferman *et al.*, 2014.

pinned down by impurity particles under an alternating stress field and the classical (that is, not quantum mechanical) problem of the forced damped vibration of a string. In Granato and Lücke's classical theory it is assumed that at high temperatures dislocations interact with thermal lattice phonons, and that as a consequence a maximum shear modulus change of

$$\delta_\mu \equiv \frac{\Delta C_{44}}{C_{44}} = \frac{\alpha \Lambda L^2}{1 + \alpha \Lambda L^2} \tag{78}$$

and a dissipation (that is, the phase difference between the applied strain and resulting stress) of

$$\frac{1}{Q} = \delta_\mu B L^2 \omega T^3 \tag{79}$$

occur in the crystal. In the context of solid ^{4}He, "high temperatures" are considered to be $T \geq 0.3$ K (Balibar *et al.*, 2016). In these equations α and B represent two thermal phonon damping parameters [which in solid ^{4}He are equal to 0.019 and 905 s × m^{-2} K^{-3}, respectively (Souris *et al.*, 2015)], Λ is the density of dislocation lines per surface unit, L is a typical length between nodes in the dislocation network, and ω is the frequency of the alternating strain field.

Using Eqs. (78) and (79) and from direct measurements of δ_μ and $1/Q$, Haziot, Fefferman, Souris *et al.* (2013) found that typical values of Λ and L in solid helium are 10^4–10^6 cm^{-2} and 100–230 μm (see Fig. 14), which in the latter case turn out to be macroscopic. In very high quality crystals (Souris *et al.*, 2015), it was observed that dislocations avoid crossing each other by forming two-dimensional arrays of parallel lines called "sub-boundaries," and that they glide together parallel to the basal planes. Remarkably, in the limit of zero temperature the dissipation associated with the gliding of dislocations in the basal plane vanishes (Fefferman *et al.*, 2014), an effect that has been interpreted as evidence of quantum behavior. Nevertheless, whether such an observation implies that the formation energy of dislocation kinks and jogs (that is, defect perturbations that affect the straightness of the dislocation line) also vanishes at ultralow temperatures, or that dislocation kinks and jogs are able to quantum tunnel through small energy barriers, yet needs to be clarified (Kuklov *et al.*, 2014). In this context, the outcomes of quantum simulations could be highly valuable.

At temperatures below 0.2 K, it is found that the dynamics of dislocations is greatly influenced by the presence of isotopic ^{3}He impurities. When the concentration of ^{3}He atoms x_3 is large enough (i.e., $\sim 10^{-7}$ or larger) and T is progressively reduced, the impurities start to bind to the dislocations with an energy that, according to Souris *et al.* (2015) measurements, is of 0.7(0.1) K. At those conditions, the mobility of the dislocations also depends on the frequency of the applied strain. At high frequencies, that is, at high dislocation speeds of > 45 μm/s, the impurities cannot move fast enough to follow the line defects so that they end up anchoring them. However, at lower frequencies, and always considering Souris *et al.* (2015) arguments, dislocations can actually move dressed with ^{3}He atoms.

A pertinent comment needs to be made here. Several nuclear magnetic resonance studies showed that at low temperatures ^{3}He atoms in solid ^{4}He behave as quantum quasiparticles that can move through the lattice at velocities as high as ∼1 mm/s (Allen, Richards, and Schratter, 1982; Kim *et al.*, 2013), that is, significantly faster than 45 μm/s. How is it then possible that impurities end up anchoring dislocations in solid ^{4}He? It has been argued that near the dislocation line the mobility of isotopic impurities could be reduced considerably due to the existing local strain (Balibar *et al.*, 2016); however, there is no quantitative evidence showing that such a large variation of about 3 orders of magnitude in the mobility of ^{3}He impurities could actually be possible. Clearly, a microscopic understanding of what are the interactions between dislocations and quantum isotopic impurities, and the factors that can affect the mobility of the latter, is necessary. The outcomes of quantum simulation studies again could be very useful in clarifying all these issues.

With regard to theory, Boninsegni *et al.* (2007) showed using PIMC simulations that the core of screw dislocations with Burgers vectors oriented perpendicular to the basal plane in solid ^{4}He might be superfluid. Boninsegni *et al.*'s predictions led to a number of hypotheses about possible new phenomena involving quantum dislocations such as, for instance, "superclimb" (Söyler *et al.*, 2009; Aleinikava, Dedits, and Kuklov, 2011) and superfluidity in dislocation networks (Boninsegni *et al.*, 2007). In a recent PIMC study by Landinez-Borda, Cai, and de Koning (2016) on solid helium, it was reported that either screw or edge dislocations with Burgers vectors along the basal plane are not superfluid. In particular, both types of dislocations are predicted to dissociate into nonsuperfluid Shockley partial dislocations separated by ribbons of stacking fault, as it normally occurs in classical hcp crystals (Bulatov and Cai, 2006; Hull and Bacon, 2011). Landinez-Borda, Cai, and de Koning (2016) also concluded that the resistance to flow of partial dislocations in solid helium is negligible (that is, the corresponding Peierls stress is nominally zero) mostly due to zero-point quantum fluctuations. The results presented in this latter simulation work have provided valuable insight into the physical origins of the observed giant plasticity effect (Haziot *et al.*, 2013a, 2013b; Zhou *et al.*, 2013). Apparently, there seems to be some inconsistencies between the conclusions presented by Boninsegni *et al.* (2007) and Landinez-Borda, Cai, and de Koning (2016) as to what concerns the superfluid properties of dislocation cores. Note, however, that the linear defects analyzed in those studies are different as their respective Burgers vectors are either oriented along the *c* axis or contained in the basal plane. Further quantum simulation studies indeed appear to be necessary for clarifying the effect of Burgers vector orientation on the transport properties of dislocations in solid ^{4}He.

Finally, recent experiments done by the Hallock group at the University of Massachusetts showed unexpected mass flow through ^{4}He crystals at low temperatures ($T < 600$ mK) when sandwiched between two regions of superfluid liquid in which a pressure gradient is applied (Ray and Hallock, 2008, 2010; Vekhov and Hallock, 2012). This phenomenon has been dubbed as "giant isochoric compressibility" or the "syringe effect." The observed mass flow was interpreted in terms of two possible scenarios (Hallock, 2015), the climbing (i.e., the passing of an obstacle to start moving again) either of superfluid dislocations (Söyler *et al.*, 2009) or of grain boundaries (Burovski *et al.*, 2005; Sasaki *et al.*, 2006; Pollet *et al.*, 2007; Cheng and Beamish, 2016). Recently, mass flow phenomena have also been observed in an inverted solid-superfluid-solid setup by Cheng *et al.* (2015), in which the effects of ^{3}He impurities concentration and distribution were analyzed in detail. The exact atomistic mechanisms underlying the inverted and direct syringe effects, however, still remain open questions. New systematic experiments and quantum simulation studies certainly are necessary to achieve a more accomplished knowledge of mass transport along quantum linear and planar defects (i.e., dislocations and grain boundaries).

VII. THE ROLE OF DIMENSIONALITY

Quantum crystals at reduced dimensionality have been the focus of numerous experimental and theoretical studies. The interplay between quantum correlations and structural confinement opens a series of interesting new prospects that since the beginning of the quantum Monte Carlo era have been meticulously investigated with theory. The search for novel phases and physical phenomena in quantum gases adsorbed on graphitic and metallic substrates or on the surface of carbon nanostructures and the interior of narrow silica pores represents well-known examples.

A. Quantum films

We focus here on helium and hydrogen since QNE are most pronounced in these species. In very thin films one can expect that two-dimensional effects become dominant, and for this reason many works have concentrated on studying the thermodynamic, structural, and dynamical properties of purely 2D quantum many-body systems.

At zero temperature and zero pressure 2D ^{4}He is a liquid with an estimated equilibrium density of $\sigma_0 = 0.043$ Å^{-2} and binding energy of $E/N = -0.90$ K (Giorgini, Boronat, and Casulleras, 1996). By increasing the density, the liquid solidifies into a triangular lattice (Whitlock, Chester, and Kalos, 1988). The liquid and solid are in equilibrium at densities $\rho_f = 0.068$ Å^{-2} (freezing) and $\rho_m = 0.072$ Å^{-2} (melting), respectively. On the other hand, ^{3}He at low densities remains in the gas phase due to its lower mass, and, more importantly, fermionic character (Grau, Boronat, and Casulleras, 2002). Upon a steady increase in density the gas eventually transforms into a triangular solid, although the critical point associated with this transition has not yet been characterized with precision.

The ground states of two-dimensional molecular hydrogen and deuterium have also been investigated with QMC methods (Boninsegni, 2004; Cazorla and Boronat, 2008c). The primary interest of these studies was to discern whether by reducing the dimensionality it was possible to stabilize the liquid phase. Those theoretical works, however, showed that the fluid is never stable, even when considering negative pressures (Boninsegni, 2004; Cazorla and Boronat, 2008c). In Fig. 15,

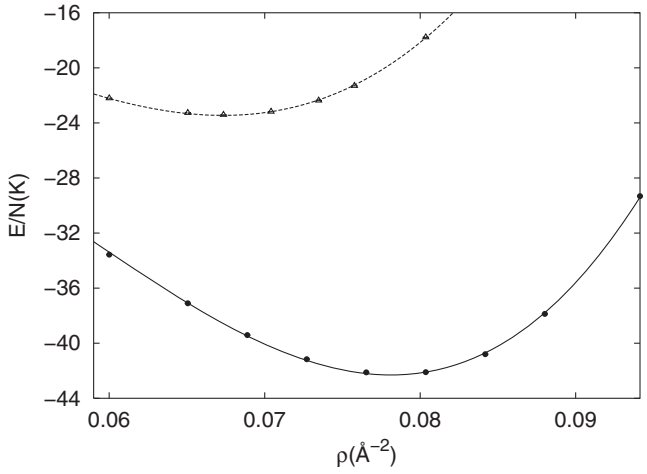

FIG. 15. Energy per particle in two-dimensional solid D_2 (solid line and filled circles) and two-dimensional solid H_2 (dotted line and empty triangles). From Cazorla and Boronat, 2008c.

we enclose the density dependence of the energy calculated in 2D H_2 and D_2 with the DMC method and Silvera-Goldman potential (Cazorla and Boronat, 2008c). At zero pressure, both crystals stabilize in a triangular lattice of density $\sigma_0 = 0.0673$ and 0.0785 Å^{-2}, respectively. The corresponding energies per particle at those conditions are −23.45 K in H_2 and −42.30 K in D_2. This large energy difference indicates that quantum isotopic effects are also significant in two dimensions.

With regard to the possibility of realizing H_2 superfluidity (see Sec. IV.B), several strategies have been explored in reduced dimensionality. It was first proposed by Gordillo and Ceperley (1997) that the intercalation of alkali atoms could frustrate the formation of the solid due to the weaker interaction between impurities and H_2 than between hydrogen molecules. K and Cs were considered as the likely candidates to induce H_2 melting in a PIMC study by Gordillo and Ceperley (1997). Large superfluid fractions of $\rho_s/\rho \sim 0.2$–0.5 were reported in the resulting hydrogen-alkali thin films. However, subsequent quantum simulation studies performed with a larger number of particles found very small values of ρ_s/ρ in equivalent systems (Cazorla and Boronat, 2004; Boninsegni, 2005). More recently, Cazorla and Boronat (2013) predicted by using the DMC method and semiempirical pairwise potentials that frustration of 2D solid H_2 could be achieved with sodium atoms arranged in a triangular lattice of constant 10 Å. The main reason for this is that the forces between Na atoms and hydrogen molecules are weaker than those considered in previous studies, hence a significant reduction of the equilibrium density is induced that favors stabilization of the liquid phase. Note, however, that in a subsequent PIMC study by Boninsegni (2016) this conclusion was disputed by arguing that the system remains in the solid phase independently of density and the type of alkali impurity that is considered.

Experimental realization of quasi-two-dimensional quantum solids is achieved through adsorption of quantum gases on attractive substrates. In this context, one of the most extensively investigated substrates is graphite. The physics of gas-adsorption phenomena in graphite is very rich (Bruch, Cole, and Zaremba, 1997) as a large sequence of transitions have been experimentally observed and described with microscopic theory (Clements *et al.*, 1993; Clements, Krotscheck, and Saarela, 1997). We concentrate here on describing the properties of the first adsorbed layer and other related phases. Note that when corrugation effects are considered in the calculations (that is, the spatial distribution of carbon atoms in the underlying substrate is explicitly simulated), one normally obtains denser commensurate phases.

According to recent quantum simulation studies performed with semiempirical pairwise potentials, the ground state of ^{4}He adsorbed on graphite (and graphene) is a $\sqrt{3} \times \sqrt{3}$ commensurate phase with a surface density of 0.0636 Å^{-2} (Gordillo, Cazorla, and Boronat, 2011). The liquid phase is metastable with respect to the crystal. As the density is increased, the commensurate crystal transforms into a triangular incommensurate solid of density ∼0.08 Å^{-2} (Pierce and Manousakis, 2000; Corboz *et al.*, 2008; Gordillo and Boronat, 2009b). This description is in excellent agreement with the available experimental data (Bruch, Cole, and Zaremba, 1997). By further increasing the density, a second layer develops on top of the first with an equilibrium density of 0.12 Å^{-2}.

Recent QMC studies of the registered phases of H_2 adsorbed on graphite and graphene provide a description that is identical to that obtained for ^{4}He and which is in good agreement with the experiments (Gordillo and Boronat, 2010). In particular, the ground state is a commensurate $\sqrt{3} \times \sqrt{3}$ phase that undergoes a first-order transition toward an incommensurate triangular crystal at $\rho = 0.077$ Å^{-2}. The phase diagram of D_2 on graphite has been thoroughly investigated in experiments (Bruch, Cole, and Zaremba, 1997) but not yet with theory. It is known that this is richer than its H_2 counterpart since at least two additional commensurate phases appear in the first adsorbed layer: the ε phase, which is a 4×4 structure (0.0835 Å^{-2}), and the δ one, corresponding to a $5\sqrt{3} \times 5\sqrt{3}$ lattice (0.0789 Å^{-2}). According to DMC calculations on H_2 none of these latter commensurate phases are stable (Gordillo and Boronat, 2010).

B. One-dimensional systems

Carbon nanotubes and nanopores embedded in solid matrices have opened the possibility of studying quantum systems in quasi-one-dimensional geometries (Calbi *et al.*, 2001). Investigating individual carbon nanotubes, however, has proved challenging due to the fact that they are normally capped and adsorption of atoms on their interior is energetically unfavored. Meanwhile, adsorption on the intersites and grooves formed between adjacent nanotubes have been observed. A topic of interest in these systems is the study of the crossover between three-dimensional and one-dimensional physics (Gordillo and Boronat, 2009a). For instance, changes on the superfluid fraction and condensate fraction of liquid ^{4}He upon variation of the nanopore radius have been systematically studied by Vranješ Markić and Glyde (2015) with PIMC simulations.

Strictly one-dimensional quantum systems possess unique features as compared to all other low-dimensional systems.

One of the most relevant aspects is that the presence of a hard core in the interatomic interactions makes the quantum statistics irrelevant. This means that simulation of fermionic systems (e.g., ^{3}He) can be made exactly because the nodes of the corresponding wave function are known *a priori* and hence one can get rid of the sign problem in practice (see Sec. III.A.2). Another important characteristic is the absence of continuous phase transitions (i.e., as described by Landau's theory), although the limiting $T = 0$ case may be an exception. Finally, if the excitation spectrum of the system is gapless, i.e., $E_k = \hbar|k|c$, Luttinger theory applies and consequently the behavior of correlation functions at large distance (or small momenta) is known analytically (Giamarchi, 2004; Imambekov, Schmidt, and Glazman, 2012). In this latter case, the behavior of the system is universal in terms of the Luttinger parameter K, which in a homogeneous system is directly related to the Fermi velocity v_F and speed of sound c as $K = v_F/c$. The Fermi velocity v_F is completely fixed by the linear density ρ, whereas the speed of sound c depends on the many-body interactions.

In Luttinger's theory, the height of the lth peak in the static structure factor $S(k)$ is given by (Haldane, 1981)

$$S(k = 2lk_F) = A_l N^{1-2l^2K}, \tag{80}$$

which diverges when $K < 1/2l^2$. If the first peak in $S(k)$ diverges, that is, $K < 1/2$, the system is called a "quasicrystal." There is a number of important differences between a quasicrystal and real crystals. A three-dimensional crystal possesses diagonal long-range order since the density oscillations in the two-body distribution function remain in phase over long distances. In one dimension, on the contrary, that order is lost according to a power-law decay. The height of the first peak diverges in both cases; however, in a true crystal the Bragg peak grows linearly with the number of particles $S(k_{\text{peak}}) \propto N$, whereas in a quasicrystal the corresponding exponent is smaller than unity [see Eq. (80)].

QMC calculations of 1D ^{4}He at equilibrium showed that this is a self-bound system with a tiny binding energy of ~ -4 mK (Boninsegni and Moroni, 2000; Gordillo, Boronat, and Casulleras, 2000a). When the density is increased, the system eventually becomes a quasicrystal. Recently, the ground state of one-dimensional ^{3}He has been thoroughly studied with the DMC method (Astrakharchik and Boronat, 2014). The lower mass of the isotope makes the system non-self-bound, and thus it remains in the gas phase down to zero pressure. Through calculation of the corresponding Luttinger parameter one can appreciate the richness of its behavior as a function of density (see Fig. 16).

As the interaction between hydrogen molecules is more attractive than between helium atoms, H_2 is also self-bound in the one-dimensional limit. When H_2 molecules, or helium atoms, are adsorbed inside a nanopore the resulting phases strongly depend on the amount of space that is available. In very narrow nanotubes, for instance, one observes the existence of real quasi-1D systems, that is, in the Luttinger sense (Gordillo and Boronat, 2009a). On the contrary, if the nanopore diameter is wide enough, particles migrate toward the nanopore walls due to the strong attractive interactions with them. Eventually if the nanopore interior is further enlarged, nucleation of a narrow channel containing a liquid may occur (Rossi, Galli, and Reatto, 2005). In the case of molecular hydrogen, however, the possible stabilization of a 1D fluid remains controversial (Gordillo, Boronat, and Casulleras, 2000b; Boninsegni, 2013b; Omiyinka and Boninsegni, 2016; Rossi and Ancilotto, 2016).

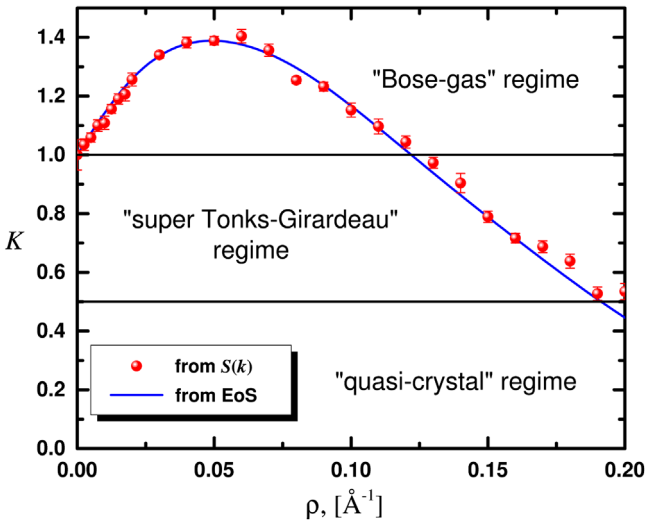

FIG. 16. Luttinger parameter K in one-dimensional ^{3}He expressed as a function of the linear density ρ. The corresponding speed of sound, as extracted from the phononic part of the static structure factor (symbols) and thermodynamic compressibility (line), is also shown. Adapted from Astrakharchik and Boronat, 2014.

Recently, the adsorption of quantum gases on the external surface of a single nanotube has drawn some attention. State-of-the-art resonance experiments on a single suspended carbon nanotube have been able to determine the phase diagram of the deposited rare gases with high precision (Wang *et al.*, 2010; Tavernarakis *et al.*, 2014). For instance, in the $T = 0$ limit one can identify either a registered $\sqrt{3} \times \sqrt{3}$ phase, already known from adsorption on planar substrates, or incommensurate phases, depending on the chemical species. Theoretical predictions on these systems (Gordillo and Boronat, 2011) agree well with the experimental findings.

C. Clusters

Helium and hydrogen drops can be generated in the laboratory by means of free jet expansions from a stagnation source chamber that go through a thin walled nozzle (Grebenev, Toennies, and Vilesov, 1998). Helium drops are the most clean example of inhomogeneous quantum liquids with either boson (^{4}He) or fermion (^{3}He) quantum statistics. In recent years, the relevance of He drops has been reinforced by the increasing interest in studying the behavior of small molecules placed in their interior. In fact, quantum clusters can act as ideal matrices in which to carry out an accurate spectroscopy analysis of the embedded molecules. When the guest molecule is surrounded by ^{4}He atoms, the corresponding rotational spectrum presents a peaked structure that has been attributed to the superfluid nature of helium. By contrast,

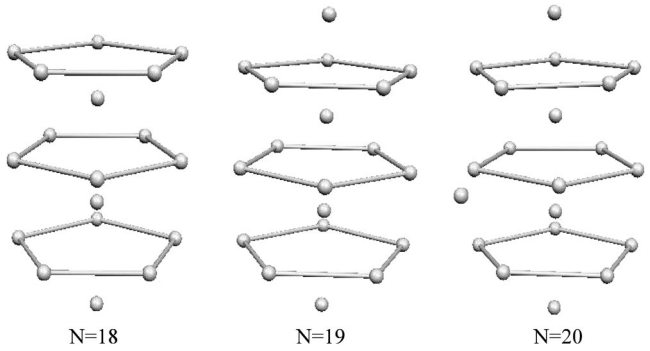

FIG. 17. Optimal distribution of equilibrium sites in solid H_2 clusters with $N = 18$, 19, and 20 molecules at zero temperature. From Sola and Boronat, 2011.

in ^{3}He drops a broad peak is recorded. This phenomenon, termed microscopic superfluidity, has been the object of many QMC studies in recent years (Sindzingre, Klein, and Ceperley, 1989; Sola, Casulleras, and Boronat, 2006).

H_2 clusters have also been produced in the laboratory with jet expansion techniques (Tejeda *et al.*, 2004). The behavior of H_2 drops is richer than that of ^{4}He since they can be either liquid or solid depending on the number of constituent particles. The first PIMC study on H_2 clusters was carried out by Sindzingre, Ceperley, and Klein (1991), and it was found that clusters comprising a number of molecules up to $N \simeq 18$ were superfluid at temperatures below $T = 2$ K. In a subsequent PIMC work (Khairallah *et al.*, 2007) the limiting number of molecules exhibiting superfluid behavior was raised to $N \simeq 26$. The results reported by Khairallah *et al.* (2007) appear to show that superfluidity is mostly localized in the surface of the cluster, which suggests an inhomogeneous structure formed by a solid core surrounded by a liquid *skin*. This interpretation, however, has been challenged in a later PIMC work in which it was argued that, in spite of the local variation in molecular order, superfluidity remains a global property of the entire cluster (Mezzacapo and Boninsegni, 2008).

The structure and energy of small H_2 clusters in the limit of zero temperature have been studied accurately with the DMC (Guardiola and Navarro, 2008) and PIGS (Cuervo and Roy, 2006) methods. The presence of magic-cluster sizes, identified with a kink in the chemical potential, was reported in those studies. The number of molecules contained in the smallest and energetically most stable clusters appears to coincide with the results of Raman spectroscopy measurements (Tejeda *et al.*, 2004). A combination of the DMC and stochastic optimization (i.e., simulated annealing) techniques has allowed one to determine the equilibrium structure in most stable solid H_2 clusters (Sola and Boronat, 2011). Examples of optimal molecular arrangements obtained in those clusters are shown in Fig. 17.

VIII. MOLECULAR CRYSTALS

Molecular systems are of critical importance in astronomy, biology, and environmental science. Hydrogen is the most abundant element in the Universe and over wide thermodynamic conditions is most stable in molecular form (see Sec. IV.B). Water is vital to all known forms of life and it covers around three-fourths of the Earth's surface. Nitrogen and methane are found in the interior and crust of many celestial bodies and also in organic substances. When all these species are compressed eventually they become crystals in which, due to the light weight of their atoms and weak interparticle interactions, QNE play a pivotal role at low temperatures (see Fig. 1). Next, we briefly review the knowledge of the phase diagram of these compounds and highlight the aspects that remain contentious. Because of their intrinsically rich and complex nature, it is not possible to provide a detailed description of H_2, H_2O, N_2, and CH_4; hence we refer the interested reader to other recent and more specialized articles [see, for instance, McMahon *et al.* (2012), Goncharov, Howie, and Gregoryanz (2013), and Herrero and Ramírez (2014)]. For the sake of focus, only those aspects related to the crystalline phases are considered in this section.

A. H_2 at extreme $P-T$ conditions

Because of its low-Z number, hydrogen's x-ray scattering cross section is very low. This means that it is extremely challenging to determine with accuracy its atomic structure under extreme thermodynamic conditions in the laboratory. Infrared (IR) and Raman spectroscopy techniques were used to monitor the changes in the vibrational properties of the crystal that can be ascribed to a phase transition. However, due to the high reactivity, mobility, and diffusion of the molecules already at moderate temperatures (i.e., ≥ 250 K), this type of measurement turns out to be very difficult (Goncharov, Howie, and Gregoryanz, 2013). Here is where the inputs of theory and computer simulations become critical. By comparing the vibrational phonon spectra of low-energy structures obtained in first-principles searches with experimental data, candidate atomic structures can be identified for each of the detected transformations. Unfortunately, for the reasons highlighted in Sec. I.D, the theoretical study of hot and dense solid hydrogen is technically difficult and very sensitive to the employed method (that is, the free-energy differences between phases normally are very small, of the order of a few meV, which coincide with the typical accuracy threshold in first-principles calculations). As a consequence, the description of hydrogen-based systems obtained with different theories may differ (Morales *et al.*, 2013; Drummond *et al.*, 2015), further complicating the characterization of solid hydrogen.

The H_2 crystal phases that are experimentally well established are denoted by I, II, III, and IV (see Fig. 18). Phase I corresponds to the close-packed hcp structure, in which para-H_2 molecules have zero angular momentum and spherically symmetric wave functions (Silvera, 1980). At low temperatures and as pressure is increased, breaking of rotational symmetry eventually occurs and the crystal stabilizes in phase II (Lorenzana, Silvera, and Goettel, 1990); the boundary between phases I and II is strongly dependent on the isotope type (see Fig. 18), which indicates the presence of important QNE. Around 150 GPa, molecular hydrogen undergoes another phase transformation into phase III (Hemley and Mao, 1988; Lorenzana, Silvera, and Goettel, 1989), which has been shown to extend up to pressures of ~300 GPa and

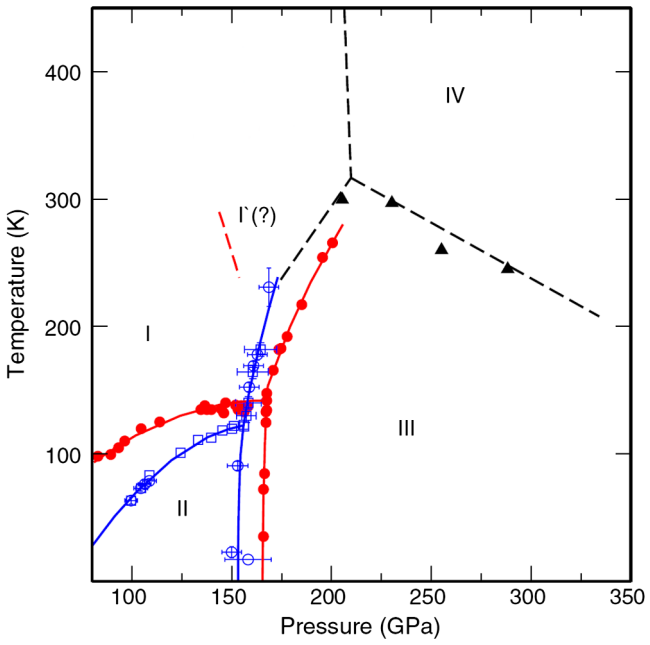

FIG. 18. High-P phase diagram of solid molecular hydrogen and deuterium. Open and filled circles are Raman measurements for hydrogen and deuterium, respectively, and open squares are IR data for the hydrogen (Goncharov, Hemley, and Mao, 2011). Triangles and the dashed lines indicate inferred boundaries for the recently proposed phase IV (Howie, Guillaume *et al.*, 2012). The dashed line and the existence of phase I′ are still matters of debate (see text). From McMahon *et al.*, 2012.

temperatures of ∼300 K (Zha, Liu, and Hemley, 2012). Experiments have also been able to provide constraints on the molecular orientation in phases II and III but, due to the reasons already specified, not complete structural characterizations (Goncharov *et al.*, 1998).

There have been many attempts to identify the structures of phases II and III with theoretical methods. Because of the technical difficulties encountered in the treatment of weak dispersive intermolecular interactions and the indispensable consideration of QNE, however, there is not yet general agreement on this matter. For phase II, there is a number of candidate structures including the orthorhombic $Cmc2_1$ (Kitamura *et al.*, 2000), monoclinic $P2_1/c$ (Zhang *et al.*, 2007), and orthorhombic $Pca2_1$ (Kohanoff *et al.*, 1997; Städele and Martin, 2000). From all these structures, $Pca2_1$ emerges as one of the most likely molecular models (Moraldi, 2009; McMahon *et al.*, 2012). Experiments, however, indicate that phase II possesses only one high-frequency Raman vibrational mode whereas the $Pca2_1$ phase has four (Cui, Chen, and Silvera, 1995). More recently, a new monoclinic $P2_1/c$ phase containing 24 atoms in the primitive cell has been proposed also as a likely candidate for phase II (Pickard and Needs, 2009). This structure has been obtained through the *ab initio* random structure searching method (Pickard and Needs, 2006) and its vibrational phonon features appear to be consistent with the Raman experiments (Drummond *et al.*, 2015).

With regard to phase III, it was initially proposed that a hcp lattice with molecules tilted roughly 60° with respect to the c axis could be a strong candidate (Natoli, Martin, and Ceperley, 1995). This suggestion is consistent with the reported spectroscopy data, in which intense IR activity is appreciated (Cui, Chen, and Silvera, 1995), and with a recent x-ray diffraction study by Akahama *et al.* (2010). Subsequently, Pickard and Needs (2007) proposed, again by relying on the outcomes of DFT-based random structure searches, a different candidate structure consisting of 12 molecules per unit cell with the centers close to those in a distorted hcp lattice. The symmetry of this phase is $C2/c$ (monoclinic) and its vibrational phonon features are consistent with the available experimental data as well. More recently, a hexagonal structure with $P6_122$ symmetry has been introduced as another possible candidate for phase III at pressures $\lesssim$200 GPa (Monserrat *et al.*, 2016). The vibrational properties of this new phase are also consistent with the available Raman and infrared experimental data; however, it appears to provide better agreement than the monoclinic $C2/c$ phase with the x-ray diffraction data obtained by Akahama *et al.* (2010) at moderately high pressures.

In 1995, Goncharov *et al.* found in deuterium a small discontinuity in the vibron mode (that is, the intramolecular stretching mode) and a change in the slope of the corresponding I-III phase boundary at pressures around 150 GPa and temperatures above 175 K. This small vibron discontinuity practically disappeared at $T \geq 250$ K. These observations suggest the possible existence of a new phase denoted by I′ (see Fig. 18) that is isostructural to phase III, and of a critical I-I′-III point. PIMC calculations by Surh *et al.* (1997) on a system of quantum rotors interacting through an effective LDA model provide some support to this hypothesis. In subsequent spectroscopy experiments, Baer, Evans, and Yoo (2007) found vibron signatures that are also consistent with the existence of phase I′. However, for these latter observations to be consistent with those by Goncharov *et al.* (1995), the slope of the I-I′ phase boundary needs to be negative, a feature that was not reported in the earliest work. In a more recent study Goncharov, Hemley, and Mao (2011) performed a refined vibrational spectroscopy analysis and concluded that the new data do not support the existence of phase I′. Further systematic investigations appear to be necessary to clarify these issues.

Recently, room-temperature static diamond-anvil-cell (DAC) experiments have been performed in which pressures of up to 300 GPa have been reached (Eremets and Trojan, 2011; Howie, Scheler *et al.*, 2012; Howie, Guillaume *et al.*, 2012; Loubeyre, Occelli, and Dumas, 2013). Eremets and Trojan (2011) reported that solid hydrogen becomes metallic at a pressure of 265 GPa. Subsequent experimental studies (Howie, Scheler *et al.*, 2012; Howie, Guillaume *et al.*, 2012; Loubeyre, Occelli, and Dumas, 2013), however, do not appear to support the validity of this result. The pressure threshold for the insulator to metal transition in hydrogen still is believed to lie between 325 (Goncharov *et al.*, 2001) and 450 GPa (Loubeyre, Occelli, and LeToullec, 2002). Such recent room-temperature DAC studies, on the other hand, all agree that hydrogen transforms to a new phase, denoted by IV (see Fig. 18), at a pressure near 220 GPa. During the III-IV transformation, a large vibron Raman frequency discontinuity and the appearance of two IR and two Raman vibron modes

are observed. The existence of phase IV, therefore, now is regarded as well established.

Again, several candidate structures have been proposed for phase IV. Howie, Scheler *et al.* (2012) and Howie, Guillaume *et al.* (2012) tentatively indexed it as $Pbcn$, based on the results of the DFT-based random structure searches carried out by Pickard and Needs (2007) and their experimental spectroscopy analysis. This new orthorhombic structure presents a quite peculiar molecular arrangement in which consecutive graphenelike layers alternate between ordered and disordered structures. Chiefly, proton tunneling occurs within the graphenelike disordered layers and the corresponding frequency increases under pressure (Howie, Scheler *et al.*, 2012). Pickard, Martinez-Canales, and Needs (2012), however, showed by using DFT-based methods that the $Pbcn$ phase is vibrationally unstable at zero temperature. They proposed a monoclinic Pc structure to represent phase IV. This monoclinic phase is dynamically stable and contains 48 atoms in its unit cell; it consists of alternating layers of weakly coupled molecules with short intramolecular bonds, and strongly coupled molecules forming graphenelike sheets with long intramolecular bonds. Recent synchrotron infrared measurements by Loubeyre, Occelli, and Dumas (2013) appear to support the validity of this structural layered model. By relying also on the results of first-principles simulations, Liu *et al.* (2012) proposed a monoclinic Cc structure as a new possible candidate for phase IV; this phase is vibrationally stable and structurally very similar to the Pc structure proposed by Pickard, Martinez-Canales, and Needs (2012), although it is thermodynamically less stable and has no orientational order. Further systematic investigations appear to be necessary to determine with precision the molecular structure of phase IV.

Several other phases have been predicted to exist in solid hydrogen at low temperatures and pressures beyond 250 GPa. Most of those phases have been predicted based on the results of first-principles crystal structure searches that incorporate QNE through the quasiharmonic approximation (see Sec. II.A.1). Pickard, Martinez-Canales, and Needs (2012) proposed that their candidate structure for phase III, that is, monoclinic $C2/c$, transforms into an orthorhombic $Cmca-12$ phase containing 12 atoms per unit cell at $P=285$ GPa, and that this subsequently transforms into another $Cmca-4$ phase with a smaller number of atoms per unit cell at $P=385$ GPa. Liu, Wang, and Ma (2012) also predicted that at pressures higher than ∼500 GPa hydrogen transforms into a new monoclinic $C2/c$ phase that possesses two types of intramolecular bonds with different lengths. In fact, new crystal phases (e.g., IV′ and V) have been observed in DAC experiments performed at pressures beyond ∼300 GPa (Howie, Scheler *et al.*, 2012; Dalladay-Simpson, Howie, and Gregoryanz, 2016); however, their precise molecular arrangements still remain unknown.

The possibility of stabilizing an atomic, rather than a molecular, phase in solid hydrogen by means of pressure has also been explored with theory. This possibility is very interesting from a fundamental point of view as it could render a metallic system (Wigner and Huntington, 1935). Considering the orthorhombic $Cmca-12$ phase originally proposed by Pickard and Needs (2007) and relying on *ab initio* random structure searches, McMahon and Ceperley (2011) proposed that molecular hydrogen dissociates into a monoatomic body-centered tetragonal structure near 500 GPa. Labet *et al.* (2012) and Labet, Hoffmann, and Ashcroft (2012a, 2012b, 2012c) also analyzed in detail the process of molecular dissociation by focusing on the structures predicted by Pickard and Needs (2007); they found a discontinuous shift in the distances between protons when transitioning from the orthorhombic $Cmca-12$ to the atomic phase and proposed an intermediate phase that would allow for a continuous dissociation. More recently, Azadi *et al.* (2014) concluded, based on electronic QMC methods (see Sec. III.A.2) and considering nuclear anharmonic contributions to the enthalpy through DFT, that a transition from the orthorhombic $Cmca-12$ to an atomic $I4_1/amd$ phase [previously introduced by Pickard and Needs (2007)] could occur at $P=374$ GPa. Interestingly, Dalladay-Simpson, Howie, and Gregoryanz (2016) reported experimental evidence for a new phase in hydrogen, denoted by V, which at room temperature is stabilized at a pressure of 325 GPa. The experimental evidence consists of a substantial weakening of the vibrational Raman activity, a change in the pressure dependence of the vibron, and a partial loss of the low-frequency excitations. The exact crystalline structure of this new phase still is not well established.

As explained in this section, many complex and controversial aspects still need to be solved in solid hydrogen under extreme thermodynamic conditions. On the theoretical side, most of the predictions on phases II, III, and IV rely on techniques that incorporate QNE only approximately (e.g., quasiharmonic approaches) and on standard DFT methods. Using such approaches to reproduce the thermodynamic stability of highly compressed hydrogen, however, seems to be inadequate. For instance, Chen *et al.* (2014) recently showed in a thorough PIMC benchmark study on H_2 that those cases in which good agreement between standard DFT calculations and experiments is obtained, large error cancellations are likely to be affecting the simulation results. Similar conclusions have also been attained by Geneste *et al.* (2012), Morales *et al.* (2013), and Drummond *et al.* (2015) by using nonstandard computational approaches (e.g., nonharmonic simulation methods in combination with the electronic QMC method). In order to provide more conclusive estimations in solid H_2, therefore, it is necessary to employ quantum simulation methods that simultaneously describe QNE (e.g., PIMD, PIMC and PIGS methods, see Sec. II) and long-range intermolecular forces (e.g., nonstandard DFT functionals and the eQMC method, see Sec. III) accurately.

B. Solid water

QNE are unquestionably important for understanding the physical properties of ice. Because of the small moment of inertia of the H_2O molecule and relatively low strength of the intermolecular hydrogen bonds, QNE persist in ice up to temperatures of ∼100 K (Gai, Schenter, and Garrett, 1996a; Ceriotti, Bussi, and Parrinello, 2009; Vega *et al.*, 2010; Moreira and de Koning, 2015). Numerous examples of these effects can be found in the literature. For example, incoherent single-particle tunneling has been disclosed in cubic ice at Mbar pressures, explaining the origins of the measured H/D

isotopic effects on the antiferroelectric ice VIII → paraelectric VII phase transformation (Benoit, Marx, and Parrinello, 1998; Benoit, Romero, and Marx, 2002). A recent neutron scattering study has also revealed an anomalous T-dependent dynamic effect in normal (hexagonal) ice I_h (Bove *et al.*, 2009) that has been explained in terms of collective tunneling of protons (up to six) within locally ordered rings (Drechsel-Grau and Marx, 2014). These findings suggest that quantum many-body tunneling could also be important in a variety of related H-bonded systems, including other phases of ice and cyclic water clusters on metal surfaces (Drechsel-Grau and Marx, 2014).

In analogy to solid helium and hydrogen, an interest has developed in understanding the features of the momentum distribution of ice. Both inelastic neutron scattering experiments (Reiter *et al.*, 2004; Flammini *et al.*, 2012) and advanced path-integral calculations (Morrone and Car, 2008; Lin *et al.*, 2010, 2011) agree in describing the corresponding $n(\mathbf{k})$ with an anisotropic Gaussian. This implies that protons experience an anisotropic quasiharmonic effective potential with distinct principal frequencies, which reflects the possible molecular orientation. According to both neutron scattering experiments and path-integral calculations (Flammini *et al.*, 2012) the excess kinetic energy in ice I_h at low temperatures amounts to ∼150 meV, which evidences a marked quantum character (see Sec. I.C).

The presence of quantum isotopic effects is also notable in solid water. The effects of hydrogen isotope substitution on the structural, kinetic energy, and atomic delocalization properties of ice have been investigated in detail with experiments and path-integral calculations. For example, quantum simulations of D_2O in the I_h phase at $T = 100$ K have found a decrease in the crystal volume and intramolecular O-D distance of 0.6% and 0.4%, respectively, as compared to H_2O (Herrero and Ramírez, 2011a). An increase of ∼6% in the melting temperature of D_2O at ambient pressure has also been predicted with path-integral simulations (Ramírez and Herrero, 2010). Similarly, the presence of quantum isotopic effects in highly compressed amorphous ice has been reported by several groups (Gai, Schenter, and Garrett, 1996b; Herrero and Ramírez, 2012). Interestingly, an anomalous thermal expansion isotopic effect has been observed in ice; the volume of solid D_2O is larger than that of solid H_2O (Röttger *et al.*, 1994), in contrast to what occurs in other crystals upon substitution with heavier species. This quantum nuclear effect has been rationalized recently by Pamuk *et al.* (2012) with *ab initio* calculations based on the quasiharmonic approximation.

The importance of QNE on the phase diagram of ice has been determined quantitatively with path-integral Monte Carlo simulations based on the TIP4PQ/2005 force field by McBride *et al.* (2012) (see Fig. 19). It is worth noting that although the intermolecular potential model employed by McBride *et al.* (2012) is nonflexible and nonpolarizable, the agreement obtained with the experiments is fairly good. In particular, quantum simulations provide phase boundaries that are shifted ∼20 K toward lower temperatures as compared to the observations [see Fig. 3 in McBride *et al.* (2012)]. As shown in Fig. 19, QNE play a significant role in the thermodynamic stability of the different phases of ice: the melting lines are shifted toward higher temperatures and

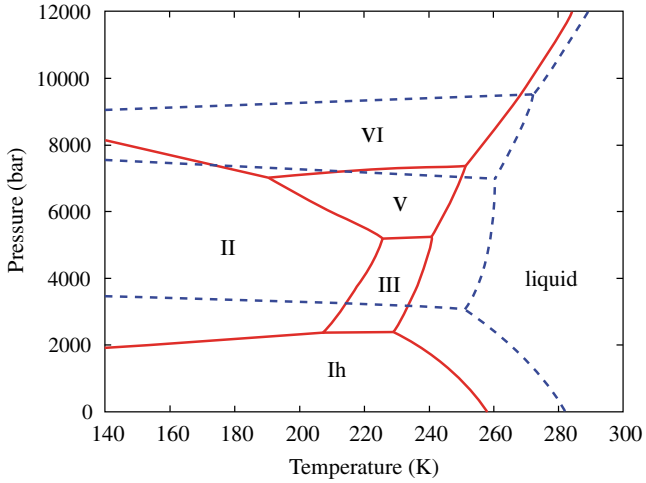

FIG. 19. The classical phase diagram of water based on the TIP4PQ/2005 force field (dashed blue lines) as compared to the quantum phase diagram obtained with path-integral simulations (solid red lines). Roman numerals label different crystal structures with hexagonal symmetry (I_h), rhombohedral (II), tetragonal (III and IV), and monoclinic (V). Adapted from McBride *et al.*, 2012.

the solid-solid transitions toward higher pressures. Another important difference is that the region of thermodynamic stability of phase II is significantly reduced in the classical phase diagram, as this phase appears only at temperatures below 80 K therein (that is, in the classical phase diagram of Fig. 19 phase II is missing). The origins of these quantum effects have been rationalized in terms of the tetrahedral angular order ascribed to each polymorph and the volume change involved in the phase transformations. The pressure dependence of the crystal volume, bulk modulus, interatomic distances, atomic delocalization, and kinetic energy in hexagonal ice (I_h) under pressure have also been thoroughly analyzed with similar computational techniques by Herrero and Ramírez (2011b).

Despite the mounting experimental and theoretical evidence showing the importance of QNE, these effects are normally disregarded in most computational studies of water and ice at $T \neq 0$ conditions. This is due in part to the difficulties encountered in the description of molecular interactions in H_2O. Different types of computationally inexpensive empirical potentials, which assume either rigid or flexible molecules and polarizable or nonpolarizable ions (e.g., the so-called SCP, TIP4P, q-TIP4P/F, and TIP4PQ/2005 force fields), have been employed in most simulation studies of ice at finite temperatures. Some of those force fields have been fitted to reproduce experimental data to be used subsequently in classical simulation studies; hence they already effectively incorporate QNE. Quantum calculations based on those interaction models, therefore, may provide in some cases worse agreement with the experiments than classical simulation studies due to double counting of quantum nuclear effects (Herrero and Ramírez, 2014). In other words, the inaccurracies affecting common empirical interaction models may disguise to some extent the real influence of QNE by providing reasonably good agreement with the

experiments. In some cases it has actually been demonstrated that the combined description of molecular interactions and ionic effects at the quantum level is necessary for correctly reproducing the experimental findings in ice. Examples include the anomalous volume expansion observed in ice isotopes (Pamuk *et al.*, 2012) and the interpretation of measured x-ray absorption spectra (Kong, Wu, and Car, 2012; Kang *et al.*, 2013).

Ab initio treatment of the molecular interactions in ice has been done mostly with DFT methods. However, the presence of hydrogen bonds and dispersive long-range forces makes the description of this crystal difficult, demanding the use of computational methods going beyond standard DFT (see Sec. III.A.1). For a detailed description of the strengths and weaknesses of different exchange-correlation DFT approximations in describing H_2O-based systems, see Morales *et al.* (2014) and Gillan, Alfè, and Michaelides (2016). Note that the application of electronic quantum Monte Carlo methods to the study of bulk ice is very rare (Santra *et al.*, 2011), mainly due to computational affordability issues and the likely bias associated with the use of pseudopotentials (Driver and Militzer, 2012).

An advantageous aspect in the simulation of ice, as compared to that of solid helium or hydrogen, is that QNE in principle can be correctly described with the QHA; see Sec. II.A.1. This conclusion has been attained based on comparisons provided between *ab initio* QHA results and neutron scattering experiments [see, for instance, Senesi *et al.* (2013)] and, more convincingly, between QHA and path-integral simulations performed with the same effective interaction model (Pamuk *et al.*, 2012; Ramírez *et al.*, 2012). Consequently, the study of the low-temperature phase diagram and thermodynamic properties of H_2O in principle is affordable with first-principles methods. Nevertheless, a note of caution must be added here. Recently, Engel, Monserrat, and Needs (2015) showed in a DFT-based study that anharmonic contributions to the free energy can turn out to be decisive for correctly describing the thermodynamic stability of different ice polymorphs with very close quasiharmonic free energies. In particular, it was shown that anharmonic quantum nuclear effects are decisive in stabilizing the hexagonal I_h phase with respect to cubic I_c, the latter being a form of ice presenting stacking of layers with tetrahedrally coordinated water molecules [the so-called "stacking disordered ice," see also Engel, Monserrat, and Needs (2016)]. As noted by the authors of that study, treatment of anharmonicity in general could be crucial for correctly describing the energy differences between similar polymorphs in hydrogen-bonded molecular crystals (which can be relevant, for instance, to the pharmaceutical sciences).

C. Nitrogen and methane

QNE are more pronounced in molecular nitrogen (N_2) and methane (CH_4) than in H_2O (see Fig. 1). This is due to the fact that the intermolecular interactions in the two former systems are dominated by long-range dipole-dipole (CH_4), dipole-quadrupole (CH_4), and quadrupole-quadrupole (N_2 and CH_4) forces, which are weaker than hydrogen bonds (Cazorla, 2015). Certainly, under normal thermodynamic conditions H_2O is a liquid whereas N_2 and CH_4 are gases. However, the study of QNE in solid nitrogen and methane is marginal in comparison to that in ice (or hydrogen). Improving our quantitative understanding of solid N_2 and CH_4 is actually important for planetary and energy materials sciences. For example, these species are believed to abound in the surface and interior of Uranus, Neptune, and Pluto (Hubbard *et al.*, 1991; Protopapa *et al.*, 2008). Meanwhile, under high pressures (≥ 110 GPa) molecular nitrogen dissociates into singly bonded polymeric nitrogen, the so-called cubic gauge phase, that is being considered as a potential high-energy-density material due to its likely metastability at ambient pressure (Eremets *et al.*, 2004).

The $P-T$ phase diagrams of compressed nitrogen and methane are very complex, which is the case for most molecular systems due to the prominence of the orientational degrees of freedom. N_2 exhibits five solid molecular phases at pressures below $\sim$10 GPa and temperatures $T \leq 300$ K (Gregoryanz *et al.*, 2007; Tomasino *et al.*, 2014). The low-temperature phases in molecular nitrogen are governed by quadrupole-quadrupole interactions and in moving from zero to higher pressures the crystal first transforms from an orientationally disordered cubic (α) to an ordered tetragonal (γ) phase, and then to an ordered rhombohedral phase (ϵ); when increasing T, a disordered hexagonal phase (β) first appears at 2.4 GPa that subsequently transforms into a cubic phase (δ) with orientational disorder by effect of pressure. It is worth noting that large isotopic effects have been observed in the P-induced $\alpha \rightarrow \gamma$ transformation occurring at low temperatures (Scott, 1976), which indicates the presence of important QNE. Some other phases have been observed at higher pressures in the experiments, the structures of which are unknown in most cases. This lack of knowledge has motivated intense theoretical activity in the study of solid nitrogen. Over a dozen different structures have been predicted to be stable in the pressure range $0 \leq P \leq 400$ GPa; among those we highlight the layered $Pba2$ or $Iba2$ (188–320 GPa) and helical tunnel $P2_12_12_1$ structures (>320 GPa) (Ma *et al.*, 2009), and the cluster form of nitrogen diamondoid structures ($>$350 GPa) (Wang *et al.*, 2012), which have been obtained through systematic crystal structure searches based on DFT methods.

Unquestionably, the results of DFT-based studies on molecular nitrogen are invaluable for advancing the knowledge of its phase diagram; however, note that most of the first-principles investigations presented thus far systematically neglect two basic aspects in N_2 crystals: long-range dispersion interactions and QNE (i.e., they have been performed with standard LDA and GGA DFT exchange-correlation functionals and disregarding likely zero-point motion effects even through the quasiharmonic approximation). It could be argued that the importance of these two elements becomes secondary at high pressures, or that somehow they cancel out when comparing the enthalpy of different phases. However, after considering all the similarities between N_2 and H_2 in terms of intermolecular interactions and degree of quantumness, one can suspect that this is actually not the case (i.e., as has been explicitly shown in solid hydrogen, see Sec. VIII.A). Therefore, it is reasonable to think that the transition pressures and phase boundaries reported in standard DFT studies of N_2 are likely to be inaccurate. With regard to this last point, it was

first predicted from standard DFT calculations that molecular nitrogen transforms into a polymeric phase (i.e., cubic *gauche cg*-N) prior to metallization at a pressure of ∼50 GPa (Mailhiot, Yang, and McMahan, 1992). This transformation has been observed subsequently in experiments, however, at thermodynamic conditions much higher than the predicted ones, namely, $P \geq 110$ GPa and $T \geq 2000$ K (Eremets *et al.*, 2004). Whether the causes of these discrepancies between theory and experiments lie in the use of inaccurate DFT functionals and neglection of QNE, the use of incorrect molecular structures in the calculations, the existence of large kinetic barriers for the dissociation of N_2 molecules that complicate the measurements, or a combination of all these factors is not yet clear. Systematic computational studies analyzing the importance of QNE and benchmarking the description of intermolecular interactions in highly compressed nitrogen, therefore, are desirable for clarifying these issues.

To the best of our knowledge, there is only one computational study by Presber *et al.* (1998) in which the importance of QNE on the orientational phase transitions of bulk solid N_2 at low P and low T has been assessed. By using the PIMC method and a classical $N_2 - N_2$ interaction potential, Presber *et al.* (1998) found that the transition temperature corresponding to the $\alpha \rightarrow \gamma$ transformation is reduced by about 11% with respect to the result obtained with classical methods. Note that, in spite of the simplicity of the employed interaction model, Presber *et al.*'s quantum predictions show reasonably good agreement with the experiments.

Similarly, the impact of quantum nuclear effects on the orientational ordering of N_2 molecules adsorbed on graphite has been investigated with PIMC methods by Marx and coworkers in a series of works (Marx *et al.*, 1993; Marx, Sengupta, and Nielaba, 1993; Marx and Müser, 1999). To this end, rigid rotors with their centers of mass pinned on a triangular lattice commensurate with the graphite basal plane, and molecule-molecule and molecule-surface interactions treated with atomistic models and point charges, were analyzed. The main conclusions from those studies were that quantum fluctuations lead to "10% effects" on the physical properties of N_2 films (Marx *et al.*, 1993; Marx, Sengupta, and Nielaba, 1993). For example, the temperature corresponding to the so-called "2-in" herringbone orientational transition that occurs at low temperatures and low densities is shifted down by about 10% as a result of zero-point motion, in good agreement with the experiments. These results imply that in order to make quantitatively correct predictions in N_2 crystals QNE must be taken into account.

Regarding methane, i.e., CH_4, the ground-state phase at low pressures is a cubic structure that can be thought of as two molecular sublattices, one of which is orientationally ordered and the other disordered (James and Keenan, 1959). A first-order phase transition between this cubic and a partially ordered phase occurs at a temperature of 20.4 K (Press and Kollmar, 1975); in CD_4, a similar transition occurs but at a higher temperature of 27.4 K (Press, 1972). This large isotopic effect, again, marks the presence of significant QNE. In fact, by using the PIMC method and a model potential based on *ab initio* results, Müser and Berne (1996) were able to replicate such a large isotopic shift in the transition temperature, otherwise not reproducible with classical methods.

The phase diagram of methane at high pressures, on the other hand, remains contentious. Up to nine different phases have been observed in CH_4 at pressures below ∼10 GPa and temperatures $0 \leq T \leq 300$ K (Bini and Pratesi, 1997; Maynard-Casely *et al.*, 2010), and only three of them have been determined. For instance, based on neutron scattering measurements Maynard-Casely *et al.* (2010) proposed that the so-called phase A, which appears at pressures about 1 GPa and temperatures above ∼100 K, consists of 21 molecules in a rhombohedral unit cell that is strongly distorted with respect to the cubic ground state. Using systematic crystal structure searches based on a genetic algorithm and dispersion-corrected DFT methods, Zhu *et al.* (2012) predicted a similar candidate structure for phase A that, in contrast to the experimentally determined one, presents orientationally disordered molecules. At pressures beyond ∼100 GPa, CH_4 is expected to become chemically unstable and to decompose (Gao *et al.*, 2010). Unfortunately, possibly due in part to the lack of knowledge on the molecular phases that appear below that pressure limit, the impact of QNE on the high-P and low-T phase diagrams of solid methane remains largely unexplored.

Recent simulation studies by Goldman, Reed, and Fried (2009) and Qi and Reed (2012) showed that quantum nuclear effects in fact are crucial for understanding the behavior of solid CH_4 at high-P and high-T conditions. By adopting a quantum thermal bath scheme to treat QNE (see Sec. II.B.3) and a multiscale simulation approach to model the molecular interactions, Qi and Reed (2012) quantified the impact of QNE on the Hugoniot of compressed methane. It has been found that quantum nuclear effects are responsible for a huge shift of ∼40% toward lower pressures in the onset of decomposition. The primary factor behind such a tremendous effect has been ascribed to the large variation in the heat capacity that occurs when QNE are considered. A previous work had already showed that quantum temperature corrections to classical DFT calculations on the Hugoniot of methane were as large as 20%–30%, and that these improved the agreement with the experiments (Goldman, Reed, and Fried, 2009).

Analogously to the situation explained for solid N_2, there is a pressing need for unraveling the influence of QNE on the thermodynamic and structural properties of methane at low and high pressures. From this knowledge, our description and understanding of quantum molecular crystals could be improved significantly.

IX. QUANTUM MATERIALS SCIENCE

Here we explain the physical properties of crystals that are technologically relevant and at the same time are strongly influenced by QNE. In this category we include lightweight and metallic crystals (e.g., Li) through to heavyweight and insulator compounds (e.g., $BaTiO_3$). The former systems respond to the traditional definition of a quantum crystal, that is, solids composed of low-Z atoms that interact through relatively weak forces; the latter systems are better described as highly anharmonic crystals with a shallow multiwell PES.

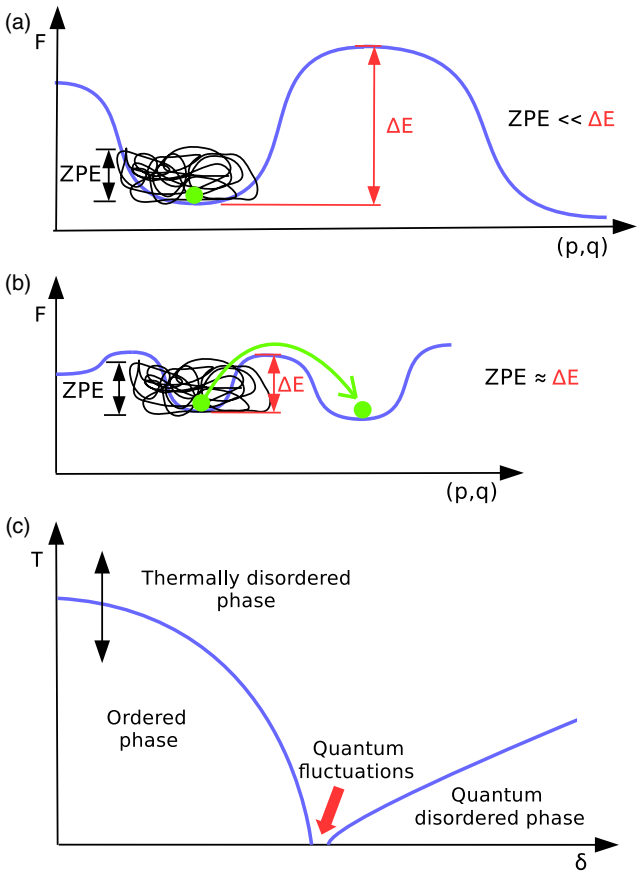

FIG. 20. The influence of QNE in normal systems and materials with a shallow multiwell potential-energy surface (PES). (a) The free-energy barrier separating two local PES minima is too large as compared to the atomic zero-point motion (ZPE), hence the system remains indifferent. (b) The free-energy barrier separating two different states is similar in magnitude to the ZPE; hence the system transits from one to the other. (c) Sketch of the phase diagram in a quantum paraelectric; δ represents a particular tuning field (e.g., pressure).

In this case, disparate phases, identified with local minima in the PES, are energetically very competitive and thus QNE play a crucial role in stabilizing one or another [see Figs. 20(a) and 20(b)].

A. Perovskite oxides

Perovskite oxides have the general formula ABO_3 in which A and B are cations, the latter being a transition metal element with a smaller radius than A. The ideal perovskite structure is cubic with space group $Pm\bar{3}m$, where the B cation is sixfold coordinated with the oxygen anions and A 12-fold coordinated. Perovskite oxides display many interesting physical properties such as, for instance, ferroelectricity (e.g., $BaTiO_3$), ferromagnetism (e.g., $SrRuO_3$), multiple coupled ferroic orders (e.g., $BiFeO_3$), and insulator-to-metallic transitions (e.g., $LaCoO_3$). All these properties are very sensitive to the chemistry, crystalline defects, electrical boundary conditions, and applied stress so that they can be tuned externally. For this reason, pervoskite oxides normally are referred to as functional materials in the literature (Ohtomo and Hwang, 2004; Schlom *et al.*, 2007; Cazorla and Stengel, 2012).

$BaTiO_3$ is an archetypal ferroelectric. At room temperature this material adopts a rhombohedral (R) phase that displays a spontaneous and switchable ferroelectric polarization. As the temperature is raised from zero to ~300 K, $BaTiO_3$ goes through the series of phase transformations $R \rightarrow O \rightarrow T \rightarrow C$, where O stands for an orthorhombic phase, T for a tetragonal, and C for a cubic. The same sequence of phases is observed under pressure (see Fig. 21). The high-T cubic phase corresponds to the ideal perovskite structure, which is nonpolar (that is, has null ferroelectric polarization). The appearance of ferroelectricity in perovskite oxides originates from a delicate balance between long-range Coulomb interactions, that favor the ferroelectric state, and short-range repulsive forces, that favor the cubic nonpolar state; the hybridization between B cation d electronic orbitals and oxygen $2p$ plays an essential part in that equilibrium (Cohen, 1992). The ferroelectric phase transition in $BaTiO_3$ is considered to be an example of displacive transition, in which a zone-center vibrational mode, called "soft," has a vanishing frequency at the phase transition and its eigenvector is similar to the atomic displacements observed in the ferroelectric state. Therefore, $BaTiO_3$ is a highly anharmonic crystal in which several phases are energetically very competitive.

In 2002, Íñiguez and Vanderbilt estimated the impact of QNE on the $P-T$ phase diagram and ferroelectric properties of $BaTiO_3$. Using the PIMC approach based on an effective Hamiltonian model fitted to DFT results, they found that the $P-T$ boundaries separating the regions of stability between different phases varied considerably when considering QNE. As shown in Fig. 21, the phase boundaries are noticeably shifted toward lower pressures and temperatures as compared to those in the classical phase diagram. As a result, the agreement between theory and experiments was improved significantly. Íñiguez and Vanderbilt (2002) also found that the electrical polarization in $BaTiO_3$ shrinks by about 10% when considering quantum fluctuations, and that the same

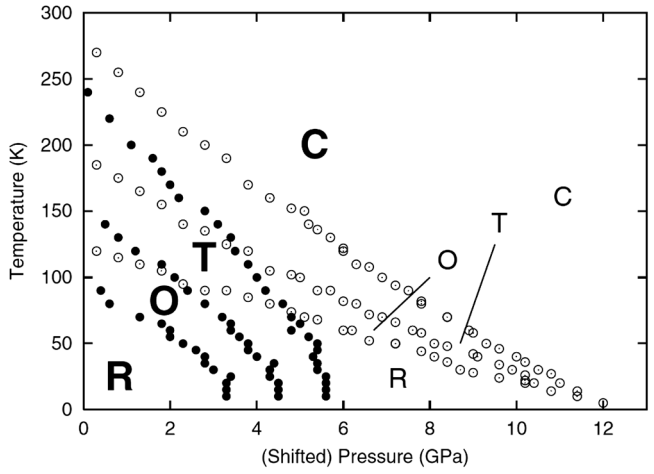

FIG. 21. Phase diagram of $BaTiO_3$ calculated with classical (open circles and small labels) and quantum (solid circles and large labels) simulation methods. From Íñiguez and Vanderbilt, 2002.

quantity exhibits null variation in the $T \to 0$ limit (as expected from quantum arguments) (Hayward and Salje, 1998).

More recently, Geneste *et al.* (2013) analyzed the influence of QNE on the dielectric permittivity and piezoelectric constants of rhombohedral $BaTiO_3$. Using a path-integral molecular dynamics approach based on the same effective Hamiltonian model as that employed by Íñiguez and Vanderbilt (2002), Geneste *et al.* (2013) found that inclusion of quantum nuclear effects systematically enhances the dielectric response and piezoelectric constants of the crystal by approximately a factor of 2. This large effect has been explained in terms of the strong anharmonicity of $BaTiO_3$, which is retained by the crystal down to zero temperature. Geneste *et al.*'s findings suggest that quasiharmonic approaches are not adequate for describing the behavior of displacive ferroelectrics at low temperatures.

QNE can strongly influence the low-T response of a system when it is close to a structural phase transition. In most ferroelectrics, the stability limit of the polar phase T_C falls within a region governed by classical Boltzmann fluctuations. In a few crystals known as "quantum paraelectrics," however, T_C is very close to the zero-temperature limit and thus quantum statistical fluctuations play a dominant role in the transformation (Müller and Burkard, 1979; Rytz, Hochli, and Bilz, 1980; Conduit and Simons, 2010). Examples of quantum paraelectrics include the perovskite oxides $SrTiO_3$, $KTaO_3$, and $KTaO_3$-$NaTaO_3$ and $KTaO_3$-$KNbO_3$ solid solutions (Hochli and Boatner, 1979; Samara, 1988). At low temperatures, the dielectric properties of a quantum paraelectric are appreciably different from those of a classical material. For instance, the Curie-Weiss law describing the variation of the static dielectric constant ϵ near T_C, namely, $\propto (T - T_C)^{-1}$, is no longer fulfilled; instead ϵ follows a $\propto T^{-2}$ relation (Hochli and Boatner, 1979).

As the temperature is raised, or as a specific tuning parameter that induces atomic displacements is varied (e.g., pressure), the dielectric behavior in quantum and classical polar materials eventually becomes analogous. Therefore, a classical-quantum crossover regime exists in quantum paraelectrics in which intriguing quantum phenomena can be expected [see Fig. 20(c)]. This is the case, for instance, of ferroelectric quantum criticality, which has been recently observed in $SrTiO_3$ and $KTaO_3$ crystals (Rowley *et al.*, 2014). In particular, the inverse of the dielectric constant in these materials, which below 50 K follow the nonclassical $\propto T^2$ dependence, experiences an anomalous upturn at very low temperatures that extends into the millikelvin range. This unexpected effect has been rationalized in terms of quantum criticality theory, after considering the influence of long-range dipolar interactions and the coupling of the electrical polarization with acoustic phonons (Rowley *et al.*, 2014). The quantum critical regime associated with quantum paraelectrics is significantly different (e.g., in terms of the collective dynamics and tuning parameter) from the better known quantum regime occurring in quantum ferromagnetic materials (e.g., Ni_3Ga and $ZrZn_2$); interesting new prospects in the field of quantum phase transitions, therefore, appear to be opened.

Quantum paraelectrics are also important from a technological point of view. Currently, there is great interest in exploiting magnetoelectric (ME) effects, which are responsible for the coupling between the electrical and magnetic degrees of freedom in multiferroic crystals, for nanoelectronics applications. ME effects could be used to induce the reversal of the magnetization in a material with an electric field, making it possible to store information in advanced electronic devices with minimal power consumption (i.e., creating magnetic fields generally involves higher energy expenses than electric fields). For ME effects to be practical, the values of the magnetic and electrical susceptibilities need to be large around the same transition temperature. Unfortunately, this rarely occurs in any material. Recently, Shvartsman *et al.* (2010) measured a large ME effect in $EuTiO_3$ near $T_N = 5$ K, a quantum paraelectric that undergoes an antiferromagnetic to paramagnetic phase transition at very low temperatures. The magnetoelectric moments revealed at the magnetic phase transition are comparable to those found in benchmark multiferroic crystals such as $TbPO_4$. Shvartsman *et al.*'s findings suggest that quantum paraelectrics could be promising for nanoelectronic applications.

Nonetheless, for the realization of practical devices based on quantum paraelectrics the observed magnetoelectric activity should be brought closer to room temperature. High compression could represent a solution to this problem as it can extend the regime in which QNE are important while simultaneously shifting T_N toward higher temperatures. In this last regard, the outcomes of quantum simulation studies based on first-principles methods could be very insightful. Actually, recent phonon calculations by Evarestov *et al.* (2011) performed with hybrid DFT methods (see Sec. III.A) have accurately reproduced the experimental T dependence of the heat capacity in $SrTiO_3$. On the other hand, theoretical approaches that allow one to estimate T-renormalized phonon modes and frequencies are already well established (e.g., velocity autocorrelation and self-consistent harmonic methods) (Teweldeberhan, Dubois, and Bonev, 2010; Errea, Rousseau, and Bergara, 2011; Paulatto *et al.*, 2015). To the best of our knowledge, however, full *ab initio* studies of quantum paraelectrics under pressure are absent in the literature.

B. H-bond ferroelectrics

H-bond ferroelectrics normally consist of polar stacks of sheets of hydrogen-bonded molecules. Hydrogen bonding can create electrical dipoles in crystals among hydrogen-donating molecules, which become partially negative, and hydrogen-accepting molecules, which become partially positive. Upon application of an electric field, protons associated with one molecule shift cooperatively toward a hydrogen-bonded neighbor, switching the molecular dipole and thus producing a large electrical polarization (Horiuchi and Tokura, 2008). Examples of H-bond ferroelectrics include the molecular compounds KH_2PO_4 (KDP) and $C_4H_2O_4$ (H2SQ), which present some well-characterized crystal structures and can be synthesized in both standard and deuterated forms. A key aspect in the ferroelectric behavior of most H-bonded ferroelectrics is the motion of H atoms in correlated double-well potentials. This correlation consists of H atoms in neighboring

H bonds being strongly coupled due to the energetic requirement for satisfying the "ice rules" (Singer *et al.*, 2005); in KDP and H2SQ this condition implies that each molecule participates in four different H bonds, two of which have donating character and the rest accepting. H-bond ferroelectric materials currently are attracting a lot of attention because polar order near room temperature has been revealed in some organic species (Horiuchi *et al.*, 2005, 2010). This finding opens the possibility for manufacturing cheaper and more environment friendly nanoelectronic components and devices.

Interestingly, the Curie transition temperature T_C in H-bond ferroelectrics can increase by about 100 K upon deuteration. The origins of such an enormous isotopic effect, however, remain contentious. Originally, a simple quantum model consisting of proton quantum tunneling in a double-well potential was proposed to rationalize the T_C observations (Blinc and Svetina, 1966); however, this simple model failed to explain the so-called Ubbelohde effect, which relates the experimentally observed elongation of H bonds upon deuteration to a purely geometric origin (Ubbelohde and Gallagher, 1955). Subsequently, models involving coupled vibrational lattice modes and proton dynamics were proposed (Dalal, Klymachyov, and Bussmann-Holder, 1998) that led to the conviction that quantum-tunneling effects were not necessary for explaining the isotopic influence on T_C (McMahon *et al.*, 1990). More recently, however, neutron Compton scattering experiments performed on KDP have found evidence for coherent proton quantum tunneling occurring at temperatures above the ferroelectric transition ($T \sim 125$ K), whereas no such evidence is found in the analogous deuterated system (Reiter, Mayers, and Platzman, 2002; Reiter *et al.*, 2008). On the theoretical side, some have attempted to reconcile the differing interpretations by arguing that a mechanism behind the Ubbelohde effect itself might be collective quantum tunneling in atomic clusters (Koval *et al.*, 2002).

Quantum *ab initio* studies of H-bond ferroelectrics are desirable to help in clarifying the controversy about the relevance of QNE on the observed T_C isotope dependence. Nevertheless, due to the large size of the unit cells involved and complex collective dynamics of hydrogen and deuterium atoms, quantum simulation of H-bond ferroelectrics turns out to be very challenging. To the best of our knowledge, the number of published works on this topic can be counted on one hand.

Srinivasan and Sebastiani (2011) performed *ab initio* PIMD simulations in KDP (i.e., KH_2PO_4) and DKDP crystals, in order to estimate the degree of quantum-mechanical localization of hydrogen and deuterium atoms in the paraelectric phase. In both systems, they have found that proton quantum delocalization in the OH $\cdots$ O hydrogen bond is necessary for stabilization of the disordered state. The only difference between KDP and DKDP is that quantum tunneling occurs coherently in the former system whereas it occurs incoherently in the latter, an effect that has been linked to the observed T_C dependence on the isotope.

Recently, Wikfeldt and Michaelides (2014) employed *ab initio* PIMD simulations based on DFT to investigate the importance of QNE on the atomic ordering and structure of H2SQ (i.e., $C_4H_2O_4$). Note that in this case Wikfeldt and Michaelides explicitly considered long-range van der Waals interactions by using a dispersion-corrected DFT functional (see Sec. III.A). It has been found that concerted proton jumps along H-bond chains are facilitated dramatically by quantum tunneling of several protons occurring at the same time. According to Wikfeldt and Michaelides' results, QNE are crucial in this order-disorder phase transition (that is, ferroelectric to paraelectric). The same phenomena have been observed also in the analogous deuterated crystal but with a smaller magnitude, leading to an Ubbelohde effect that is in good agreement with the experiments (i.e., elongation of the oxygen-oxygen distances by $\sim$0.02 Å). Subsequently, Wikfeldt (2014) introduced a simple model for a coupled one-dimensional H-bond chain that has been parametrized to DFT calculations performed in H2SQ. Such an effective model allows for an efficient exploration of QNE in larger systems over longer simulation times. The PIMC results obtained with Wikfeldt's H2SQ model in fact appear to be consistent with the conclusions presented in a previous full *ab initio* work (Wikfeldt and Michaelides, 2014).

Further systematic studies are necessary to exactly determine how important QNE are for understanding the proton dynamics and proton order in H-bond ferroelectrics. The computational evidence gathered to date appears to indicate that quantum nuclear effects certainly are crucial. Reassuringly, in a recent *ab initio* PIMC study Li, Walker, and Michaelides (2011) showed that the quantum nature of the H bond manifests appreciably in most hydrogen-bonded materials.

C. Lithium and related compounds

Lithium is the lightest metallic element; at ambient conditions it is most stable in a cubic bcc crystal. Li represents the prototype of a simple metal with a Fermi surface that is nearly spherical. As pressure is increased, however, this material undergoes a series of symmetry-breaking structural transformations that provoke an increase in complexity of its electronic band structure (Guillaume *et al.*, 2011). The presence of QNE in solid Li under pressure is notable. Experimentally, large isotopic effects have been observed in the equation of state and elastic properties of the bulk crystal at low temperatures ($T \leq 77$ K) and pressures up to $\sim$2 GPa (Gromnitskaya, Stal'gorova, and Stishov, 1999). For instance, differences of about 7% have been reported for the transversal and longitudinal sound-wave velocities in solid ^{6}Li and ^{7}Li at low and high pressures. On the theoretical side, Filippi and Ceperley (1998) analyzed the influence of quantum nuclear effects on the kinetic energy of the crystal with PIMC simulations based on a pairwise interaction potential. It has been found that the excess kinetic energy in Li decreases from about 10.4% of the classical value at 300 K to 4.5% at 450 K; hence QNE are important all the way up to melting. The role of QNE in the structural and electronic properties of small Li clusters has also been estimated as influential by Rousseau and Marx (1998).

One of the effects of applying pressure in a crystal is to increase the kinetic energy of the atoms. It has been argued theoretically that if the increment in zero-point motion due to compression is higher than that attained in the potential

energy, eventually the crystal could melt at low temperatures. This possibility has attracted a great deal of attention in hydrogen since according to some theoretical arguments and effective models a metallic liquid with exotic properties could be stabilized in the region of Mbar pressures (Babaev, Sudbø, and Ashcroft, 2004; Chen *et al.*, 2013). In solid lithium it has been experimentally observed (Lazicki, Fei, and Hemley, 2010) and calculated with first-principles methods (Hernández *et al.*, 2010) that at a pressure of ∼10 GPa the corresponding melting line develops a negative slope (in analogy to what occurs in sodium at $P \sim 30$ GPa). This finding appears to open an alternative for the possible realization of a ground-state metallic liquid at high pressures (although possibly in the region of Mbar pressures, or even at much higher pressures).

The role of QNE in the sudden drop observed in the melting line of Li, however, remains controversial. Guillaume *et al.* (2011) measured a melting temperature of ∼190 K at a pressure of ∼40 GPa, which represents by far the lowest melting temperature observed for any material at such pressures. They suggested that QNE play an important role in shaping the phase diagram of Li. This suggestion seems to be consistent with the fact that classical first-principles simulations (Hernández *et al.*, 2010) provide melting temperatures which are about 100 K higher than the experimental points obtained by Guillaume *et al.* (2011). A more recent experiment by Schaeffer *et al.* (2012), however, has revealed a totally different scenario in which excellent agreement with the classical *ab initio* results by Hernández *et al.* (2010) is obtained. Then, what is the real extent of QNE on the melting properties of Li? Recently, Feng *et al.* (2015) have performed a systematic first-principles PIMD study aimed at answering this question. They found that the net effect of considering QNE on the melting temperature of Li is minimal (e.g., a small shift of 15 K toward lower temperatures at $P = 45$ GPa). Interestingly, QNE noticeably influence the free energy of the solid and liquid phases; however, there is a strong QNE compensation effect between them at melting (Feng *et al.*, 2015).

Lightweight materials based on lithium are important from a technological point of view, and thus so are QNE. Two interesting examples are lithium hydride (LiH) and lithium imide (Li_2NH). LiH is used in the nuclear industry as either a shielding agent or fuel in energy reactors (Welch, 1974; Veleckis, 1977). LiH is an ionic crystal that stabilizes in the rock salt structure at ambient conditions; Li is the cation (positively charged ion) and H the anion (negatively charged ion). The presence of large QNE in LiH has been reported in both experiments and quantum simulations (Boronat *et al.*, 2004). At room temperature the experimental Lindemann ratio of the hydrogen ion amounts to 0.12 (Vidal and Vidal-Valat, 1986), which lies in between those measured for solid H_2 and Ne (i.e., 0.18 and 0.09, respectively), thus indicating very strong quantum character.

Large quantum isotopic effects have been reported in lithium hydride for numerous quantities including the kinetic energy, Lindemann ratio, and lattice parameter. For example, Cazorla and Boronat (2005) estimated by means of VMC calculations based on classical interatomic potentials that the kinetic energy of the hydrogen anion in LiH is 84(1) and in LiD is 67(1) meV. Meanwhile, the corresponding Lindemann ratio is reduced by about 24% in LiD as compared to that in LiH. More recently, Dammak *et al.* (2012) found by using a quantum thermostat approach in combination with first-principles methods that the lattice parameter difference between LiH and LiD amounts to 0.019 and 0.016 Å at 0 and 300 K, respectively, in fairly good agreement with the experiments (namely, 0.016 and 0.014 Å).

QNE can also considerably affect the electronic properties of a quantum solid, in particular, the electronic energy band gap E_g due to the presence of electron-phonon couplings. By using a first-principles approach that consistently takes into account anharmonic and zero-point motion effects, Monserrat, Drummond, and Needs (2013) calculated the quantum-mechanical expectation value of E_g in LiH and LiD over the temperature interval $0 \leq T \leq 800$ K. They found that the isotopic effect in E_g roughly amounts to 4%–7%, with LiD always exhibiting the largest energy band gap. Interestingly, QNE at zero temperature account for a E_g variation of ∼2% as compared to the value calculated with classical methods, which is ∼3.00 eV.

Lithium imide (Li_2NH) is a very promising hydrogen storage material due to its low molecular weight and central role played in the decomposition reaction (Shevlin and Guo, 2009):

$$\begin{aligned} LiNH_2 + 2LiH &\leftrightarrow Li_2NH + LiH + H_2 \\ &\leftrightarrow Li_3N + 2H_2, \end{aligned} \tag{81}$$

where in the first stage a total of 5.5 wt % H_2 is released and 5.2 wt % H_2 in the second. Much research of both computational and experimental nature has been devoted to understand the atomic structure and phase transitions occurring in Li_2NH. Because of the light mass of the atoms and relatively weak interactions between particles, QNE are likely to affect the fundamental properties of this material. Zhang, Dyer, and Alavi (2005) solved the Schrödinger equation of a proton in the potential-energy surface of Li_2NH calculated with DFT methods, to analyze the influence of QNE on its dynamics. It was found that the quantum character of H atoms is very strong, leading to partial delocalization of the proton around certain N centers through quantum tunneling. The origin of this effect has been traced back to the relatively flat potential-energy landscape of the system. The results of a more recent computational study by Ludueña and Sebastiani (2010) based on *ab initio* PIMD simulations appear to support the validity of these results. The proton momentum distribution in Li_2NH has been experimentally measured with inelastic neutron scattering techniques and calculated with quantum thermostatted *ab initio* molecular dynamics (Ceriotti, Miceli *et al.*, 2010). The reported experimental and computational $n(\mathbf{k})$ results are in good agreement, providing a large average kinetic energy of 415 K for Li atoms, of 410 K for N, and of 858 K for H.

The presence of proton quantum tunneling and large zero-point motion in Li_2NH has several implications. First, the conventional treatment of quantum nuclear effects through the quasiharmonic approximation is not adequate in this system. And second, the real energy barrier for hydrogen diffusion, a

key parameter for understanding and designing new H-storage materials, must be lower than predicted with classical simulation methods. In fact, Zhang, Dyer, and Alavi (2005) estimated that at room temperature the H diffusion coefficient in Li_2NH is about 4 orders of magnitude higher than the one expected from classical theory. In light of these results, full quantum treatment of hydrogen atoms in crystals similar to Li_2NH (e.g., $LiBH_4$) may allow for an improved rational engineering of H-storage materials.

D. Carbon-based crystals and nanomaterials

Carbon atoms are found in a large number of technologically relevant materials, including diamond and the prolific family of carbon nanostructures (e.g., graphene, nanotubes, and nanohorns). Diamonds, which due to their strong covalent atomic bonds possess superlative hardness and thermal conductivity, are used as anvil cells to study condensed matter systems over wide $P-T$ ranges and also have a major industrial application as cutting and polishing tools. At low temperatures, diamond is an archetypal quasiharmonic crystal (Ceriotti, Bussi, and Parrinello, 2009) in which the presence of QNE has a profound impact on its structural, elastic, and electronic band-structure features. Herrero and Ramírez (2000) studied the influence of zero-point motion on the thermodynamic properties of this solid with PIMC simulations based on an empirical interatomic potential. They found that QNE account for an increase of 0.5% in the lattice parameter and a decrease of 5% in the bulk modulus with respect to the values obtained with classical simulation methods. More recently, Monserrat, Drummond, and Needs (2013) estimated with fully anharmonic first-principles calculations that the zero-point motion renormalization of the electronic energy band gap in diamond amounts to −461 meV. The origins of this large effect have been discussed in detail by Monserrat and Needs (2014) in terms of important electron-phonon interactions differently affecting valence and conduction band electrons (e.g., the latter are specially sensitive to the size of the Lindemann ratio in the crystal).

Diamondoids, namely, nanocages with formula C_xH_y in which the carbon atoms are sp^3 bonded as in diamond, are biocompatible and superhard molecules. These organic nanoparticles are found in large concentrations in petroleum fluids and currently are attracting a lot of attention due to their potential use in drug delivery and nanotechnology applications (Mochalin *et al.*, 2012). In analogy to diamond, a strong electron-phonon coupling is expected to occur in diamondoids. Recently, Patrick and Giustino (2013) demonstrated by means of first-principles simulations combined with Monte Carlo sampling techniques that the role of QNE in the "photophysics" of these molecules is pivotal. In particular, for the theoretically calculated optical absorption spectra of diamondoids to be in quantitative agreement with the experiments, the zero-point motion of the atoms must be taken into account. Also, the accompanying renormalization of the electronic energy band gaps amounts to 0.4–0.6 eV, depending on the selected C_xH_y species, which coincides with the results obtained by Monserrat, Drummond, and Needs (2013) in diamond.

QNE can significantly affect the gas adsorption and transport properties of carbon-based nanostructures from zero up to room temperature. A case study that has been thoroughly investigated with both theory and experiment is the adsorption and diffusion of hydrogen molecules and atoms on graphene and other related nanomaterials. Understanding this problem correctly is critical from a technological point of view (e.g., for the design of improved hydrogen storage materials) (Cazorla, 2015) and also for fundamental reasons (e.g., to rationalize the formation of molecular hydrogen in the interstellar medium and improve the astrophysical models of star evolution) (Bromley *et al.*, 2014). Experimental evidence of the importance of QNE in hydrogenated carbon-based surfaces and cavities is abundant. Tanaka *et al.* (2005) measured the adsorption of H_2 and D_2 on single-wall carbon nanohorns at $T = 77$ K and reported appreciably different behaviors in the two cases. In particular, around 6%–7% more deuterium molecules are adsorbed on the interior of the nanoparticles. The observed kinetic isotope effect has been ascribed, on the basis of the results of path-integral grand canonical MC simulations performed with semiempirical potentials, to the presence of QNE that favors the localization of D_2 in the cone part of the nanohorns. A similar adsorption isotope effect has also been reported for graphene, which has been interpreted in terms of similar quantum-mechanically nuclear arguments (Paris *et al.*, 2013). Lovell *et al.* (2008) studied the room-temperature adsorption of H_2 in the graphite intercalation compound KC_{24} with inelastic neutron scattering techniques. By comparing their experimental data to the results of quantum first-principles simulations, they concluded that QNE are responsible for a tremendous reduction of ∼60% in the amount of taken gas.

On the purely computational side, Kowalczyk *et al.* (2007) described the physical adsorption of molecular hydrogen in slitlike carbon nanopores at low temperatures and high gas densities, using classical and path-integral grand canonical Monte Carlo simulations based on semiempirical interatomic potentials. It was found that classical simulations overestimate the amount of hydrogen in carbon nanopores due to neglecting of QNE (although the differences between the classical and quantum predictions are ameliorated when the size of the slit-carbon pore diameter is wider than ∼6 Å). Herrero and Ramírez (2010) studied the finite-temperature properties of H_2 molecules adsorbed in graphite using PIMD simulations and a tight-binding potential fitted to DFT calculations. It was shown that H_2 molecules are disposed parallel to the graphite-layer plane and that they can rotate freely about their center of mass in that plane. The stretching mode of the hydrogen molecule is found to change considerably under graphitic confinement by reducing its frequency ∼3.5% with respect to the isolated molecule. Herrero and Ramírez (2010) also reported strong quantum isotopic effects in this system; for instance, at room temperature the ratio between the kinetic energy of H_2 and D_2 amounts to 1.31, where $E_k(H_2)$ is equal to 0.238 eV. Kowalczyk *et al.* (2015) also investigated the structural and dynamical properties of hydrogen and deuterium molecules adsorbed in the interior of carbon-based nanotubes at low temperatures using PIMD techniques and classical force fields. A large isotope effect caused by QNE

has been revealed that consists of H_2 molecules diffusing 7 to 8 times faster than D_2 on the inner H_2/D_2 monolayer that coats the carbon atoms. This effect, which is quantum in nature, could be exploited in lightweight isotope separation processes employing nanoporous molecular sieves.

Several quantum studies involving a variety of simulation techniques have also been performed to investigate the chemisorption and diffusivity of H atoms on graphene (Herrero and Ramírez, 2009; Garashchuk *et al.*, 2013; Karlický, Lepetit, and Lemoine, 2014; Bonfanti *et al.*, 2015). The general picture deriving from all these works is that QNE appreciably facilitate both the adsorption and subsequent diffusion of hydrogen atoms on the carbon surface. Consequently, hydrogenation of large areas of graphene could be achieved more easily in practice than previously inferred from classical simulation studies. Interestingly, Davidson *et al.* (2014) pointed to the need of explicitly considering van der Waals forces in this type of quantum simulation study; the estimated energetic barriers for the chemisorption and diffusion of H atoms then are reduced further, in some cases as much as ∼25% (depending on the employed DFT functional). In view of the results presented in the last part of this section, we can conclude that inclusion of QNE and long-range dispersive interactions in modeling of hydrogenated carbon-based nanomaterials is necessary for providing a realistic estimation of gas-adsorption capacities and transition states at low temperatures.

X. SUMMARY AND OUTLOOK

We have presented an overview of the current understanding of quantum crystals formed by atoms and small molecules over wide thermodynamic intervals, focusing on the insights provided by quantum simulations. We have described the fundamentals of the computational methods that are used to study QNE in quantum solids including variational, projector, and path-integral Monte Carlo techniques, among others. Also, we have explained the basic notions of popular first-principles electronic band-structure methods (e.g., DFT and eQMC) as applied to the description of atomic interactions in crystals.

Our analysis shows that consideration of QNE in computer simulation studies of rare gases, molecular solids, H-bond ferroelectrics, lightweight ionic compounds, carbon-based nanomaterials, and even some perovskite oxides is crucial for understanding the origins of their energy, structural, and functional properties at low temperatures. In most quantum crystals (e.g., ^{4}He, H_2, Li_2NH, and $BaTiO_3$) quasiharmonic approaches turn out to be inadequate for describing their thermodynamic stability and the energy differences between energetically competitive phases. One instead has to consider using methods that fully take into account anharmonicity. Meanwhile, the interatomic interactions in quantum solids normally are not described correctly by standard first-principles (LDA and GGA DFT functionals) or semiempirical approaches. Combination of these two factors makes the simulation of quantum solids very challenging.

QNE are important in a large number of systems and processes that are relevant to materials science. These include hydrogen storage (e.g., Li_2NH and LiH), perovskite oxides (e.g., $BaTiO_3$ and $SrTiO_3$), ferroelectricity (e.g., H-bonded polar compounds), solid plasticity (e.g., ^{4}He), and high-energy density materials (e.g., N_2). It is also likely that QNE are more influential than previously assumed in systems that are relevant to the pharmaceutical industry (molecular crystal polymorphs) and catalysis (diffusion and adsorption of small molecules on carbon-based and metallic surfaces). We hope that our review will motivate new investigations in the context of materials science that will take into consideration the quantum nature of atoms.

In spite of all the insight gathered in quantum solids, there are still a few remaining aspects that need to be better understood. These are essentially related to comprehension of (i) the behavior of different types of crystalline defects and the interactions between them, and (ii) the energy, structural, and dynamical properties of quantum crystals under extreme $P-T$ conditions. Advancing in the first of these two challenges is crucial for substantiating the microscopic arguments that have been proposed to explain the intriguing plastic phenomena observed in solid ^{4}He at ultralow temperatures. In particular, a quantitative description of dislocations at the atomic scale and their interactions with isotopic ^{3}He impurities is still pending. Quantum simulations could contribute significantly to this endeavor. Nevertheless, due to the large size of the simulation cells involved ($\sim 10^4$–10^5 atoms) and inherent structural complexity of line defects, this progress is slow at the moment (Boninsegni *et al.*, 2007; Landinez-Borda, Cai, and de Koning, 2016).

Meanwhile, the crystal structures appearing in the phase diagram of most molecular solids at high pressures are either vaguely characterized or unknown. The outcomes of systematic structural searches based on first-principles methods in fact have been very useful to better identify them. Nevertheless, the influence of QNE on the thermodynamic stability of different high-P polymorphs generally is disregarded in computational studies (see, for instance, the case of N_2 and CH_4), or considered straightforwardly within the quasiharmonic approximation. It is worth stressing once again that a consequence of applying pressure to a crystal is to extend the temperature range over which QNE are relevant; therefore, the presence of quantum nuclear effects such as zero-point motion, quantum atomic exchanges, and quantum tunneling, the majority of which are not correctly reproduced by harmonic-based approaches, is a key aspect in understanding the properties of molecular solids under extreme thermodynamic conditions. Such a comprehension is crucial to advance our knowledge in planetary sciences.

Common to these challenges is the underlying problem of how to correctly describe the interactions between atoms in quantum crystals. As explained before, these interactions require one to go beyond standard first-principles approaches which, in addition to the unavoidable task of treating QNE, sometimes makes the simulation of quantum solids prohibitive in terms of computational expense. In this regard, the outcomes of systematic benchmark studies involving nonstandard DFT and eQMC methods are crucial for rigorously establishing acceptable balances between numerical accuracy and computational load. Further progress in current electronic band structure algorithms, on the one hand, and improvements

in the availability of quantum computer packages which allow one to simulate QNE, on the other hand, would enormously facilitate this task.

As a final reflection, we note that in a few situations QNE are "put under the rug" by arguing that they should play a minor role or somehow cancel out. This is normally supported by a reasoning of the type of "good agreement with the experiments" obtained from classical studies. Nevertheless, several have demonstrated that the causes behind such a good agreement sometimes can be traced back to an inaccurate representation of the atomic forces, which can disguise the real magnitude of QNE (see, for instance, the case of the predicted atomization transition in solid H_2 under pressure) (Chen *et al.*, 2014). Therefore, tests on the influence of QNE in lightweight and highly anharmonic crystals should not be avoided but instead performed systematically. As expressed by Miller (2005), "If one performs only classical simulations, one will never know whether quantum effects are important. One must have the ability to include quantum effects into a simulation, even if only approximately, to know when they are important and when they are not."

ACKNOWLEDGMENTS

This research was supported by the Australian Research Council's Future Fellowship funding scheme (No. FT140100135), and MICINN-Spain (Grants No. MAT2010-18113, No. CSD2007-00041, and No. FIS2014-56257-C2-1-P). Computational resources and technical assistance were provided by the Australian Government and the Government of Western Australia through Magnus under the National Computational Merit Allocation Scheme and The Pawsey Supercomputing Centre.

REFERENCES

Abo-Shaeer, J. R., C. Raman, J. M. Vogels, and W. Ketterle, 2001, Science **292**, 476.
Adamo, C., and V. Barone, 1999, J. Chem. Phys. **110**, 6158.
Ahlrichs, R., R. Penco, and G. Scoles, 1977, Chem. Phys. **19**, 119.
Akahama, Y., M. Nishimura, H. Kawamura, N. Hirao, Y. Ohishi, and K. Takemura, 2010, Phys. Rev. B **82**, 060101(R).
Aleinikava, D., E. Dedits, and A. Kuklov, 2011, J. Low Temp. Phys. **162**, 464.
Alfè, D., A. Bartok, G. Csanyi, and M. J. Gillan, 2013, J. Chem. Phys. **138**, 221102.
Allen, A., M. Richards, and J. Schratter, 1982, J. Low Temp. Phys. **47**, 289.
Ambrosetti, A., A. M. Reilly, R. A. DiStasio, Jr., and A. Tkatchenko, 2014, J. Chem. Phys. **140**, 18A508.
Andersen, O. K., 1975, Phys. Rev. B **12**, 3060.
Anderson, J. B., 1975, J. Chem. Phys. **63**, 1499.
Anderson, J. B., 1976, J. Chem. Phys. **65**, 4121.
Anderson, J. B., 2002, *Quantum Simulations of Complex Many-Body Systems: From Theory to Algorithms*, Lectures Notes, NCI Series (John von Neumann Institute for Computing, Julich, Germany), Vol. 10, p. 25.
Apenko, S. M., 1999, Phys. Rev. B **60**, 3052.
Assaraf, R., and M. Caffarel, 2000, J. Chem. Phys. **113**, 4028.
Astrakharchik, G. E., and J. Boronat, 2014, Phys. Rev. B **90**, 235439.
Astrakharchik, G. E., J. Boronat, I. L. Kurbakov, and Y. E. Lozovik, 2007, Phys. Rev. Lett. **98**, 060405.
Axilrod, B. M., and E. Teller, 1943, J. Chem. Phys. **11**, 299.
Azadi, S., B. Monserrat, W. M. C. Foulkes, and R. J. Needs, 2014, Phys. Rev. Lett. **112**, 165501.
Aziz, R. A., F. R. W. McCourt, and C. C. K. Wong, 1987, Mol. Phys. **61**, 1487.
Aziz, R. A., W. J. Meath, and A. R. Allnatt, 1983, Chem. Phys. **78**, 295.
Aziz, R. A., V. P. S. Nain, J. S. Carley, W. L. Taylor, and G. T. McConville, 1979, J. Chem. Phys. **70**, 4330.
Babaev, E., A. Sudbø, and N. W. Ashcroft, 2004, Nature (London) **431**, 666.
Badinski, A., P. D. Haynes, J. R. Trail, and R. J. Needs, 2010, J. Phys. Condens. Matter **22**, 074202.
Baer, B. J., W. J. Evans, and C.-S. Yoo, 2007, Phys. Rev. Lett. **98**, 235503; **102**, 209901(E) (2009).
Balibar, S., J. Beamish, A. Fefferman, A. Haziot, X. Rojas, and F. Souris, 2016, C.R. Phys. **17**, 264.
Baraffe, I., G. Chabrier, and T. Barman, 2010, Rep. Prog. Phys. **73**, 016901.
Barker, J., 1979, J. Chem. Phys. **70**, 2914.
Baroni, S., and S. Moroni, 1999, Phys. Rev. Lett. **82**, 4745.
Barrat, J. L., and D. Rodney, 2011, J. Stat. Phys. **144**, 679.
Barrozo, A. H., and M. de Koning, 2011, Phys. Rev. Lett. **107**, 198901.
Bartók, A. P., M. J. Gillan, F. R. Manby, and G. Csányi, 2013, Phys. Rev. B **88**, 054104.
Bartók, A. P., M. C. Payne, R. Kondor, and G. Csányi, 2010, Phys. Rev. Lett. **104**, 136403.
Becke, A. D., 1993, J. Chem. Phys. **98**, 5648.
Becke, A. D., and E. R. Johnson, 2007, J. Chem. Phys. **127**, 154108.
Bedoya-Martínez, O. N., J.-L. Barrat, and D. Rodney, 2014, Phys. Rev. B **89**, 014303.
Behler, J., 2010, *Chemical Modelling: Applications and theory*, edited by M. Springborg (RSC Publishing, Cambridge, UK), Vol. 7, pp. 1–41.
Behler, J., 2015, Int. J. Quantum Chem. **115**, 1032.
Benedek, G., A. Kalinin, P. Nieto, and J. P. Toennies, 2016, Phys. Rev. B **93**, 104505.
Benoit, M., D. Marx, and M. Parrinello, 1998, Nature (London) **392**, 258.
Benoit, M., A. H. Romero, and D. Marx, 2002, Phys. Rev. Lett. **89**, 145501.
Bernades, N., 1958, Phys. Rev. **112**, 1534.
Bernu, B., and D. M. Ceperley, 2005, J. Phys. Chem. Solids **66**, 1462.
Bini, R., and G. Pratesi, 1997, Phys. Rev. B **55**, 14800.
Blinc, R., and S. Svetina, 1966, Phys. Rev. **147**, 423.
Blöchl, P. E., 1994, Phys. Rev. B **50**, 17953.
Bonfanti, M., B. Jackson, K. H. Hughes, I. Burghardt, and R. Martinazzo, 2015, J. Chem. Phys. **143**, 124703.
Boninsegni, M., 2004, Phys. Rev. B **70**, 193411.
Boninsegni, M., 2005, New J. Phys. **7**, 78.
Boninsegni, M., 2013a, Phys. Rev. A **87**, 063604.
Boninsegni, M., 2013b, Phys. Rev. Lett. **111**, 235303.
Boninsegni, M., 2016, Phys. Rev. B **93**, 054507.
Boninsegni, M., A. Kuklov, L. Pollet, N. Prokof'ev, B. Svistunov, and M. Troyer, 2007, Phys. Rev. Lett. **99**, 035301.
Boninsegni, M., and S. Moroni, 2000, J. Low Temp. Phys. **118**, 1.
Boninsegni, M., C. Pierleoni, and D. M. Ceperley, 1994, Phys. Rev. Lett. **72**, 1854.
Boninsegni, M., N. Prokof'ev, and B. Svistunov, 2006a, Phys. Rev. E **74**, 036701.

Boninsegni, M., N. Prokof'ev, and B. Svistunov, 2006b, Phys. Rev. Lett. **96**, 105301.

Born, M., and K. Huang, 1954, *Dynamical Theory of Crystal Lattices* (Oxford University Press, New York).

Boronat, J., and J. Casulleras, 1994, Phys. Rev. B **49**, 8920.

Boronat, J., J. Casulleras, and J. Navarro, 1994, Phys. Rev. B **50**, 3427.

Boronat, J., C. Cazorla, D. Colognesi, and M. Zoppi, 2004, Phys. Rev. B **69**, 174302.

Bove, L. E., S. Klotz, A. Paciaroni, and F. Sacchetti, 2009, Phys. Rev. Lett. **103**, 165901.

Bowman, J. M., G. Czakó, and B. Fu, 2011, Phys. Chem. Chem. Phys. **13**, 8094.

Brewer, D. F., J. Rajendra, N. Sharma, and A. L. Thomson, 1990, Physica B (Amsterdam) **165–166**, 569.

Brieuc, F., H. Dammak, and M. Hayoun, 2016, J. Chem. Theory Comput. **12**, 1351.

Brito, B. G. A., and A. Antonelli, 2012, J. Chem. Phys. **137**, 034114.

Bromley, S. T., T. P. M. Goumans, E. Herbst, A. P. Jones, and B. Slater, 2014, Phys. Chem. Chem. Phys. **16**, 18623.

Brown, A., B. J. Braams, K. Christoffel, Z. Jin, and J. M. Bowman, 2003, J. Chem. Phys. **119**, 8790.

Bruce, T. A., 1972, Phys. Rev. B **5**, 4170.

Bruch, L. W., M. W. Cole, and E. Zaremba, 1997, *Physical Adsorption: Forces and Phenomena* (Oxford Science Publications, Oxford).

Bruch, L. W., and I. J. McGee, 1973, J. Chem. Phys. **59**, 409.

Buck, U., F. Huisken, A. Kohlhase, D. Otten, and J. Schaefer, 1983, J. Chem. Phys. **78**, 4439.

Bulatov, V. V., and W. Cai, 2006, *Computer simulations of dislocations* (Oxford University Press, New York).

Burovski, E., E. Zovik, A. Kuklov, N. V. Prokof'ev, and B. V. Svistunov, 2005, Phys. Rev. Lett. **94**, 165301.

Buyukdagli, S., A. V. Savin, and B. Hu, 2008, Phys. Rev. E **78**, 066702.

Calbi, M. M., M. W. Cole, S. M. Gatica, M. J. Bojan, and G. Stan, 2001, Rev. Mod. Phys. **73**, 857.

Callen, H. B., and T. A. Welton, 1951, Phys. Rev. **83**, 34.

Cândido, L., G.-Q. Hai, and D. M. Ceperley, 2011, Phys. Rev. B **84**, 064515.

Cao, J., and B. J. Berne, 1989, J. Chem. Phys. **91**, 6359.

Carrasco, J., B. Santra, J. Klimeš, and A. Michaelides, 2011, Phys. Rev. Lett. **106**, 026101.

Casulleras, J., and J. Boronat, 1995, Phys. Rev. B **52**, 3654.

Casulleras, J., and J. Boronat, 2000, Phys. Rev. Lett. **84**, 3121.

Cazorla, C., 2015, Coord. Chem. Rev. **300**, 142.

Cazorla, C., D. Alfè, and M. J. Gillan, 2008, Phys. Rev. Lett. **101**, 049601.

Cazorla, C., G. E. Astrakharchik, J. Casulleras, and J. Boronat, 2009, New J. Phys. **11**, 013047.

Cazorla, C., and J. Boronat, 2004, J. Low Temp. Phys. **134**, 43.

Cazorla, C., and J. Boronat, 2005, J. Low Temp. Phys. **139**, 645.

Cazorla, C., and J. Boronat, 2008a, J. Phys. Condens. Matter **20**, 015223.

Cazorla, C., and J. Boronat, 2008b, Phys. Rev. B **77**, 024310.

Cazorla, C., and J. Boronat, 2008c, Phys. Rev. B **78**, 134509.

Cazorla, C., and J. Boronat, 2013, Phys. Rev. B **88**, 224501.

Cazorla, C., and J. Boronat, 2015a, Phys. Rev. B **91**, 024103.

Cazorla, C., and J. Boronat, 2015b, Phys. Rev. B **92**, 224113.

Cazorla, C., and J. Boronat, 2015c, J. Low Temp. Phys. **180**, 20.

Cazorla, C., and D. Errandonea, 2014, Phys. Rev. Lett. **113**, 235902.

Cazorla, C., D. Errandonea, and E. Sola, 2009, Phys. Rev. B **80**, 064105.

Cazorla, C., and J. Íñiguez, 2013, Phys. Rev. B **88**, 214430.

Cazorla, C., Y. Lutsyshyn, and J. Boronat, 2012, Phys. Rev. B **85**, 024101.

Cazorla, C., Y. Lutsyshyn, and J. Boronat, 2013, Phys. Rev. B **87**, 214522.

Cazorla, C., S. A. Shevlin, and Z. X. Guo, 2011, J. Phys. Chem. C **115**, 10990.

Cazorla, C., and M. Stengel, 2012, Phys. Rev. B **85**, 075426.

Cencek, W., K. Patkowski, and K. Szalewicz, 2009, J. Chem. Phys. **131**, 064105.

Ceperley, D. M., 1995, Rev. Mod. Phys. **67**, 279.

Ceperley, D. M., and B. J. Alder, 1980, Phys. Rev. Lett. **45**, 566.

Ceperley, D. M., and B. J. Alder, 1984, J. Chem. Phys. **81**, 5833.

Ceperley, D. M., and B. J. Alder, 1987, Phys. Rev. B **36**, 2092.

Ceperley, D. M., and B. Bernu, 2004, Phys. Rev. Lett. **93**, 155303.

Ceperley, D. M., G. V. Chester, and M. H. Kalos, 1976, Phys. Rev. D **13**, 3208.

Ceperley, D. M., G. V. Chester, and M. H. Kalos, 1978, Phys. Rev. B **17**, 1070.

Ceperley, D. M., and G. Jacucci, 1987, Phys. Rev. Lett. **58**, 1648.

Ceperley, D. M., and M. H. Kalos, 1979, *Quantum many-body problems in Monte Carlo Methods in Statistical Physics*, edited by K. Binder (Springer-Verlag, Berlin).

Ceperley, D. M., and H. Partridge, 1986, J. Chem. Phys. **84**, 820.

Ceperley, D. M., R. O. Simmons, and R. C. Blasdell, 1996, Phys. Rev. Lett. **77**, 115.

Ceriotti, M., G. Bussi, and M. Parrinello, 2009, Phys. Rev. Lett. **103**, 030603.

Ceriotti, M., and D. E. Manolopoulos, 2012, Phys. Rev. Lett. **109**, 100604.

Ceriotti, M., D. E. Manolopoulos, and M. Parrinello, 2011, J. Chem. Phys. **134**, 084104.

Ceriotti, M., G. Miceli, A. Pietropaolo, D. Colognesi, A. Nale, M. Catti, M. Bernasconi, and M. Parrinello, 2010, Phys. Rev. B **82**, 174306.

Ceriotti, M., J. More, and D. E. Manolopoulos, 2014, Comput. Phys. Commun. **185**, 1019.

Ceriotti, M., M. Parrinello, T. E. Markland, and D. E. Manolopoulos, 2010, J. Chem. Phys. **133**, 124104.

Chai, J.-D., and M. Head-Gordon, 2008, Phys. Chem. Chem. Phys. **10**, 6615.

Chakravarty, C., 1997, Int. Rev. Phys. Chem. **16**, 421.

Chan, M. H. W., R. B. Hallock, and L. Reatto, 2013, J. Low Temp. Phys. **172**, 317.

Chandler, D., and P. G. Wolynes, 1981, J. Chem. Phys. **74**, 4078.

Chen, J., X.-Z. Li, Q.-F. Zhang, M. I. J. Probert, C. J. Pickard, R. J. Needs, A. Michaelides, and E. Wang, 2013, Nat. Commun. **4**, 2064.

Chen, J., X. Ren, X.-Z. Li, D. Alfè, and E. Wang, 2014, J. Chem. Phys. **141**, 024501.

Cheng, Z. G., and J. Beamish, 2016, Phys. Rev. Lett. **117**, 025301.

Cheng, Z. G., J. Beamish, A. D. Fefferman, F. Souris, and S. Balibar, 2015, Phys. Rev. Lett. **114**, 165301.

Chiesa, S., D. M. Ceperley, R. M. Martin, and M. Holzmann, 2006, Phys. Rev. Lett. **97**, 076404.

Chiesa, S., D. M. Ceperley, and S. Zhang, 2005, Phys. Rev. Lett. **94**, 036404.

Chin, S. A., and C. R. Chen, 2002, J. Chem. Phys. **117**, 1409.

Clark, B. K., and D. M. Ceperley, 2006, Phys. Rev. Lett. **96**, 105302.

Clark, B. K., and D. M. Ceperley, 2008, Comput. Phys. Commun. **179**, 82.

Clay, III, R. C., M. Holzmann, D. M. Ceperley, and M. A. Morales, 2016, Phys. Rev. B **93**, 035121.

Clay, III, R. C., J. Mcminis, J. McMahon, C. Pierleoni, D. M. Ceperley, and M. A. Morales, 2014, Phys. Rev. B **89**, 184106.
Clements, B. E., J. L. Epstein, E. Krotscheck, and M. Saarela, 1993, Phys. Rev. B **48**, 7450.
Clements, B. E., E. Krotscheck, and M. Saarela, 1997, Phys. Rev. B **55**, 5959.
Cohen, R. E., 1992, Nature (London) **358**, 136.
Colognesi, D., U. Bafile, M. Celli, and M. Neumann, 2015, Chem. Phys. **446**, 57.
Conduit, G. J., and B. D. Simons, 2010, Phys. Rev. B **81**, 024102.
Cooper, N. R., N. K. Wilkin, and J. M. F. Gunn, 2001, Phys. Rev. Lett. **87**, 120405.
Corboz, P., M. Boninsegni, L. Pollet, and M. Troyer, 2008, Phys. Rev. B **78**, 245414.
Cotterill, R. M. J., and M. Doyama, 1966, Phys. Rev. **145**, 465.
Cox, S., M. Towler, D. Alfè, and A. Michaelides, 2014, J. Chem. Phys. **140**, 174703.
Crepeau, R. H., O. Heybey, D. M. Lee, and S. A. Strauss, 1971, Phys. Rev. A **3**, 1162.
Cuccoli, A., A. Macchi, V. Tognetti, and R. Vaia, 1993, Phys. Rev. B **47**, 14923.
Cuervo, J. E., and P. N. Roy, 2006, J. Chem. Phys. **125**, 124314.
Cui, L., N. H. Chen, and I. F. Silvera, 1995, Phys. Rev. B **51**, 14987.
Cui, T., E. Cheng, B. J. Alder, and K. B. Whaley, 1997, Phys. Rev. B **55**, 12253.
Dalal, N., A. Klymachyov, and A. Bussmann-Holder, 1998, Phys. Rev. Lett. **81**, 5924.
Dalladay-Simpson, P., R. T. Howie, and E. Gregoryanz, 2016, Nature (London) **529**, 63.
Dammak, H., E. Antoshchenkova, M. Hayoun, and F. Finocchi, 2012, J. Phys. Condens. Matter **24**, 435402.
Dammak, H., Y. Chalopin, M. Laroche, M. Hayoun, and J.-J. Greffet, 2009, Phys. Rev. Lett. **103**, 190601.
Davidson, E. R. M., J. Klimeš, D. Alfè, and A. Michaelides, 2014, ACS Nano **8**, 9905.
Dawes, R., D. L. Thompson, Y. Guo, A. F. Wagner, and M. Minkoff, 2007, J. Chem. Phys. **126**, 184108.
Day, J., and J. R. Beamish, 2007, Nature (London) **450**, 853.
Dewaele, A., F. Datchi, P. Loubeyre, and M. Mezouar, 2008, Phys. Rev. B **77**, 094106.
Dewaele, A., M. Mezouar, N. Guignot, and P. Loubeyre, 2010, Phys. Rev. Lett. **104**, 255701.
Diallo, S. O., J. V. Pearce, R. T. Azuah, and H. R. Glyde, 2004, Phys. Rev. Lett. **93**, 075301.
Diallo, S. O., J. V. Pearce, R. T. Azuah, O. Kirichek, J. W. Taylor, and H. R. Glyde, 2007, Phys. Rev. Lett. **98**, 205301.
Diatschenko, V., C. W. Chu, D. H. Liebenberg, D. A. Young, M. Ross, and R. L. Mills, 1985, Phys. Rev. B **32**, 381.
Dion, M., H. Rydberg, E. Schroder, D. C. Langreth, and B. I. Lundqvist, 2004, Phys. Rev. Lett. **92**, 246401.
Dobson, J. F., and T. Gould, 2012, J. Phys. Condens. Matter **24**, 073201.
Dobson, J. F., A. White, and A. Rubio, 2006, Phys. Rev. Lett. **96**, 073201.
Domb, C., and J. S. Dugdale, 1957, *Progress in Low Temperature Physics* (North-Holland Publ., Amsterdam), Vol. 2, p. 338.
Draeger, E. W., and D. M. Ceperley, 2000, Phys. Rev. B **61**, 12094.
Drechsel-Grau, C., and D. Marx, 2014, Phys. Rev. Lett. **112**, 148302.
Driessen, A., J. A. de Waal, and I. F. Silvera, 1979, J. Low Temp. Phys. **34**, 255.
Driver, K., R. E. Cohen, Z. Wu, P. López-Ríos, M. D. Towler, R. J. Needs, and J. W. Wilkins, 2010, Proc. Natl. Acad. Sci. U.S.A. **107**, 9519.
Driver, K., and B. Militzer, 2012, Phys. Rev. Lett. **108**, 115502.
Drummond, N. D., B. Monserrat, J. H. Lloyd-Williams, P. López-Ríos, C. J. Pickard, and R. J. Needs, 2015, Nat. Commun. **6**, 7794.
Drummond, N. D., and R. J. Needs, 2009, Phys. Rev. Lett. **102**, 126402.
Drummond, N. D., R. J. Needs, A. Sorouri, and W. M. C. Foulkes, 2008, Phys. Rev. B **78**, 125106.
Drummond, N. D., Z. Radnai, J. R. Trail, M. D. Towler, and R. J. Needs, 2004, Phys. Rev. B **69**, 085116.
Dzyabura, V., M. Zaghoo, and I. F. Silvera, 2013, Proc. Natl. Acad. Sci. U.S.A. **110**, 8040.
Eckert, J., W. Thomlinson, and G. Shirane, 1977, Phys. Rev. B **16**, 1057.
Edwards, D. O., and R. C. Pandorf, 1965, Phys. Rev. **140**, A816.
Engel, E. A., B. Monserrat, and R. J. Needs, 2015, Phys. Rev. X **5**, 021033.
Engel, E. A., B. Monserrat, and R. J. Needs, 2016, J. Chem. Phys. **145**, 044703.
Ercolessi, F., and J. B. Adams, 1994, Europhys. Lett. **26**, 583.
Eremets, M. I., A. G. Gavriliuk, I. A. Trojan, D. A. Dzivenko, and R. Boehler, 2004, Nat. Mater. **3**, 558.
Eremets, M. I., and I. A. Trojan, 2011, Nat. Mater. **10**, 927.
Errandonea, D., R. Boehler, S. Japel, M. Mezouar, and L. R. Benedetti, 2006, Phys. Rev. B **73**, 092106.
Errea, I., M. Calandra, and F. Mauri, 2013, Phys. Rev. Lett. **111**, 177002.
Errea, I., M. Calandra, C. J. Pickard, J. Nelson, R. J. Needs, Y. Li, H. Liu, Y. Zhang, Y. Ma, and F. Mauri, 2015, Phys. Rev. Lett. **114**, 157004.
Errea, I., B. Rousseau, and A. Bergara, 2011, Phys. Rev. Lett. **106**, 165501.
Esler, K. P., J. Kim, L. Shulenburger, and D. M. Ceperley, 2012, Comput. Sci. Eng. **14**, 40.
Evarestov, R. A., E. Blokhin, D. Gryaznov, E. A. Kotomin, and J. Maier, 2011, Phys. Rev. B **83**, 134108.
Fahy, S., X. W. Wang, and S. G. Louie, 1988, Phys. Rev. Lett. **61**, 1631.
Fahy, S., X. W. Wang, and S. G. Louie, 1990, Phys. Rev. B **42**, 3503.
Fefferman, A. D., F. Souris, A. Haziot, J. R. Beamish, and S. Balibar, 2014, Phys. Rev. B **89**, 014105.
Feng, Y., J. Chen, D. Alfè, X.-Z. Li, and E. Wang, 2015, J. Chem. Phys. **142**, 064506.
Feynman, P. R., 1948, Rev. Mod. Phys. **20**, 367.
Feynman, P. R., 1956, Phys. Rev. **102**, 1189.
Feynman, P. R., 1972, *Statistical Mechanics: A set of lectures* (Benjamin/Cummings Publishing, Massachusetts).
Feynman, P. R., and A. R. Hibbs, 1965, *Quantum Mechanics and Path Integrals* (McGraw-Hill, New York).
Filippi, C., and D. M. Ceperley, 1998, Phys. Rev. B **57**, 252.
Filippi, C., and C. J. Umrigar, 2000, Phys. Rev. B **61**, R16291.
Flammini, D., A. Pietropaolo, R. Senesi, C. Andreani, F. McBride, A. Hodgson, M. A. Adams, L. Lin, and R. Car, 2012, J. Chem. Phys. **136**, 024504.
Fortney, J., 2004, Science **305**, 1414.
Foulkes, W. M. C., L. Mitas, R. J. Needs, and G. Rajagopal, 2001, Rev. Mod. Phys. **73**, 33.
Fraass, B. A., P. R. Granfors, and R. O. Simmons, 1989, Phys. Rev. B **39**, 124.
Fraser, L. M., W. M. C. Foulkes, G. Rajagopal, R. J. Needs, S. D. Kenny, and A. J. Williamson, 1996, Phys. Rev. B **53**, 1814.
Freiman, Y. A., A. Grechnev, S. M. Tretyak, A. G. Goncharov, C. S. Zha, and R. J. Hemley, 2013, Phys. Rev. B **88**, 214501.

Fuchs, G. D., G. Burkard, P. V. Klimov, and D. D. Awschalom, 2011, Nat. Phys. **7**, 789.

Furukawa, G. T., 1972, Metrologia **8**, 11.

Gadipelli, S., and Z. X. Guo, 2015, Prog. Mater. Sci. **69**, 1.

Gai, H., G. K. Schenter, and B. C. Garrett, 1996a, J. Chem. Phys. **104**, 680.

Gai, H., G. K. Schenter, and B. C. Garrett, 1996b, J. Chem. Phys. **104**, 680.

Galli, D. E., and L. Reatto, 2004, J. Low Temp. Phys. **134**, 121.

Galli, D. E., and L. Reatto, 2006, Phys. Rev. Lett. **96**, 165301.

Galli, D. E., M. Rossi, and L. Reatto, 2005, Phys. Rev. B **71**, 140506.

Gao, G., A. R. Oganov, Y. Ma, H. Wang, P. Li, Y. Li, T. Iitaka, and G. Zou, 2010, J. Chem. Phys. **133**, 144508.

Garashchuk, S., J. Jakowski, L. Wang, and B. G. Sumpter, 2013, J. Chem. Theory Comput. **9**, 5221.

Geneste, G., H. Dammak, M. Hayoun, and M. Thiercelin, 2013, Phys. Rev. B **87**, 014113.

Geneste, G., M. Torrent, F. Bottin, and P. Loubeyre, 2012, Phys. Rev. Lett. **109**, 155303.

Georgescu, I. M., S. Ashhab, and F. Nori, 2014, Rev. Mod. Phys. **86**, 153.

Giamarchi, T., 2004, *Quantum Physics in One Dimension* (Oxford University Press, New York).

Gillan, M. J., 1990, *Computer Modelling of Fluids, Polymers, and Solids* (Kluwer, Dordrecht).

Gillan, M. J., D. Alfè, and A. Michaelides, 2016, J. Chem. Phys. **144**, 130901.

Giorgini, S., J. Boronat, and J. Casulleras, 1996, Phys. Rev. B **54**, 6099.

Glyde, H. R., 1994, *Excitations in liquid and solid helium* (Clarendon Press, Oxford).

Gobre, V. V., and A. Tkatchenko, 2013, Nat. Commun. **4**, 2341.

Goldman, N., E. J. Reed, and L. E. Fried, 2009, J. Chem. Phys. **131**, 204103.

Goncharov, A. F., E. Gregoryanz, R. J. Hemley, and H. k. Mao, 2001, Proc. Natl. Acad. Sci. U.S.A. **98**, 14234.

Goncharov, A. F., R. J. Hemley, and H. J. Mao, 2011, J. Chem. Phys. **134**, 174501.

Goncharov, A. F., R. J. Hemley, H. k. Mao, and J. Shu, 1998, Phys. Rev. Lett. **80**, 101.

Goncharov, A. F., R. T. Howie, and E. Gregoryanz, 2013, Low Temp. Phys. **39**, 402.

Goncharov, A. F., I. I. Mazin, J. H. Eggert, R. J. Hemley, and H. k. Mao, 1995, Phys. Rev. Lett. **75**, 2514.

Gonze, X., *et al.*, 2016, Comput. Phys. Commun. **205**, 106.

Gordillo, M. C., and J. Boronat, 2009a, J. Low Temp. Phys. **157**, 296.

Gordillo, M. C., and J. Boronat, 2009b, Phys. Rev. Lett. **102**, 085303.

Gordillo, M. C., and J. Boronat, 2010, Phys. Rev. B **81**, 155435.

Gordillo, M. C., and J. Boronat, 2011, Phys. Rev. B **84**, 033406.

Gordillo, M. C., J. Boronat, and J. Casulleras, 2000a, Phys. Rev. B **61**, R878.

Gordillo, M. C., J. Boronat, and J. Casulleras, 2000b, Phys. Rev. Lett. **85**, 2348.

Gordillo, M. C., C. Cazorla, and J. Boronat, 2011, Phys. Rev. B **83**, 121406(R).

Gordillo, M. C., and D. M. Ceperley, 1997, Phys. Rev. Lett. **79**, 3010.

Granato, A., and K. Lücke, 1956, J. Appl. Phys. **27**, 583.

Grau, V., J. Boronat, and J. Casulleras, 2002, Phys. Rev. Lett. **89**, 045301.

Grebenev, S., J. P. Toennies, and A. F. Vilesov, 1998, Science **279**, 2083.

Grechnev, A., S. M. Tretyak, Y. A. Freiman, A. F. Goncharov, and E. Gregoryanz, 2015, Phys. Rev. B **92**, 024102.

Gregoryanz, E., A. F. Goncharov, C. Sanloup, M. Somayazulu, H.-K. Mao, and R. J. Hemley, 2007, J. Chem. Phys. **126**, 184505.

Greywall, D. S., 1977, Phys. Rev. B **16**, 5127.

Grimme, S., 2004, J. Comput. Chem. **25**, 1463.

Grimme, S., J. Antony, S. Ehrlich, and H. Krieg, 2010, J. Chem. Phys. **132**, 154104.

Grimsditch, M.P. Loubeyre, and A. Polian, 1986, Phys. Rev. B **33**, 7192.

Grimvall, G., B. Magyari-Köpe, and V. Ozoliņš, and K. A. Persson, 2012, Rev. Mod. Phys. **84**, 945.

Grochala, W., and P. P. Edwards, 2004, Chem. Rev. **104**, 1283.

Gromnitskaya, E. L., O. V. Stal'gorova, and S. M. Stishov, 1999, JETP Lett. **69**, 38.

Grossman, J. C., and L. Mitas, 2005, Phys. Rev. Lett. **94**, 056403.

Guardiola, R., 1986, *First international course on condensed matter* (World Scientific, Bogota), Vol. 8, p. 157.

Guardiola, R., and J. Navarro, 2008, Central Eur. J. Phys. **6**, 33.

Guillaume, C. L., E. Gregoryanz, O. Degtyareva, M. I. McMahon, M. Hanfland, S. Evans, M. Guthrie, S. V. Sinogeikin, and H.-K. Mao, 2011, Nat. Phys. **7**, 211.

Habershon, S., D. E. Manolopoulos, T. E. Markland, and T. F. Miller, III, 2013, Annu. Rev. Phys. Chem. **64**, 387.

Haldane, F. D. M., 1981, Phys. Rev. Lett. **47**, 1840.

Hallock, R., 2015, Phys. Today **68**, 30.

Hammond, B. L., W. A. Lester, Jr., and P. J. Reynolds, 1994, *Monte Carlo Methods in Ab Initio Quantum Chemistry* (World Scientific, Singapore).

Hammond, B. L., P. J. Reynolds, and W. A. Lester, Jr., 1987, J. Chem. Phys. **87**, 1130.

Hansen, J.-P., 1968, Phys. Rev. **172**, 919.

Hansen, J.-P., and D. Levesque, 1968, Phys. Rev. **165**, 293.

Hayward, S. A., and E. K. H. Salje, 1998, J. Phys. Condens. Matter **10**, 1421.

Haziot, A., A. D. Fefferman, J. R. Beamish, and S. Balibar, 2013, Phys. Rev. B **87**, 060509(R).

Haziot, A., A. D. Fefferman, F. Souris, J. R. Beamish, H. J. Maris, and S. Balibar, 2013, Phys. Rev. B **88**, 014106.

Haziot, A., X. Rojas, A. D. Fefferman, J. R. Beamish, and S. Balibar, 2013a, Phys. Rev. Lett. **110**, 035301.

Haziot, A., X. Rojas, A. D. Fefferman, J. R. Beamish, and S. Balibar, 2013b, Phys. Rev. Lett. **111**, 119602.

Hemley, R. J., 2000, Annu. Rev. Phys. Chem. **51**, 763.

Hemley, R. J., and H. K. Mao, 1988, Phys. Rev. Lett. **61**, 857.

Henning, R. G., A. Wadehra, K. P. Driver, W. D. Parker, C. J. Umrigar, and J. W. Wilkins, 2010, Phys. Rev. B **82**, 014101.

Hepburn, J., G. Scoles, and R. Penco, 1975, Chem. Phys. Lett. **36**, 451.

Hernández, E., A. Rodriguez-Prieto, A. Bergara, and D. Alfè, 2010, Phys. Rev. Lett. **104**, 185701.

Hernández-Rojas, J., F. Calvo, and E. González-Noya, 2015, J. Chem. Theory Comput. **11**, 861.

Herrero, C. P., and R. Ramírez, 2000, Phys. Rev. B **63**, 024103.

Herrero, C. P., and R. Ramírez, 2009, Phys. Rev. B **79**, 115429.

Herrero, C. P., and R. Ramírez, 2010, Phys. Rev. B **82**, 174117.

Herrero, C. P., and R. Ramírez, 2011a, J. Chem. Phys. **134**, 094510.

Herrero, C. P., and R. Ramírez, 2011b, Phys. Rev. B **84**, 224112.

Herrero, C. P., and R. Ramírez, 2012, J. Chem. Phys. **137**, 104505.

Herrero, C. P., and R. Ramírez, 2014, J. Phys. Condens. Matter **26**, 233201.

Heyd, J., G. E. Scuseria, and M. Ernzerhof, 2003, J. Chem. Phys. **118**, 8207.

Hinde, R. J., 2011, Comput. Phys. Commun. **182**, 2339.

Hochli, U. T., and L. A. Boatner, 1979, Phys. Rev. B **20**, 266.

Holzmann, M., R. C. Clay, III, M. A. Morales, N. M. Tubman, D. M. Ceperley, and C. Pierleoni, 2016, Phys. Rev. B **94**, 035126.
Hood, R. Q., M.-Y. Chou, A. J. Williamson, G. Rajagopal, R. J. Needs, and W. M. C. Foulkes, 1997, Phys. Rev. Lett. **78**, 3350.
Horiuchi, S., F. Ishii, R. Kumai, Y. Okimoto, H. Tachibana, N. Nagaosa, and Y. Tokura, 2005, Nat. Mater. **4**, 163.
Horiuchi, S., Y. Tokunaga, G. Giovannetti, S. Picozzi, H. Itoh, R. Shimano, R. Kumai, and Y. Tokura, 2010, Nature (London) **463**, 789.
Horiuchi, S., and Y. Tokura, 2008, Nat. Mater. **7**, 357.
Howie, R. T., C. L. Guillaume, T. Scheler, A. F. Goncharov, and E. Gregoryanz, 2012, Phys. Rev. Lett. **108**, 125501.
Howie, R. T., T. Scheler, C. L. Guillaume, and E. Gregoryanz, 2012, Phys. Rev. B **86**, 214104.
Hubbard, W. B., W. J. Nellis, A. C. Mitchell, N. C. Holmes, S. S. Limaye, and P. C. McCandless, 1991, Science **253**, 648.
Huihuo, Z., and L. K. Wagner, 2015, Phys. Rev. Lett. **114**, 176401.
Hull, D., and D. J. Bacon, 2011, *Introduction to dislocations* (Elsevier, Amsterdam), 5th ed.
Hurley, M. M., and P. A. Christiansen, 1987, J. Chem. Phys. **86**, 1069.
Hutter, J., M. Iannuzzi, F. Schiffmann, and J. VandeVondele, 2014, WIREs Comput. Mol. Sci. **4**, 15.
Imambekov, A., T. L. Schmidt, and L. I. Glazman, 2012, Rev. Mod. Phys. **84**, 1253.
Íñiguez, J., and D. Vanderbilt, 2002, Phys. Rev. Lett. **89**, 115503.
James, H. M., and T. A. Keenan, 1959, J. Chem. Phys. **31**, 12.
Jiang, X., X. Cheng, G. Chen, and H. Zhang, 2012, Int. J. Quantum Chem. **112**, 2627.
Kalos, M. H., 1962, Phys. Rev. **128**, 1791.
Kalos, M. H., D. Levesque, and L. Verlet, 1974, Phys. Rev. A **9**, 2178.
Kang, D., J. Dai, H. Sun, Y. Hou, and J. Yuan, 2013, Sci. Rep. **3**, 3272.
Karlický, F., B. Lepetit, and D. Lemoine, 2014, J. Chem. Phys. **140**, 124702.
Keesom, W. H., 1942, *Helium* (Elsevier, Amsterdam).
Khairallah, S. A., M. B. Sevryuk, D. M. Ceperley, and J. P. Toennies, 2007, Phys. Rev. Lett. **98**, 183401.
Kim, D. Y., and M. H. W. Chan, 2012, Phys. Rev. Lett. **109**, 155301.
Kim, D. Y., and M. H. W. Chan, 2014, Phys. Rev. B **90**, 064503.
Kim, E., and M. H. W. Chan, 2004a, Nature (London) **427**, 225.
Kim, E., and M. H. W. Chan, 2004b, Science **305**, 1941.
Kim, J., K. P. Esler, J. McMinis, M. A. Morales, B. K. Clark, L. Shulenburger, and D. M. Ceperley, 2012, J. Phys. Conf. Ser. **402**, 012008.
Kim, S. S., C. Huan, L. Yin, J. Xia, D. Candela, and N. Sullivan, 2013, Phys. Rev. B **87**, 224303.
Kinder, J., A. Bouwen, and D. Schoemaker, 1995, Phys. Lett. A **203**, 251.
Kitamura, H., S. Tsuneyuki, T. Ogitsu, and T. Miyake, 2000, Nature (London) **404**, 259.
Kittel, C., 2005, *Introduction to Solid State Physics* (Wiley, Hoboken), 8th ed.
Klein, M. L., and J. A. Venables, 1974, *Rare Gas Solids* (Academic Press, San Francisco).
Klimeš, J., and A. Michaelides, 2012, J. Chem. Phys. **137**, 120901.
Koehler, T. R., 1966, Phys. Rev. Lett. **17**, 89.
Koehler, T. R., 1967, Phys. Rev. Lett. **18**, 654.
Kohanoff, J., S. Scandolo, G. L. Chiarotti, and E. Tosatti, 1997, Phys. Rev. Lett. **78**, 2783.
Kohn, W., and L. J. Sham, 1965, Phys. Rev. **140**, A1133.
Kong, L., X. Wu, and R. Car, 2012, Phys. Rev. B **86**, 134203.
Kosevich, A. M., 2005, *The Crystal Lattice: Phonons, Solitons, Dislocations, Superlattices* (Wiley-VCH, Berlin), 2nd ed.
Koval, S., J. Kohanoff, R. L. Migoni, and E. Tosatti, 2002, Phys. Rev. Lett. **89**, 187602.
Kowalczyk, P., P. A. Gauden, A. P. Terzyk, and S. K. Bhatia, 2007, Langmuir **23**, 3666.
Kowalczyk, P., A. P. Terzyk, P. A. Gauden, S. Furmaniak, K. Kaneko, and T. F. Miller, 2015, J. Phys. Chem. Lett. **6**, 3367.
Kühnel, M., J. M. Fernández, G. Tejeda, A. Kalinin, S. Montero, and R. E. Grisenti, 2011, Phys. Rev. Lett. **106**, 245301.
Kuklov, A., L. Pollet, N. V. Prokof'ev, and B. V. Svistunov, 2014, Phys. Rev. B **90**, 184508.
Kwon, Y., D. M. Ceperley, and R. M. Martin, 1993, Phys. Rev. B **48**, 12037.
Kwon, Y., D. M. Ceperley, and R. M. Martin, 1998, Phys. Rev. B **58**, 6800.
Labet, V., P. Gonzalez-Morelos, R. Hoffmann, and N. Ashcroft, 2012, J. Chem. Phys. **136**, 074501.
Labet, V., R. Hoffmann, and N. Ashcroft, 2012a, J. Chem. Phys. **136**, 074502.
Labet, V., R. Hoffmann, and N. Ashcroft, 2012b, J. Chem. Phys. **136**, 074503.
Labet, V., R. Hoffmann, and N. Ashcroft, 2012c, J. Chem. Phys. **136**, 074504.
Landinez-Borda, E. J., W. Cai, and M. de Koning, 2014, Phys. Rev. Lett. **112**, 155303.
Landinez-Borda, E. J., W. Cai, and M. de Koning, 2016, Phys. Rev. Lett. **117**, 045301.
Langel, W., D. L. Price, R. O. Simmons, and P. E. Sokol, 1988, Phys. Rev. B **38**, 11275.
Langreth, D. C., and J. P. Perdew, 1975, Solid State Commun. **17**, 1425.
Lawless, W. N., 1974, Ferroelectrics **7**, 379.
Lazicki, A., Y. Fei, and R. Hemley, 2010, Solid State Commun. **150**, 625.
Lee, K., E. D. Murray, L. Kong, B. I. Lundqvist, and D. C. Langreth, 2010, Phys. Rev. B **82**, 081101.
Lewestein, M., A. Sanpera, V. Ahufinger, B. Damski, A. Sen, and U. Sen, 2007, Adv. Phys. **56**, 243.
Li, X.-P., D. M. Ceperley, and R. M. Martin, 1991, Phys. Rev. B **44**, 10929.
Li, X.-Z., B. Walker, and A. Michaelides, 2011, Proc. Natl. Acad. Sci. U.S.A. **108**, 6369.
Li, X.-Z., B. Walker, M. I. J. Probert, C. J. Pickard, R. J. Needs, and A. Michaelides, 2013, J. Phys. Condens. Matter **25**, 085402.
Li, Z., J. R. Kermode, and A. D. Vita, 2015, Phys. Rev. Lett. **114**, 096405.
Lin, L., J. A. Morrone, R. Car, and M. Parrinello, 2010, Phys. Rev. Lett. **105**, 110602.
Lin, L., J. A. Morrone, R. Car, and M. Parrinello, 2011, Phys. Rev. B **83**, 220302(R).
Lin, Y.-S., G.-D. Li, S.-P. Mao, and J.-D. Chai, 2013, J. Chem. Theory Comput. **9**, 263.
Lipschultz, F. P., V. J. Minkiewicz, T. A. Kitchens, G. Shirane, and R. Nathans, 1967, Phys. Rev. Lett. **19**, 1307.
Lisunov, A., V. Maidanov, V. Rubanskyi, S. Rubets, E. Rudavskii, S. Smirnov, and V. Zhuchkov, 2015, Phys. Rev. B **92**, 140505(R).
Liu, H., H. Wang, and Y. Ma, 2012, J. Phys. Chem. C **116**, 9221.
Liu, H., L. Zhu, W. Cui, and Y. Ma, 2012, J. Chem. Phys. **137**, 074501.
Lloyd-Williams, J. H., R. J. Needs, and G. J. Conduit, 2015, Phys. Rev. B **92**, 075106.

López-Ríos, P., A. Ma, N. D. Drummond, M. D. Towler, and R. J. Needs, 2006, Phys. Rev. E **74**, 066701.
Lorenz, S., A. Groß, and M. Scheffler, 2004, Chem. Phys. Lett. **395**, 210.
Lorenzana, H. E., I. F. Silvera, and K. A. Goettel, 1989, Phys. Rev. Lett. **63**, 2080.
Lorenzana, H. E., I. F. Silvera, and K. A. Goettel, 1990, Phys. Rev. Lett. **64**, 1939.
Loubeyre, P., 1987, Phys. Rev. Lett. **58**, 1857.
Loubeyre, P., R. LeToullec, J. P. Pinceaux, H. K. Mao, J. Hu, and R. J. Hemley, 1993, Phys. Rev. Lett. **71**, 2272.
Loubeyre, P., F. Occelli, and P. Dumas, 2013, Phys. Rev. B **87**, 134101.
Loubeyre, P., F. Occelli, and R. LeToullec, 2002, Nature (London) **416**, 613.
Lovell, A., F. Fernandez-Alonso, N. T. Skipper, K. Refson, S. M. Bennington, and S. F. Parker, 2008, Phys. Rev. Lett. **101**, 126101.
Ludueña, G. A., and D. Sebastiani, 2010, J. Phys. Chem. Lett. **1**, 3214.
Lutsyshyn, Y., 2015, Comput. Phys. Commun. **187**, 162.
Lutsyshyn, Y., C. Cazorla, G. E. Astrakharchik, and J. Boronat, 2010, Phys. Rev. B **82**, 180506(R).
Lutsyshyn, Y., C. Cazorla, and Boronat, 2010, J. Low Temp. Phys. **158**, 608.
Lutsyshyn, Y., R. Rota, and Boronat, 2011, J. Low Temp. Phys. **162**, 455.
Ma, F., S. Zhang, and H. Krakauer, 2011, Phys. Rev. B **84**, 155130.
Ma, Y., A. R. Oganov, Z. Li, Y. Xie, and J. Kotakoski, 2009, Phys. Rev. Lett. **102**, 065501.
MacFarland, T., S. A. Vitiello, L. Reatto, G. V. Chester, and M. H. Kalos, 1994, Phys. Rev. B **50**, 13577.
Mailhiot, C., L. H. Yang, and A. K. McMahan, 1992, Phys. Rev. B **46**, 14419.
Manzhos, S., K. Yamashita, and T. Carrington, Jr., 2009, Chem. Phys. Lett. **474**, 217.
Mao, H.-K., and R. J. Hemley, 1994, Rev. Mod. Phys. **66**, 671.
Mardirossian, N., and M. Head-Gordon, 2014, Phys. Chem. Chem. Phys. **16**, 9904.
Maris, H. J., 2009, J. Low Temp. Phys. **155**, 290.
Maris, H. J., 2010, J. Low Temp. Phys. **158**, 485.
Maris, H. J., 2012, Phys. Rev. B **86**, 020502(R).
Maris, H. J., and D. O. Edwards, 2002, J. Low Temp. Phys. **129**, 1.
Maris, J. H., 1995, J. Low Temp. Phys. **98**, 403.
Martyna, G. J., A. Hughes, and M. E. Tuckerman, 1999, J. Chem. Phys. **110**, 3275.
Marx, D., and M. H. Müser, 1999, J. Phys. Condens. Matter **11**, R117.
Marx, D., O. Opitz, P. Nielaba, and K. Binder, 1993, Phys. Rev. Lett. **70**, 2908.
Marx, D., S. Sengupta, and P. Nielaba, 1993, J. Chem. Phys. **99**, 6031.
Marx, D., M. E. Tuckerman, and G. J. Martyna, 1999, Comput. Phys. Commun. **118**, 166.
Masia, M., E. Guàrdia, and P. Nicolini, 2014, Int. J. Quantum Chem. **114**, 1036.
Matveeva, M., and S. Giorgini, 2012, Phys. Rev. Lett. **109**, 200401.
Maynard-Casely, H. E., C. L. Bull, M. Guthrie, I. Loa, M. I. McMahon, E. Gregoryanz, R. J. Nelmes, and J. S. Loveday, 2010, J. Chem. Phys. **133**, 064504.
McBride, C., E. G. Noya, J. L. Aragones, M. M. Conde, and C. Vega, 2012, Phys. Chem. Chem. Phys. **14**, 10140.
McMahon, J. M., and D. Ceperley, 2011, Phys. Rev. Lett. **106**, 165302.
McMahon, J. M., M. A. Morales, C. Pierleoni, and D. M. Ceperley, 2012, Rev. Mod. Phys. **84**, 1607.
McMahon, M. I., R. J. Nelmes, W. F. Kuhst, R. Dorwarth, R. O. Piltz, and Z. Tun, 1990, Nature (London) **348**, 317.
McMillan, W. L., 1965, Phys. Rev. **138**, A442.
Metropolis, N., A. W. Rosenbluth, M. N. Rosenbluth, A. M. Teller, and E. Teller, 1953, J. Chem. Phys. **21**, 1087.
Mezzacapo, F., and M. Boninsegni, 2008, Phys. Rev. Lett. **100**, 145301.
Militzer, B., and R. L. Graham, 2006, J. Phys. Chem. Solids **67**, 2136.
Miller, W. H., 2005, Proc. Natl. Acad. Sci. U.S.A. **102**, 6660.
Minkiewicz, V. J., T. A. Kitchens, F. P. Lipschultz, R. Nathans, and G. Shirane, 1968, Phys. Rev. **174**, 267.
Misquitta, A. J., J. Spencer, A. J. Stone, and A. Alavi, 2010, Phys. Rev. B **82**, 075312.
Mitas, L., E. L. Shirley, and D. M. Ceperley, 1991, J. Chem. Phys. **95**, 3467.
Mochalin, V. N., O. Shenderova, D. Ho, and Y. Gogotsi, 2012, Nat. Nanotechnol. **7**, 11.
Monserrat, B., N. D. Drummond, and R. J. Needs, 2013, Phys. Rev. B **87**, 144302.
Monserrat, B., N. D. Drummond, C. J. Pickard, and R. J. Needs, 2014, Phys. Rev. Lett. **112**, 055504.
Monserrat, B., and R. J. Needs, 2014, Phys. Rev. B **89**, 214304.
Monserrat, B., R. J. Needs, E. Gregoryanz, and C. J. Pickard, 2016, Phys. Rev. B **94**, 134101.
Moraldi, M., 2009, Phys. Rev. B **80**, 134117.
Moraldi, M., 2012, J. Low Temp. Phys. **168**, 275.
Morales, M. A., J. R. Gergely, J. McMinis, J. M. McMahon, J. Kim, and D. M. Ceperley, 2014, J. Chem. Theory Comput. **10**, 2355.
Morales, M. A., J. M. McMahon, C. Pierleoni, and D. M. Ceperley, 2013, Phys. Rev. B **87**, 184107.
Morales, M. A., C. Pierleoni, and D. M. Ceperley, 2010, Phys. Rev. E **81**, 021202.
Moreira, P. A. F. P., and M. de Koning, 2015, Phys. Chem. Chem. Phys. **17**, 24716.
Moroni, S., and M. Boninsegni, 2014, Phys. Rev. Lett. **113**, 240407.
Moroni, S., F. Pederiva, S. Fantoni, and M. Boninsegni, 2000, Phys. Rev. Lett. **84**, 2650.
Morrone, J. A., and R. Car, 2008, Phys. Rev. Lett. **101**, 017801.
Müller, K. A., and H. Burkard, 1979, Phys. Rev. B **19**, 3593.
Müser, M. H., and B. J. Berne, 1996, Phys. Rev. Lett. **77**, 2638.
Nabi, Z., L. Vitos, B. Johansson, and R. Ahuja, 2005, Phys. Rev. B **72**, 172102.
Natoli, V., R. Martin, and D. M. Ceperley, 1995, Phys. Rev. Lett. **74**, 1601.
Needs, R. J., M. Towler, N. Drummond, and P. L. Ríos, 2010, J. Phys. Condens. Matter **22**, 023201.
Nemoto, K., M. Trupke, S. J. Devitt, A. M. Stephens, B. Scharfenberger, K. Buczak, T. Nobauer, M. S. Everitt, J. Schmiedmayer, and W. J. Munro, 2014, Phys. Rev. X **4**, 031022.
Neumann, M., and M. Zoppi, 2002, Phys. Rev. E **65**, 031203.
Nguyen, H.-V., and S. de Gironcoli, 2009, Phys. Rev. B **79**, 205114.
Nielsen, M., 1973, Phys. Rev. B **7**, 1626.
Nielsen, M., and H. B. M. ller, 1971, Phys. Rev. B **3**, 4383.
Norman, M. J., R. O. Watts, and U. Buck, 1984, J. Chem. Phys. **81**, 3500.
Nosanow, L. H., 1966, Phys. Rev. **146**, 120.
Nosanow, L. H., and G. L. Shaw, 1962, Phys. Rev. **128**, 546.
Ohtomo, A., and H. Y. Hwang, 2004, Nature (London) **427**, 423.
Omiyinka, T., and M. Boninsegni, 2013, Phys. Rev. B **88**, 024112.
Omiyinka, T., and M. Boninsegni, 2016, Phys. Rev. B **93**, 104501.

Operetto, F., and F. Pederiva, 2006, Phys. Rev. B **73**, 184124.
Ortiz, G., D. M. Ceperley, and R. M. Martin, 1993, Phys. Rev. Lett. **71**, 2777.
Osychenko, O. N., R. Rota, and J. Boronat, 2012, Phys. Rev. B **85**, 224513.
Pamuk, B., J. M. Soler, R. Ramírez, C. P. Herrero, P. Stephens, P. B. Allen, and M.-V. Fernández-Serra, 2012, Phys. Rev. Lett. **108**, 193003.
Paris, A., *et al.*, 2013, Adv. Funct. Mater. **23**, 1628.
Patrick, C. E., and F. Giustino, 2013, Nat. Commun. **4**, 2006.
Paulatto, L., Errea, I., M. Calandra, and F. Mauri, 2015, Phys. Rev. B **91**, 054304.
Pechenik, E., I. Kelson, and G. Makov, 2008, Phys. Rev. B **78**, 134109.
Peek, D. A., M. C. Schmidt, I. Fujita, and R. O. Simmons, 1992, Phys. Rev. B **45**, 9680.
Peña-Ardila, L. A., S. A. Vitiello, and M. de Koning, 2011, Phys. Rev. B **84**, 094119.
Per, M. C., S. P. Russo, and I. K. Snook, 2008, J. Chem. Phys. **128**, 114106.
Perdew, J. P., 2013, MRS Bull. **38**, 743.
Perdew, J. P., K. Burke, and M. Ernzerhof, 1996, Phys. Rev. Lett. **77**, 3865.
Perdew, J. P., J. A. Chevary, S. H. Vosko, K. A. Jackson, M. R. Pederson, D. J. Singh, and C. Fiolhais, 1992, Phys. Rev. B **46**, 6671.
Perdew, J. P., and A. Zunger, 1981, Phys. Rev. B **23**, 5048.
Pessoa, R., M. de Koning, and S. A. Vitiello, 2009a, J. Stat. Phys. **134**, 769.
Pessoa, R., M. de Koning, and S. A. Vitiello, 2009b, Phys. Rev. B **80**, 172302.
Pessoa, R., M. de Koning, and S. A. Vitiello, 2013, J. Low Temp. Phys. **173**, 143.
Pessoa, R., S. A. Vitiello, and M. de Koning, 2010, Phys. Rev. Lett. **104**, 085301.
Pickard, C. J., M. Martinez-Canales, and R. J. Needs, 2012, Phys. Rev. B **85**, 214114; **86**, 059902(E) (2012).
Pickard, C. J., and R. J. Needs, 2006, Phys. Rev. Lett. **97**, 045504.
Pickard, C. J., and R. J. Needs, 2007, Nat. Phys. **3**, 473.
Pickard, C. J., and R. J. Needs, 2009, Phys. Status Solidi B **246**, 536.
Pierce, M. E., and E. Manousakis, 2000, Phys. Rev. B **62**, 5228.
Pierleoni, C., and D. M. Ceperley, 2005, ChemPhysChem **6**, 1872.
Pierleoni, C., and D. M. Ceperley, 2006, *Computer Simulations in Condensed Matter Systems: From Materials to Chemical Biology* (Springer, Berlin/Heidelberg), Vol. 703, p. 641.
Pierleoni, C., D. M. Ceperley, and M. Holzmann, 2004, Phys. Rev. Lett. **93**, 146402.
Pollet, L., M. Boninsegni, A. B. Kuklov, N. V. Prokof'ev, B. V. Svistunov, and M. Troyer, 2007, Phys. Rev. Lett. **98**, 135301.
Pollet, L., M. Boninsegni, A. B. Kuklov, N. V. Prokof'ev, B. V. Svistunov, and M. Troyer, 2008, Phys. Rev. Lett. **101**, 097202.
Presber, M., D. Löding, R. Martoňák, and P. Nielaba, 1998, Phys. Rev. B **58**, 11937.
Press, W., 1972, J. Chem. Phys. **56**, 2597.
Press, W., and A. Kollmar, 1975, Solid State Commun. **17**, 405.
Protopapa, S., H. Boehnhardt, T. M. Herbst, D. P. Cruikshank, W. M. Grundy, F. Merlin, and C. B. Olkin, 2008, Astron. Astrophys. **490**, 365.
Proville, L., D. Rodney, and M.-C. Marinica, 2012, Nat. Mater. **11**, 845.
Purwanto, W., H. Krakauer, Y. Virgus, and S. Zhang, 2011, J. Chem. Phys. **135**, 164105.
Qi, T., and E. J. Reed, 2012, J. Phys. Chem. A **116**, 10451.
Raghunathan, R., P. O. Dral, M. Rupp, and O. A. von Lilienfeld, 2015, J. Chem. Theory Comput. **11**, 2087.
Ramírez, R., and C. P. Herrero, 2008, J. Chem. Phys. **129**, 204502.
Ramírez, R., and C. P. Herrero, 2010, J. Chem. Phys. **133**, 144511.
Ramírez, R., C. P. Herrero, A. Antonelli, and E. R. Hernández, 2008, J. Chem. Phys. **129**, 064110.
Ramírez, R., N. Neuerburg, M.-V. Fernández-Serra, and C. P. Herrero, 2012, J. Chem. Phys. **137**, 044502.
Ray, M. W., and R. B. Hallock, 2008, Phys. Rev. Lett. **100**, 235301.
Ray, M. W., and R. B. Hallock, 2010, Phys. Rev. Lett. **105**, 145301.
Reiter, G. F., J. C. Li, J. Mayers, T. Abdul-Redah, and P. Platzman, 2004, Braz. J. Phys. **34**, 142.
Reiter, G. F., J. Mayers, and P. Platzman, 2002, Phys. Rev. Lett. **89**, 135505.
Reiter, G. F., A. Shukla, P. Platzman, and J. Mayers, 2008, New J. Phys. **10**, 013016.
Reppy, J. D., 2010, Phys. Rev. Lett. **104**, 255301.
Reynolds, P. J., D. M. Ceperley, B. J. Alder, and W. A. Lester, Jr., 1982, J. Chem. Phys. **77**, 5593.
Roger, M., J. H. Hetherington, and J. M. Delrieu, 1983, Rev. Mod. Phys. **55**, 1.
Rossi, M., and F. Ancilotto, 2016, Phys. Rev. B **94**, 100502(R).
Rossi, M., D. E. Galli, and L. Reatto, 2005, Phys. Rev. B **72**, 064516.
Rossi, M., M. Nava, L. Reatto, and D. E. Galli, 2009, J. Chem. Phys. **131**, 154108.
Rossi, M., L. Reatto, and D. E. Galli, 2012, J. Low Temp. Phys. **168**, 235.
Rossi, M., E. Vitali, D. E. Galli, and L. Reatto, 2008, J. Low Temp. Phys. **153**, 250.
Rossi, M., E. Vitali, D. E. Galli, and L. Reatto, 2010, J. Phys. Condens. Matter **22**, 145401.
Rossi, M., E. Vitali, L. Reatto, and D. E. Galli, 2012, Phys. Rev. B **85**, 014525.
Rota, R., and J. Boronat, 2011, J. Low Temp. Phys. **162**, 146.
Rota, R., and J. Boronat, 2012, Phys. Rev. Lett. **108**, 045308.
Rota, R., J. Casulleras, F. Mazzanti, and J. Boronat, 2010, Phys. Rev. E **81**, 016707.
Rota, R., Y. Lutsyshyn, C. Cazorla, and J. Boronat, 2012, J. Low Temp. Phys. **168**, 150.
Röttger, K., A. Endriss, J. Ihringer, S. Doyle, and W. F. Kuhs, 1994, Acta Crystallogr. Sect. B **50**, 644.
Rousseau, R., and D. Marx, 1998, Phys. Rev. Lett. **80**, 2574.
Rowley, S. E., L. J. Spalek, R. P. Smith, M. P. M. Dean, M. Itoh, J. F. Scott, G. G. Lonzarich, and S. S. Saxena, 2014, Nat. Phys. **10**, 367.
Ruiz, V. G., W. Liu, E. Zojer, M. Scheffler, and A. Tkatchenko, 2012, Phys. Rev. Lett. **108**, 146103.
Rupp, M., 2015, Int. J. Quantum Chem. **115**, 1058.
Rytz, D., U. T. Hochli, and H. Bilz, 1980, Phys. Rev. B **22**, 359.
Safar, H., P. L. Gammel, D. A. Huse, D. J. Bishop, J. P. Rice, and D. M. Ginsberg, 1992, Phys. Rev. Lett. **69**, 824.
Sakkos, K., J. Casulleras, and J. Boronat, 2009, J. Chem. Phys. **130**, 204109.
Samara, G. A., 1988, Physica B+C (Amsterdam) **150**, 179.
Santra, B., J. Klimeš, D. Alfè, A. Tkatchenko, B. Slater, A. Michaelides, R. Car, and M. Scheffler, 2011, Phys. Rev. Lett. **107**, 185701.
Sarsa, A., K. E. Schmidt, and W. R. Magro, 2000, J. Chem. Phys. **113**, 1366.
Sasaki, S., R. Ishiguro, F. Caupin, H. J. Maris, and S. Balibar, 2006, Science **313**, 1098.
Schaeffer, A. M. J., W. B. Talmadge, S. R. Temple, and S. Deemyad, 2012, Phys. Rev. Lett. **109**, 185702.
Schiff, D., and L. Verlet, 1967, Phys. Rev. **160**, 208.

Schlom, D. G., L.-Q. Chen, C.-B. Eom, K. M. Rabe, S. K. Streiffer, and J.-M. Triscone, 2007, Annu. Rev. Mater. Res. **37**, 589.
Schmidt, K. E., and M. H. Kalos, 1984, *Few- and Many-Body Problems, Monte Carlo Methods in Statistical Physics* (Springer-Verlag, Berlin).
Schnepp, O., 1970, Phys. Rev. A **2**, 2574.
Schöffel, P., and M. H. Müser, 2001, Phys. Rev. B **63**, 224108.
Scott, T. A., 1976, Phys. Rep. **27**, 89.
Senesi, R., D. Flammini, A. I. Kolesnikov, E. D. Murray, G. Galli, and C. Andreani, 2013, J. Chem. Phys. **139**, 074504.
Sevryuk, M. B., J. P. Toennies, and D. M. Ceperley, 2010, J. Chem. Phys. **133**, 064505.
Sham, L. J., and W. Kohn, 1966, Phys. Rev. **145**, 561.
Shevlin, S. A., C. Cazorla, and Z. X. Guo, 2012, J. Phys. Chem. C **116**, 13488.
Shevlin, S. A., and Z. X. Guo, 2009, Chem. Soc. Rev. **38**, 211.
Shin, J., J. Choi, K. Shirahama, and E. Kim, 2016, Phys. Rev. B **93**, 214512.
Shukla, K., A. Paskin, D. O. Welch, and G. J. Dienes, 1981, Phys. Rev. B **24**, 724.
Shumway, J., 2005, J. Phys. Condens. Matter **17**, 2563.
Shvartsman, V. V., P. Borisov, W. Kleemann, S. Kamba, and T. Katsufuji, 2010, Phys. Rev. B **81**, 064426.
Silvera, I. F., 1980, Rev. Mod. Phys. **52**, 393.
Silvera, I. F., and V. V. Goldman, 1978, J. Chem. Phys. **69**, 4209.
Sindzingre, P., D. M. Ceperley, and M. L. Klein, 1991, Phys. Rev. Lett. **67**, 1871.
Sindzingre, P., M. L. Klein, and D. M. Ceperley, 1989, Phys. Rev. Lett. **63**, 1601.
Singer, S. J., J.-L. Kuo, T. K. Hirsch, C. Knight, L. Ojamae, and M. L. Klein, 2005, Phys. Rev. Lett. **94**, 135701.
Sola, E., and J. Boronat, 2011, J. Phys. Chem. A **115**, 7071.
Sola, E., J. Casulleras, and J. Boronat, 2006, Phys. Rev. B **73**, 092515.
Souris, F., A. D. Fefferman, A. Haziot, N. Garroum, J. R. Beamish, and S. Balibar, 2015, J. Low Temp. Phys. **178**, 149.
Souris, F., A. D. Fefferman, H. J. Maris, V. Dauvois, P. Jean-Baptiste, J. R. Beamish, and S. Balibar, 2014, Phys. Rev. B **90**, 180103(R).
Söyler, S. G., A. B. Kuklov, L. Pollet, N. V. Prokof'ev, and B. V. Svistunov, 2009, Phys. Rev. Lett. **103**, 175301.
Srinivasan, V., and D. Sebastiani, 2011, J. Phys. Chem. C **115**, 12631.
Städele, M., and R. M. Martin, 2000, Phys. Rev. Lett. **84**, 6070.
Stassis, C., G. Kline, W. Kamitakahara, and S. K. Sinha, 1978, Phys. Rev. B **17**, 1130.
Surh, M. P., K. J. Runge, T. Barbee, E. L. Pollock, and C. Mailhiot, 1997, Phys. Rev. B **55**, 11330.
Syshchenko, O., J. Day, and J. Beamish, 2009, J. Phys. Condens. Matter **21**, 164204.
Tanaka, H., H. Kanoh, M. Yudasaka, S. Iijima, and K. Kaneko, 2005, J. Am. Chem. Soc. **127**, 7511.
Tanatar, B., and D. M. Ceperley, 1989, Phys. Rev. B **39**, 5005.
Tavernarakis, A., J. Chaste, A. Eichler, G. Ceballos, M. C. Gordillo, J. Boronat, and A. Bachtold, 2014, Phys. Rev. Lett. **112**, 196103.
Tejeda, G., J. M. Fernández, S. Montero, D. Blume, and J. P. Toennies, 2004, Phys. Rev. Lett. **92**, 223401.
Teweldeberhan, A. M., J. L. Dubois, and S. A. Bonev, 2010, Phys. Rev. Lett. **105**, 235503.
Timms, D. N., A. C. Evans, M. Boninsegni, D. M. Ceperley, J. Mayers, and R. O. Simmons, 1996, J. Phys. Condens. Matter **8**, 6665.
Timms, D. N., R. O. Simmons, and J. Mayers, 2003, Phys. Rev. B **67**, 172301.
Tkatchenko, A., D. Alfè, and K. S. Kim, 2012, J. Chem. Theory Comput. **8**, 4317.
Tkatchenko, A., R. A. DiStasio, Jr., R. Car, and M. Scheffler, 2012, Phys. Rev. Lett. **108**, 236402.
Tkatchenko, A., and M. Scheffler, 2009, Phys. Rev. Lett. **102**, 073005.
Tomasino, D., Z. Jenei, W. Evans, and C.-S. Yoo, 2014, J. Chem. Phys. **140**, 244510.
Towler, M. D., 2006, Phys. Status Solidi B **243**, 2573.
Trail, J. R., and R. J. Needs, 2013, J. Chem. Phys. **139**, 014101.
Trail, J. R., and R. J. Needs, 2015, J. Chem. Phys. **142**, 064110.
Trotter, H. F., 1959, Proc. Am. Math. Soc. **10**, 545.
Troullier, N., and J. L. Martins, 1991, Phys. Rev. B **43**, 1993.
Tubman, N. M., J. L. DuBois, R. Q. Hood, and B. J. Alder, 2011, J. Chem. Phys. **135**, 184109.
Tubman, N. M., I. Kylänpää, S. Hammes-Schiffer, and D. M. Ceperley, 2014, Phys. Rev. A **90**, 042507.
Tuckerman, M. E., and A. Hughes, 1998, *Classical and Quantum Dynamics in Condensed Phase Simulations* (World Scientific, Singapore).
Ubbelohde, A. R., and K. J. Gallagher, 1955, Acta Crystallogr. **8**, 71.
Umrigar, C. J., J. Toulouse, C. Filippi, S. Sorella, and R. G. Hennig, 2007, Phys. Rev. Lett. **98**, 110201.
Umrigar, C. J., K. G. Wilson, and J. W. Wilkins, 1988, Phys. Rev. Lett. **60**, 1719.
Vanderbilt, D., 1990, Phys. Rev. B **41**, 7892(R).
Vega, C., M. M. Conde, C. McBride, J. L. F. Abascal, E. G. Noya, R. Ramírez, and L. M. Sesé, 2010, J. Chem. Phys. **132**, 046101.
Vekhov, Y., and R. B. Hallock, 2012, Phys. Rev. Lett. **109**, 045303.
Veleckis, E., 1977, J. Phys. Chem. **81**, 526.
Vidal, J. P., and G. Vidal-Valat, 1986, Acta Crystallogr. Sect. B **42**, 131.
Vilches, O. E., 1992, J. Low Temp. Phys. **89**, 267.
Vitiello, S. A., 2011, J. Low Temp. Phys. **162**, 154.
Vitiello, S. A., K. Runge, and M. H. Kalos, 1988, Phys. Rev. Lett. **60**, 1970.
Vranješ, L., J. Boronat, J. Casulleras, and C. Cazorla, 2005, Phys. Rev. Lett. **95**, 145302.
Vranješ Markić, L., and H. R. Glyde, 2015, Phys. Rev. B **92**, 064510.
Vydrov, O. A., and T. V. Voorhis, 2012, J. Chem. Theory Comput. **8**, 1929.
Wagner, L. K., 2014, Int. J. Quantum Chem. **114**, 94.
Wagner, L. K., 2015, Phys. Rev. B **92**, 161116.
Wagner, L. K., M. Bajdich, and L. Mitas, 2009, J. Comput. Phys. **228**, 3390.
Wagner, L. K., and J. C. Grossman, 2010, Phys. Rev. Lett. **104**, 210201.
Wagner, M., and D. M. Ceperley, 1994, J. Low Temp. Phys. **94**, 161.
Wagner, M., and D. M. Ceperley, 1996, J. Low Temp. Phys. **102**, 275.
Wallace, D. C., 1972, *Thermodynamics of Crystals* (Wiley, New York).
Wang, J.-S., 2007, Phys. Rev. Lett. **99**, 160601.
Wang, X., Y. Wang, M. Miao, X. Zhong, J. Lv, T. Cui, J. Li, L. Chen, C. J. Pickard, and Y. Ma, 2012, Phys. Rev. Lett. **109**, 175502.
Wang, Y., *et al.*, 2015, ACS Nano **9**, 7769.
Wang, Z., J. Wei, P. Morse, J. G. Dash, O. E. Vilches, and D. H. Cobden, 2010, Science **327**, 552.
Wanner, R., and H. Meyer, 1973, J. Low Temp. Phys. **11**, 715.
Welch, F. H., 1974, Nucl. Eng. Des. **26**, 444.
Wette, F. W., and B. R. A. Nijboer, 1965, Phys. Lett. **18**, 19.
Whitlock, P. A., D. M. Ceperley, G. V. Chester, and M. H. Kalos, 1979, Phys. Rev. B **19**, 5598.

Whitlock, P. A., G. V. Chester, and M. H. Kalos, 1988, Phys. Rev. B **38**, 2418.
Whitlock, P. A., and M. H. Kalos, 1979, J. Comput. Phys. **30**, 361.
Wigner, E., 1934, Phys. Rev. **46**, 1002.
Wigner, E., and H. B. Huntington, 1935, J. Chem. Phys. **3**, 764.
Wikfeldt, K. T., 2014, J. Phys. Conf. Ser. **571**, 012012.
Wikfeldt, K. T., and A. Michaelides, 2014, J. Chem. Phys. **140**, 041103.
Withers, B., and H. R. Glyde, 2007, J. Low Temp. Phys. **147**, 633.
Wood, W. W., and F. R. Parker, 1957, J. Chem. Phys. **27**, 720.
Yang, Y., I. Kylänpää, N. M. Tubman, J. T. Krogel, S. Hammes-Schiffer, and D. M. Ceperley, 2015, J. Chem. Phys. **143**, 124308.
Zha, C.-S., T. S. Duffy, H.-K. Mao, and R. J. Hemley, 1993, Phys. Rev. B **48**, 9246.
Zha, C.-S., Z. Liu, and R. J. Hemley, 2012, Phys. Rev. Lett. **108**, 146402.
Zha, C.-S., H.-K. Mao, and R. J. Hemley, 2004, Phys. Rev. B **70**, 174107.
Zhang, C., M. Dyer, and A. Alavi, 2005, J. Phys. Chem. B **109**, 22089.
Zhang, L. J., Y. L. Niu, T. Cui, Y. Li, Y. M. Ma, Z. He, and G. T. Zou, 2007, J. Phys. Condens. Matter **19**, 425237.
Zhao, Y., N. E. Schultz, and D. G. Truhlar, 2005, J. Chem. Phys. **123**, 161103.
Zhou, C., C. Reichhardt, M. J. Graf, and J.-J. Su, 2013, Phys. Rev. Lett. **111**, 119601.
Zhu, Q., A. R. Oganov, C. W. Glass, and H. T. Stokes, 2012, Acta Crystallogr. Sect. B **68**, 215.